



University
of Glasgow

Lin, Hequan (1997) *Prediction of separated flows around pitching aerofoils using a discrete vortex method.*

PhD thesis

<http://theses.gla.ac.uk/3950/>

Copyright and moral rights for this thesis are retained by the author

A copy can be downloaded for personal non-commercial research or study, without prior permission or charge

This thesis cannot be reproduced or quoted extensively from without first obtaining permission in writing from the Author

The content must not be changed in any way or sold commercially in any format or medium without the formal permission of the Author

When referring to this work, full bibliographic details including the author, title, awarding institution and date of the thesis must be given

Prediction of Separated Flows Around Pitching Aerofoils
Using a Discrete Vortex Method

by

Hequan Lin
BSc.(Eng), MSc.(Eng)

A dissertation submitted to
the Faculty of Engineering
in partial fulfillment
of the requirements for the degree of
Doctor of Philosophy

University of Glasgow

©Hequan Lin, 1997

University of Glasgow

Abstract

Prediction of Separated Flows Around Pitching Aerofoils
Using a Discrete Vortex Method

by Hequan Lin

A surface shedding discrete vortex method has been developed for simulating incompressible flows around pitching aerofoils. The method is able to predict both attached and separated flows, the latter typified by the formation and transport of large vortices. The structures of dynamic stall flow are well captured without the need for other means to predetermine the separation points. In contrast to most other vortex methods, the method presented herein can perform quantitative analysis. Throughout a wide range of incidence, the pressure distributions are smooth, and the normal force and pitching moment are in good agreement with experimental data. The method is also able to predict the flow with external constraints for simulating the effects of wind tunnel blockage. In this regard quantitative results and flow structures have been obtained which are consistent with those expected.

Following the review of previous work presented in the introduction, the mathematical formulation of the method is expounded. A velocity expression is theoretically derived for flows with both a moving inner boundary (aerofoil) and fixed external constraints (wind tunnel walls). To maintain both no penetration and no slip conditions, it is concluded that an external constraint parallel to the free stream can be modelled by placement of a constant vortex sheet along the boundary, and the introduction of distributed vortices next to the constraint to represent the boundary layer. The vortex sheet strength is equivalent to the free stream velocity while the strength of the vortices can be calculated in the same manner as for the internal boundary. This conclusion avoids the necessity of employing mirror vortices and iteration techniques

in traditional models.

The aerodynamic loads are computed from the pressure distribution. For the computation of surface pressures, the relationship between the pressure gradient and the rate of vorticity creation on the surface has been developed for a moving boundary.

Numerically, a surface vortex shedding model has been proposed and implemented which contrasts with the traditional vortex shedding from sharp edges or predetermined points. The method is based on the concept of two-zone vorticity discretization. The two zones are comprised of a creation zone, for the thin strip close to the boundary, and a wake zone for the remaining flow region. As with most vortex methods, a Lagrangian description of the wake vortices is employed, in conjunction with a random walk model for viscous diffusion. In the creation zone, vorticity is re-discretized every time step at specified points, with the strength determined from the implementation of boundary conditions. These nascent vortices are considered as a discretized representation of a vortex sheet, with circulation strength distributed in a piecewise linear and continuous fashion. The surface vortex shedding model simulates the exchange of vorticity across the zone boundary. The convection and diffusion of vorticity are reflected in the model via operator splitting; that is, at each time step, vortices are first convected using the Biot-Savart law, and subsequently given a random displacement consistent with the viscous model employed.

A sub-panel model has been used in the representation of the body surface. Each sub-panel is defined in conjunction with the multi-vortex discretization on every panel. De-coupling of the continuous vorticity distribution has been proposed at a sharp edge like an aerofoil trailing edge to improve the predicted flow behaviour in such regions. These novel techniques, combined with the traditional vortex blob method, random vortex method, vortex amalgamation and Adams-Bashfort second order method for vortex convection, have led to a successful simulation of separated pitching aerofoil flows. It is expected that the method can be further developed for simulating bluff body flows and three dimensional flows.

TABLE OF CONTENTS

List of Figures	iii
Nomenclature	vi
Chapter 1: Introduction	1
1.1 Theoretical background and classical methods	2
1.2 Dynamic stall phenomena	5
1.3 Numerical approach – grid based methods	10
1.4 Numerical approach – vortex methods	17
1.5 Summary of present method	25
Chapter 2: Mathematical formulation	27
2.1 Governing equations	27
2.2 Influence of moving body	29
2.3 Influence of external boundary	31
2.4 Velocity field in terms of the vorticity	33
2.5 Conservation of circulation	39
2.6 Boundary conditions	40
2.7 Evaluation of the force and moment	44
2.8 Conclusion	46
Chapter 3: Numerical implementation	48
3.1 Vorticity layer	48
3.2 Discretization – description of vorticity	51
3.3 Determination of flow	60
3.4 Shedding of Vorticity	64
3.5 Creation of vorticity	69

3.6	Pressure distribution	70
3.7	Amalgamation of vortices	71
3.8	Boundary condition enhancement	73
3.9	Sharp edge modelling	76
3.10	External constraints	81
3.11	Computational procedure	82
Chapter 4:	Flow prediction and analysis	86
4.1	Impulsively started flows	87
4.2	Flows around pitching aerofoils	88
4.3	Constrained flows around aerofoils	92
4.4	Ramp-up and Ramp-down motion	94
Chapter 5:	Concluding remarks	118
5.1	Summary	118
5.2	Further developments	121
	References	123
	Appendix A:	141

LIST OF FIGURES

1.1	Illustration of dynamic stall events from ref. ⁸	7
1.2	Lift histories for pitch-up from ref. ⁵⁶	12
1.3	Lift coefficients from ref. ⁴⁹	12
1.4	Normal force coefficients from ref. ³⁷	13
1.5	Lift and moment coefficients from ref. ⁵¹	14
1.6	Steady-state lift coefficients from ref. ¹¹²	15
1.7	Aerodynamic coefficients from ref. ⁴²	16
1.8	Pressure and lift coefficient from ref. ¹⁵⁹	24
2.1	Reference coordinate system	29
2.2	Flow regions	32
3.1	Illustration of velocity distribution near surface	50
3.2	Illustration of vorticity layer of attached flows	50
3.3	Illustration of vorticity layer of separated flows	51
3.4	Vorticity and velocity distributions for various cores	53
3.5	Illustration of creation zone and wake zone	56
3.6	Discrete points in creation zone	56
3.7	Discretization of surface	57
3.8	Multi-panel discretization of vorticity upon a curved segment	57
3.9	Discretization of vorticity upon a straight segment	58
3.10	First time step γ distribution for the NACA0012 at 0°	63
3.11	Assumed velocity and vorticity profiles in creation zone	67
3.12	Normal velocity on panel for different numbers of panel vortices	74
3.13	Normal velocity comparison along vortex creation line for different numbers of panel vortices	75

3.14	Additional control strip	76
3.15	First time step γ distribution for model with equal trailing edge γ for upper and lower surface	78
3.16	First time step γ distribution for model with constant γ on lower surface trailing panel	79
3.17	First time step γ distribution for model which interpolates γ on lower surface	80
3.18	Illustration of trailing edge region	81
3.19	Illustration of constraints	82
3.20	Flow diagram of computational procedure	85
4.1	Correlation of normal force coefficients with experimental data	96
4.2	Pressure distributions for the NACA0012	96
4.3	Circulation history, $Re = 990,000$	96
4.4	Vortex patterns and streamlines for impulsively started flow around the NACA0012	97
4.5	Contours of velocity magnitude and vertical velocity for impulsively started flow around the NACA0012	98
4.6	Vortex patterns and streamlines for the NACA0012 in ramp-up, $\kappa = 0.0415$	99
4.7	Velocity magnitude contours for the NACA0012 in ramp-up, $\kappa = 0.0415$	102
4.8	Characteristics for the NACA0012 in ramp-up, $\kappa = 0.0415$	103
4.9	Characteristics for the NACA0015 in ramp-up, $\kappa = 0.0487$	104
4.10	Pressure distributions for the NACA0012 and NACA0015 in ramp-up	105
4.11	Comparison of characteristics between the NACA0012 and NACA0015, $\kappa = 0.0415$	106
4.12	Comparison of characteristics between various pitch rates	107
4.13	Tunnel wall effects for impulsively started flow around the NACA0012	108

4.14	Vortex patterns and streamlines for the NACA0012 in ramp-up with wall effect	109
4.15	Comparison of NACA0012 streamlines with and without wall effect .	110
4.16	Comparison of NACA0012 velocity magnitude contours with and without wall effect	111
4.17	Comparison of vertical velocity contours with and without wall effect	112
4.18	Influence of wall effects on characteristics for the NACA0012 in ramp-up, $\kappa = 0.0415$	113
4.19	Correlation of characteristics for the NACA0012 in ramp-up with wall effect	114
4.20	Pressure distributions with and without tunnel wall effect	115
4.21	Vortex patterns and streamlines for the NACA0012 in ramp-up and ramp-down, $\kappa = 0.0415$	116
4.22	Characteristics for the NACA0012 in ramp-up and ramp-down, $\kappa = 0.0415$	117

NOMENCLATURE

A	Area of body (section)
B	Volume within the body
F_b	Volume within the control zone
F_w	Volume outside the control zone
\Im	Imaginary part of complex number
K	Number of sub-panels for each panel
N	Number of panels for the body
\Re	Real part of complex number
Re	Reynolds Number
S	Surface of the body
V	Velocity in the form of complex number
Z	Position in the form of complex number
c	Aerofoil chord
i	Unit imaginary number
\vec{k}	Unit vector, $\vec{k} = \vec{n} \times \vec{s}$
k	Index number of sub-panel within a panel
ℓ	Panel length
p	Pressure
\vec{r}, r	Position vector and its magnitude
\vec{s}, \vec{n}	Unit vector along and normal to the surface
t	Time
\vec{u}	Velocity vector

α	Angle of attack
β	Parameter for velocity profile in creation zone
Ω	Rotational velocity
$\vec{\Psi}, \Psi$	Vector potential and stream function
Γ	Circulation
ρ	Fluid density
γ	Circulation density
κ	Reduced pitch rate $\kappa = \frac{\Omega c}{2V}$
ν	Kinematic viscosity
Δt	Time step
δ	Distance of nascent vortex off the body
ω	Vorticity
σ	Vortex core radius

Subscripts

c	Reference point for the body
i	Index for body
j	Index for panel
k	Index for sub-panel
m	Index for vortices in creation zone, index for moment
n	Normal component
s	Surface
t	Tangential component
w	Index for vortices in wake zone

ACKNOWLEDGMENTS

I am very grateful to my supervisors, Dr. M. Vezza, Dr. F. Coton, and Prof. R.A.McD. Galbraith, who have consistently provided me with encouragement and support in addition to the supervision. Their kindness and tolerance have enabled me to go through the whole process. I am especially grateful to Dr. M. Vezza for making valuable suggestions in the preparation of the thesis, in particular with regard to the upgrading of the language.

I wish to thank Dr. R. Green, from whom I have got many valuable suggestions and help. I also wish to thank Mrs. E. Leitch, Miss M. Simpson, Mrs. E. Garman, and many others in the department for their kindness and help during my study.

I would like to acknowledge the Committee of Vice-Chancellors and Principals (CVCP), the university, and the department for their contributions, through Overseas Research Students Schemes, University Postgraduate Scholarship, and other grants, towards the tuition fees and maintenance fees. The efforts of Prof. Galbraith, Dr. Coton, and Prof. Z. Gao and Prof. S. Wang, of Nanjing University of Aeronautics and Astronautics, in the application process are very much appreciated.

I am indebted to Prof. Gao, Prof. C. Zhang, Prof. X. Xu and their families and many others in the Nanjing University of Aeronautics and Astronautics. Their kindness and care had enriched the prosperity of my life during my study and subsequent work in Nanjing.

Finally, I wish to thank my parents, brothers and sisters, and friends for their enormous support, in particular for their patience and understanding during my long absence.

Chapter 1

INTRODUCTION

The following conclusions were made by Wilbur Wright in a lecture to the Western Society of Engineers on September 18, 1901¹:

That the ratio of drift to lift in well-shaped surfaces is less at angles of incidence of five degrees to 12 degrees than at an angle of three degrees (“Drift” is what we now call “drag”).

That in arched surfaces the center of pressure at 90 degrees is near the center of the surface, but moves slowly forward as the angle becomes less, till a critical angle varying with the shape and depth of the curve is reached, after which it moves rapidly toward the rear till the angle of no lift is found.

That a pair of superposed, or tandem surfaces, have less lift in proportion to drift than either surface separately, even after making allowance for weight and head resistance of the connections.

The above remarks illustrate the Wright brothers’ understanding of wing and aerofoil behaviour, which undoubtedly contributed to their success in achieving mankind’s first sustained, controlled, powered flight in a heavier-than-air machine in 1903.

This knowledge about behaviour of a static aerofoil is not unfamiliar to today’s aerodynamicists and aerospace engineers. This qualitative understanding is actually supported by databases^{2,3}, obtained from extensive wind tunnel experiments, which indicate the quantitative relationships between aerodynamic characteristics (lift, drag and moment) and aerofoil geometry, angle of attack and flow properties. Furthermore, analytic methods have been developed to predict aerofoil flows and associated characteristics. It is also true, however, that technical advances have brought new

aerodynamic phenomena to light, which have driven both the development of experimental and computational methods. Indeed, dynamic stall is one such phenomenon, and is still an active topic of research, both experimentally⁴⁻³⁴ and numerically.³⁵⁻⁶⁰

In this introductory chapter, the theoretical background and classical methods pertaining to the analysis of aerofoil flow are summarised. A presentation is then given of the current understanding and explanation of the dynamic stall phenomenon, based on the observations of numerous researchers. This is followed by a brief review of numerical studies of dynamic stall by means of both grid-dependent methods and vortex methods. A summary to a new vortex method is also given in this chapter. Finally, an outline of the remaining components of the thesis is provided.

1.1 Theoretical background and classical methods

The foundations of theoretical fluid dynamics were moulded by a triumvirate, Daniel Bernoulli, Jean Le Rond d'Alembert and Leonhard Euler in the early eighteenth century, when the momentum relations between pressure and velocity were first established.⁶¹ The applications of the relations, namely Euler and Bernoulli equations, are restricted to steady inviscid flows, with the further restriction of incompressibility in the latter case. In viscous flow, the equivalent momentum relations are described by the Navier-Stokes equations, developed by Navier(1822) and Stokes(1845). These equations form the basis for fluid flow analysis when combined with the mass continuity and energy equations, the former initially published by d'Alembert in 1749 in the form of differential equations, and later developed by Euler into their present form.

Although the governing equations for the motion of fluid have existed for centuries, there is still no general solution to them. This is partly due to the variety of boundary conditions and partly because of the non-linearity of the Navier-Stokes equations themselves. As a result, the search for practicable solutions to these equations is still attracting many researchers, including aerodynamicists, who are mainly interested in

the flows around aerofoils, wings and aircraft.

Idealisation has been commonly practised in order to simplify the complexities associated with the solution of the governing equations for viscous flow. Flow viscosity, compressibility, rotationality and dimensionality have often been used as a means of classifying the flow conditions, and hence informing the simplifications. Assumptions have been made about the entire flow field, as in the case of inviscid and/or incompressible flow, or about specific flow regions, for example a thin viscous boundary layer in an otherwise inviscid flow.

In an inviscid flow, or inviscid flow region, if the flow is also assumed to be incompressible and irrotational, the governing equations are reduced to the Laplace and Bernoulli equations after introduction of a velocity potential, the gradient of which is the velocity. The analysis procedure usually first involves the solution of the Laplace equations for the velocity distribution, incorporating the particular flow boundary conditions, and then, from this velocity field, calculating the pressure distribution via the Bernoulli equations. When solving the Laplace equation, it is common to place basic singular elements on the boundary, such as source, sink, doublet and vortex elements, to utilise the superposition property of the linear equations. The solution is a two-step process, the first step solving for the distribution of the singularities, followed by the calculation of the velocity field. The expression for velocity in terms of the basic singular elements has been well established⁶¹⁻⁶⁴.

If the flow is assumed to be two dimensional, it is more convenient to use the complex potential, of which the real and imaginary parts are the velocity potential and stream function respectively. The complex potential is an analytic function and thus it satisfies the Laplace equation. The complex potential for uniform flow past a circle is well known⁶². Complex geometries can be mapped into a circle by the method of conformal transformations. For a contour like an aerofoil surface, the Schwarz-Christoffel transformation is able to map a polygonal border in the physical plane into the real axis of a new complex plane, with the upper and lower half planes representing the inside and outside regions of the physical plane respectively. It is

then trivial to map a half plane into a disc. Other theories, using similar procedures to this for flow passing an aerofoil, were well summarised by Bryan Thwaites⁶² as theories of first inviscid approximation, in which the surface of the aerofoil is taken as a boundary of the potential flow. The theories described include Theodorsen's theory, Goldstein's approximation, and non-linear theories developed by Lighthill, Weber, and Spencer and Routledge. Thwaites also stressed that, within the strict limitation of the first inviscid approximation, the various theories described "were remarkably accurate and complete" and there seemed little need for new theory.

However, the limitations referred to by Thwaites are so strict as to exclude real flows, due to the neglect of viscosity. For modern requirements there is a need to integrate viscous effects into the flow theories. For unseparated flows, a common extension is to solve the boundary layer equations based on the velocities obtained from the first inviscid approximation, leading to a viscous/inviscid interaction scheme in which the boundary of the potential flow departs from the surface of the aerofoil by a small distance. The result of the boundary layer calculation can then be used to improve the inviscid approximation. Theoretically, this iterative procedure is viable, but it was pointed out that the convergence to the real solution did not necessarily follow due to the errors implicit in the boundary layer approximation. In practice, results of the second inviscid approximation were as good as may be obtained. Following a similar procedure, Preston⁶² obtained a satisfactory velocity distribution at the edge of the boundary layer of the flow over a symmetrical Joukowski aerofoil at zero incidence.

Convergence proofs for models of aerofoil flows based on the above procedures are largely associated with flows which are steady and unseparated. In cases where the flow is separated or unsteady, little is available. Indeed, several difficulties arise if the boundary layer is separated. First, there is no easy way to determine the edge of the separated region, the line that is important for the potential flow calculation. The exact position of the border could probably only be decided once the convergence of the whole calculation has been achieved. Secondly, the boundary layer theory seems

to be inadequate for separated regions, mainly because the dimension of the region normally exceeds what is described as “thin”. With a “thicker” layer, the assumption of constant pressure along the normal is highly questionable. Thirdly, the separated flow might not be steady, even for flow of a static aerofoil at high incidence, when the separated shear layer extends to infinity from the front half of the aerofoil. The unsteadiness becomes more obvious if the flow is unsettled, such as the impulse start of the flow around an aerofoil at incidence, or the aerofoil itself is in motion, as in the case associated with dynamic stall. It therefore becomes clear that the classical theories described above are inadequate for the prediction of unsteady, separated flows.

With the fast growth of computer capabilities in recent years, a numerical approach to the solution of viscous, separated, unsteady flow has attracted much more attention. Prior to the discussion of the progress in numerical prediction of such flows, an outline is given of some of the related physical phenomena, obtained through experimental observation, with emphasis on those associated with dynamic stall.

1.2 Dynamic stall phenomena

It has been shown in numerous experiments^{27,35,65} that the lift curve of an aerofoil continues to increase with increasing incidence beyond the static stall angle, before it collapses, when the aerofoil is pitching up rapidly. The associated phenomena have been collectively named dynamic stall (figure 1.1), to differentiate the process from the stalling of flow over a static aerofoil – static stall. They have been studied by several scientists over the last fifty years, and comprehensive reviews on this subject have been published.^{8,9,11,65} The understanding obtained from these studies of the mechanisms governing dynamic stall has undoubtedly assisted the development of computational methods to predict such events.

The interest in this stall delay phenomenon originally arose in the helicopter industry. It is well known that stalling is a limiting factor of maximum flight speed

of a helicopter. In forward flight, the magnitude of the relative velocity a rotor blade encounters is bigger on the advancing side than on the retreating side. This is, however, counterbalanced by a larger angle of attack on the retreating side to maintain longitudinal balance of the helicopter, and there can be certain blade sections which temporarily experience incidences higher than the static stall value for the aerofoil. As the incidence of a section changes constantly with the rotation of the blade, the stall, if any, is certainly a dynamic one. Accompanying the stall is also a very dramatic negative pitching moment, the periodic change of which affects the flutter characteristic of the helicopter blade and, subsequently, the control system. It is not surprising that the investigation of dynamic stall has its origins in the research into stall flutter of helicopter blades.⁶⁶⁻⁶⁸ There has been an aim that research into dynamic stall would eventually lead to an improvement in helicopter performance and prediction⁶⁹⁻⁷⁵. It is also believed that dynamic stall might be of benefit both in the increase of manoeuvrability of fighters⁷⁶ due to the extra lift coefficient and in the improvement of the efficiency of wind turbines⁷⁷⁻⁸³, which operate in a similar fashion to helicopter rotors.

Stalling of aerofoil flow is considered to initiate with boundary layer separation. For a better appreciation of the flow behaviour during the dynamic stall process, it is appropriate first to review the understanding of boundary layer separation on a static aerofoil. In determining the characteristics of a stalling flow, the position and pressure of the separation bubble are principal factors. According to Gault,⁸⁴ static stall can be categorised as leading edge stall, thin aerofoil stall, and trailing edge stall, with the first of these generally ascribed to all aerofoils that stall abruptly. Trailing edge stall commonly occurs on aerofoils with boundary layer separation that progresses gradually forward from the trailing edge as the angle of attack increases. Thin aerofoil stall, or long bubble separation, develops when a separation bubble appears near the leading edge and lengthens progressively with increasing angle of attack. This process normally leads to a round lift curve peak. Leading edge separation is generally associated with the bursting of a laminar leading edge separation bubble.⁶⁵ When a

separation bubble exists, it is thought that the pressure along its edge is not constant, as assumed in classical Kirchhoff type of flow. It is believed that the pressure on the rear end of the bubble is higher than that on the front half, and that of mainstream.⁶²

Around a pitching aerofoil, however, the focus of attention is extended beyond these early stages of separation. It has been established by numerous experiments that dynamic stall is characterised by the shedding and convection of a vortex like disturbance over the upper surface of an aerofoil, which induces a non-linearly fluctuating pressure field.⁶⁵ The pattern of vortex shedding is dependent on aerofoil shape, Reynolds number, cross-flow effects, and type of motion. However, if reduced frequency, amplitude and maximum incidence are sufficiently high, the qualitative results are independent of all of these parameters. In addition, the unsteady fluctuations in the airloads are normally very

large, corresponding to a well-defined vortex shedding phenomenon. This case is referred to by McCroskey⁶⁵ as “deep stall” as opposed to “light stall”.

Preceding the full formation of the dominant dynamic stall vortex, the nature of the initial boundary layer separation strongly influences the dynamic stall behaviour. After analysing extensive experimental data for several aerofoil profiles, McCroskey et al.⁶⁵ identified four distinctive mechanisms of separation. These were classified into three categories, namely trailing edge stall, leading edge stall and mixed stall, with the latter containing two mechanisms. In trailing edge stall, the moment stall is preceded

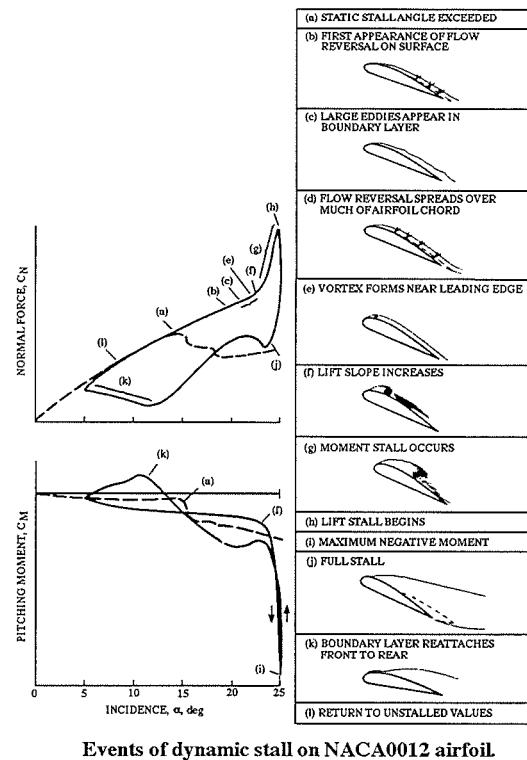


Figure 1.1: Illustration of dynamic stall events from ref.⁸

by a gradual forward movement of flow reversal in the thin layer at the bottom of the boundary layer. When this flow reversal reaches the leading edge region, stall begins gradually and a vortex forms around $x/c = 0.3$ and moves rearward over the aerofoil. This is in contrast to leading edge stall, in which the initial flow breakdown begins at the leading edge and causes an abrupt moment stall as the dynamic leading edge vortex moves rearward closely behind the boundary layer disturbance. Mixed stall behaviour represents a combination of leading edge and trailing edge stall. It has been observed from the tests that a vortex erupts out of the leading edge region while the reverse flow behind this formation moves forward. The two disturbances appear to meet and merge near mid-chord to form a new vortex that continues to move rearward. It has also been observed that a disturbance generated near the quarter chord spreads upstream and downstream, in conjunction with the occurrence of trailing edge separation.

While knowledge of the general flow physics during dynamic stall on an aerofoil has been well advanced over the last few decades through experimental studies, the development of computational methods to predict this phenomenon still poses enormous challenges. This is due not only to the existence of various types of boundary layer separation which need to be simulated, but also the necessity of extending the calculation beyond separation to include the formation, shedding and convection over the upper surface of vortex like disturbances. The simulation of this latter process has exposed the inadequacies of traditional boundary layer theory. It is, however, at this stage of the stalling process that the potential benefit of higher lift coefficients or the potential disadvantage of negative pitch damping appears. The last few decades have seen the development of numerical methods to predict dynamic stall flow. It appears that the fundamental models are based either on grid dependent Navier-Stokes solvers or on vortex methods, with a variety of models to incorporate viscous/turbulent influences. A more detailed discussion on these methods is the subject of the next two sections.

A brief mention is given below of other research developments in the prediction

of dynamic stall. As well as attempts to predict dynamic stall characteristics purely from the flow physics, several empirical or semi-empirical models have been proposed to predict the air loading during dynamic stall.⁸⁵⁻⁸⁸ These models, developed initially in the helicopter industry, employ a variety of basic relations capable of representing the main features of the dynamic stall process. This capability is realised through correlation with extensive airload data obtained from both static and dynamic aerofoil experiments. A review of these methods is available.⁸⁹ Despite the lack of detailed flow analysis, the computational efficiency and reasonable accuracy of these methods make them practical tools for routine analysis of rotor and wind turbine aerodynamics.

In the Beddoes model,^{85,90} time delays were introduced to represent the delay of moment stall and lift stall, compared with the static stall. The delay data came from the analysis of test results and were presented as functions of motion and flow properties. The timing of the major events divides the history into several time periods, for each of which a different simple function was in use to synthesise the variation of lift. In addition, one more function was introduced to describe the shift of centre of pressure between the onset of moment stall and that of lift stall. The model was further modified to improve accuracy.⁸⁸ A number of applications of the Beddoes model have been reported.^{83,91,92}

The Gangwani model^{87,93} is a purely empirical model, based on extensive correlation with unsteady experimental data, instantaneous angles of stall onset, vortex passage over the trailing edge and reattachment. The data, presented with a set of empirical parameters, are synthesised to produce relations defined by a number of empirical coefficients. Although satisfactory correlation with experimental data was published, the choice of the large set of empirical parameters seems to be one of the difficulties in generalisation.

Tran et al.⁸⁶ proposed a model from which the unsteady airloads are obtained from derivative models, the coefficients of which were extracted from unsteady tests by system identification methods. It seems the derivatives should vary with the

change of incidence as the equations are not linear during dynamic stall. This appears either to increase the task of the system identification or otherwise to compromise the accuracy.

In recent years, in addition to the continued accumulation of aerofoil data,^{12,29,94} a number of papers have appeared, particularly of an experimental nature, which concentrate on the flow physics of reattachment,^{4,14,25,30,95} three dimensional effects,^{96,97} and the influence of compressibility^{7,98}. A comprehensive review of the last item has been recently published.⁹ Although significant advances have been made by the development of the experimentally driven empirical and semi-empirical techniques, more emphasis in the future is likely to be placed on correlations derived from more fundamental numerical methods, as part of the drive to reduce the overall cost of testing.

1.3 Numerical approach – grid based methods

Although experimental studies have been, and continue to be, important in developing an understanding of the phenomena which comprise dynamic stall, there is no practical possibility of performing tests on every conceivable combination of parameters. This is one of the main reasons for research into analytical and computational methods of prediction.

It was previously noted that the governing equations for the dynamic stall events were well established. The onus thus lies on finding a solution of the Navier-Stokes equations. At present, analytical solutions for these non-linear partial differential equations, complicated by complex boundary conditions, appear remote. A numerical approach, therefore, provides the only other way forward, and a large research effort has been made in this area.

Among the two main numerical schemes employed for the prediction of dynamic stall, grid based methods and vortex methods, the former have undergone significant development with the appearance of a number of books⁹⁹⁻¹⁰² devoted to the descrip-

tion of the general techniques involved. The general principal of the grid based methods is, through a mesh, to translate the continuous governing equations into algebraic ones, from which a solution is extracted for physical properties such as fluid velocity and pressure, at discretized points – grid points. A distribution of flow properties is often generated throughout the entire flow region via an appropriate interpolation scheme. For the four commonly used algorithms, namely the finite difference, finite volume, finite element and spectral methods, the initial procedure is always to divide the entire flow domain into sub-domains by meshing, generating grid points in the process. In the finite difference method, the partial derivatives of a variable at the grid points are approximated using variable values at the grid points only, and an approximation can be obtained for these values by solving the simultaneous algebraic equations. For the other methods, however, an approximate solution, which satisfies both the boundary conditions and initial conditions, is first assumed through the use of trial functions with unknown coefficients. A residue equation for the unknown coefficients is constructed by substituting the approximate solution into the governing equations.

The capabilities of grid based computational fluid dynamics methods have advanced rapidly in recent years, with new techniques constantly emerging. Reviews of new developments in this area are available.^{103,104} For flow around a static aerofoil, it is now standard practice to calculate the flow field efficiently, even if the flow is compressible and separated. One example is flow over the NACA0012¹⁰⁵ in which the finite element method¹⁰⁶ and adaptive unstructured meshes were employed.

For a pitching aerofoil, the complication is dramatically increased by the constantly changing flow domain which requires an adjustment of the mesh. This is in addition to the need for mesh refinement, in order to adapt to the shifting dynamic stall vortex. Recently, despite the difficulties, several studies have contributed to the solution of dynamic stall flows.

Osswald et al.,⁵⁶ Ghia et al.^{107,108} developed an unsteady Navier-Stokes analysis on a non-inertial, generalised coordinate frame fixed to the body. In this frame they

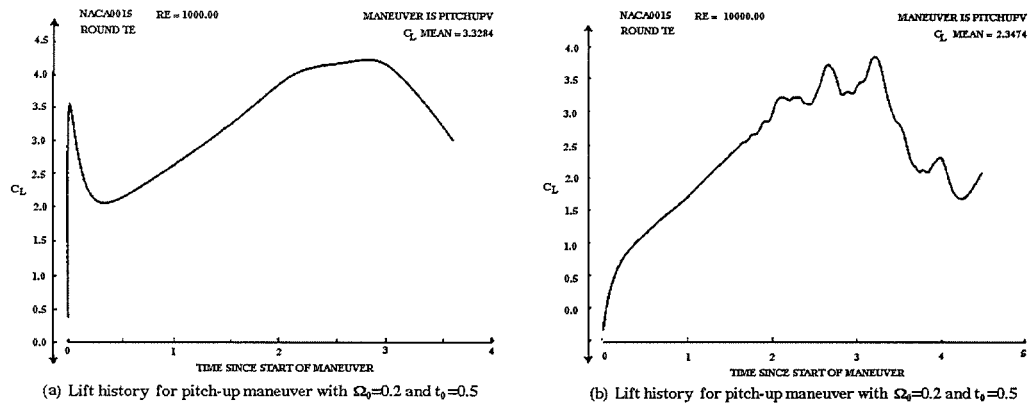


Figure 1.2: Lift histories for pitch-up from ref.⁵⁶

used a velocity-vorticity form of the Navier-Stokes equation that was found to be invariant under the generalised coordinate transformation. As the flow domain remains unchanged in this body fixed coordinate system, a C-grid could be generated in a similar way as for a static aerofoil. The model was used to calculate steady inviscid flow around the NACA0015 at 30° , and the streamlines show good agreement with those obtaining by using the Schwarz-Christoffel mapping technique. For pitching up motion, a dynamic vortex was generated over the upper surface, as indicated by both the streamline and vorticity contours. No comparison of lift and moment coefficients with experimental results was given. Indeed, with variation in Reynolds number, the time histories (figure 1.2) obtained seem quite different.⁵⁶

Visbal et al.^{49,50} utilised a general time-dependent coordinate transformation to match the motion of the body, while the governing equations were still formulated in an inertial frame of reference. A nearly orthogonal boundary-fitted grid, ri-

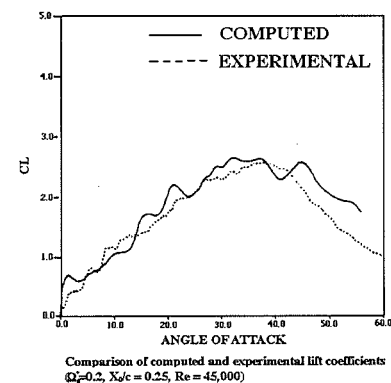


Figure 1.3: Lift coefficients from ref.⁴⁹

gently attached to the aerofoil, was generated, and both the mass-averaged Navier-Stokes equations and a Baldwin-Lomax algebraic eddy viscosity model was employed to simulate the unsteady flow. The comparison of lift and moment coefficients with experimental data (figure 1.3) shows reasonably good agreement, although discrepancies are apparent in the post-stall region. It is also not clear why lift coefficients of more than 0.5 were predicted for angles of attack between 0° and 3° , at which the flow would normally be attached. Based on the computational results, the effects of pitch rate on the airload coefficients, and the effects of Mach number on the lift coefficient and stalling process were analysed.⁵⁰

Reu et al.³⁷ developed an approach that solved an integral form of the Navier-Stokes equations. The model used coupled structured and unstructured grids effectively to handle the unsteady boundary layer. A structured, highly stretched, body-conforming grid was generated in the region around an aerofoil while an unstructured grid was used in the remaining region. As the structured grid moved with the aerofoil and the far field unstructured grid was fixed, there was a borderline between the moving and stationary patches. For this, two proposals were examined, as described below. The first was the DSUG method that included the dividing line between the two grids. The unstructured grid near this boundary was used to patch the gap caused by the motion at each time step, and no interpolation was therefore required. The second approach, referred to as the PSUG method, was to use a slip boundary within the region represented by the unstructured grid. It was concluded, however, that this latter approach was inadequate for the prediction of unsteady wake flow due

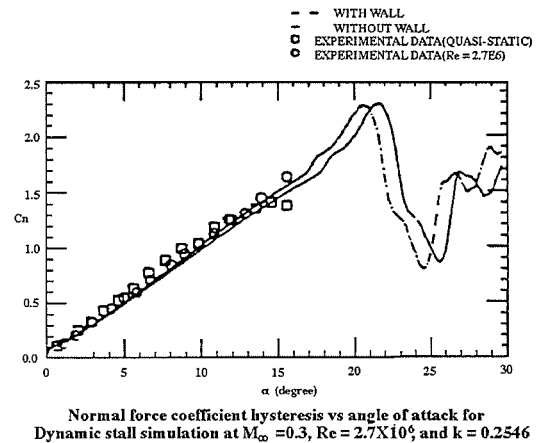


Figure 1.4: Normal force coefficients from ref.³⁷

to the discontinuity across the boundary, despite the use of interpolations to convey the data. A result for the NACA0012 using the DSUG method was obtained and the pressure distribution from 0° to 29° was presented, although comparisons with experimental data¹⁰⁹ were only provided up to 15.54° , the angle before the dynamic stall vortex becomes dominant. The computation did, however, predict the formation of a dynamic stall vortex and its shift downstream with increasing angle of attack. The effect of the addition of wind tunnel walls was also predicted, indicating an earlier stall (figure 1.4).

Tuncer et al.⁵¹ proposed two models to numerically study the flow around oscillating aerofoils, which comprised full viscous analysis and simplified vortical analysis. The latter approach only had the vortex shedding from the trailing edge, and was therefore unable to predict the dynamic stall vortex that is believed to initiate near the leading edge. In the viscous analysis, the vorticity transport equation was solved along with a Biot-Savart velocity expression in terms of the vorticity field and boundary conditions. The Baldwin-Lomax two layer algebraic eddy viscosity model¹¹⁰ was incorporated into the numerical method. The NACA0012 aerofoil profile was approximated by a Joukowski transformation of a unit circle in the ζ plane in which the solution was performed by using an O-grid to discretize the governing equations and the velocity relations. From the instantaneous streamlines and vorticity contours, the computation indicated the formation of the dynamic stall vortex near the leading edge. The vortex convected downstream during pitch-up and

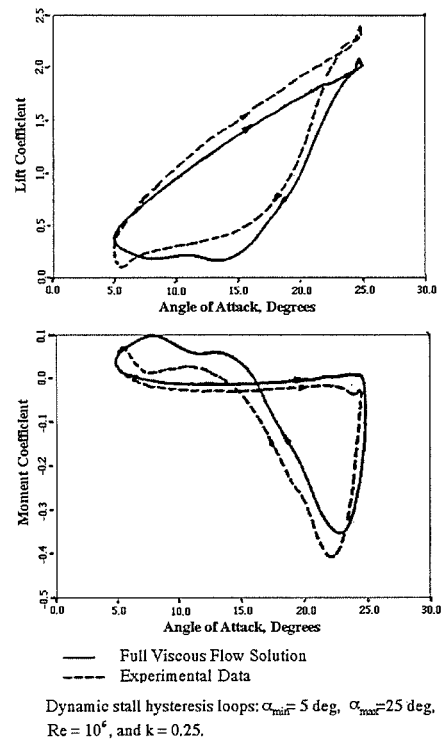


Figure 1.5: Lift and moment coefficients from ref.⁵¹

the flow reattached during pitch-down. The deep stall hysteresis loops in lift, drag, and moment coefficients were captured by the computation (figure 1.5), although discrepancies exist when compared with experimental data.

Wernert et al.,¹⁹ Geissler et al.⁴⁴ employed the approximate-factorisation implicit method¹¹¹ to solve the Navier-Stokes equations in a curvilinear aerofoil fitted coordinate system that deformed with respect to time. The Baldwin-Lomax algebraic turbulence model¹¹⁰ was incorporated into the method. The computed velocity vector field, streamlines and vorticity contours for the NACA0012 undergoing pitching oscillations were presented, together with those from PIV experiments. The main features of dynamic stall were captured.

Tuncer et al.¹¹² proposed a viscous-inviscid interaction method that partitioned the entire computational domain into near-field and far-field zones. The near-field zone encompassed the boundary layer and separated flow zones, within which the full Navier-Stokes equations were solved. For flow in the far-field zone, a potential flow solution method was employed, with isolated vortices shedding from the near-field zone. Lift and drag coefficient histories were presented, indicating good agreement with experiments for a sinusoidally oscillating aerofoil up to a maximum angle of attack of 10° , below that at which stall is expected. Comparisons of static lift coefficients with ex-

perimental data were also given for the case where the full viscous computation was performed on the entire field. It is interesting to note that, although good agreement was shown between the two computational models, the computational data were much bigger than the those obtained from experiments (figure 1.6).

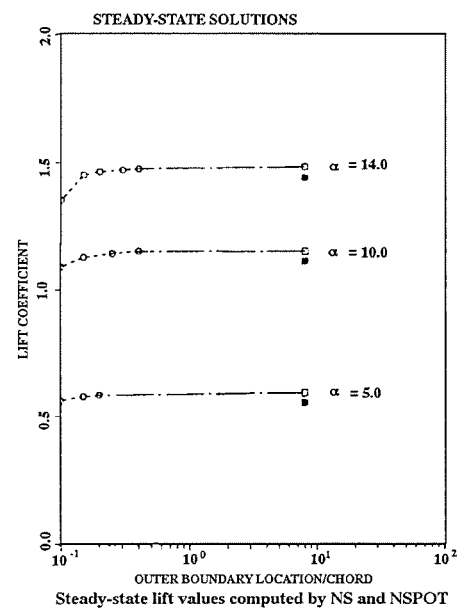


Figure 1.6: Steady-state lift coefficients from ref.¹¹²

Kim et al.⁵⁸ used a finite volume method to solve the Navier-Stokes equations expressed in an arbitrary Lagrangian-Eulerian coordinate system. Flow turbulence was modelled by a multiple time-scale turbulence equation. A new sheared moving mesh was generated algebraically at each time step. Streamlines and turbulent viscosity contours were presented which indicated the process of dynamic stall.

Choudhuri et al.^{42,113} numerically studied unsteady leading edge separation on a pitching aerofoil up to the stage of dynamic stall vortex formation. Two algorithms were employed for comparison, both of which were second order accurate: a structured grid algorithm that utilised a structured, boundary fitted C-grid; an unstructured grid algorithm that employed triangular elements. Results for the NACA0012 were presented. The incidence variation of lift, moment and drag coefficients were compared for

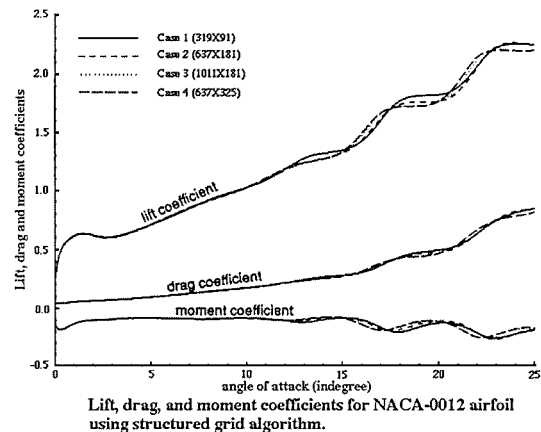


Figure 1.7: Aerodynamic coefficients from ref.⁴²

the two algorithms, but no comparison with experiments was provided. In the calculated instantaneous flow fields, recirculating regions near the leading edge were shown, and critical points were proposed and identified. However, although the formation and convection of the dynamic stall vortex was shown, the vortex induced lift and pitching moment were not evident (figure 1.7). Similar to the results from Visbal's model, the lift coefficients at low angles of attack (0° to 3°) seem quite high.

Despite the differences in detail, the common feature of the methods above is the use of a grid to solve the Navier-Stokes equations. Turbulence models were integrated into some of the methods. All of the methods were able to capture the dynamic stall vortex, but only some predicted airloads. All of the methods have contributed to the advancement in the prediction of dynamic stall. However, when

comparison of numerically predicted airloads were made with experimental data, discrepancies existed, especially in the post-stall region. This highlights the necessity for further research. Considering the dominant influence of the dynamic stall vortex revealed by numerous experimental studies, techniques collectively known as vortex methods would appear to offer useful alternatives to grid based methods, and these are discussed below.

1.4 Numerical approach – vortex methods

Since the realisation by Helmholtz, almost one and half centuries ago, that flows with vorticity could be modelled with vortices of appropriate circulation and infinitely small cross section, computational methods with vortices have been under constant development. This process has accelerated with the advancement of computer technology over the last few decades, which have seen the appearance of numerous new models aiming to identify, solve or eliminate the problems associated with the implementation of Helmholtz's ideas in real flows. The quantity of publications available prohibits a detailed review here. However, comprehensive reviews have been produced.^{114–122} which provide the background of the methods together with a summary and assessment of the existing techniques.

The essence of vortex methods is the representation, through discretization, of the continuous distribution of vorticity by an ensemble of vortices imbedded in a potential flow. The vortices are described in a Lagrangian frame of reference and tracked numerically through the flow field. If the flow is incompressible, the velocity of an individual vortex can be determined in accordance with the Biot-Savart law, or by the Green's function method in conjunction with the boundary conditions. The same methods apply to the entire flow velocity field and, therefore, when the distribution of vortices and boundary conditions are known, the flow is defined.

The advantages of vortex methods come from the Lagrangian description of the vortices. These are a grid free computation, the need for velocity computation only

at the vortex locations, exact treatment of boundary conditions at infinity, the need to deal only with vorticity rather than with velocity and pressure, and many others. These advantages are, however, counterbalanced among other things by the difficulties with velocity computation which arise from the singularity of a point vortex and the cost proportional to the square of the number of vortices. Attempts to find solutions to these difficulties have been made, details of which have been published.¹¹⁴

The theoretical basis of vortex methods lies in the flow momentum equations. Once vorticity is defined as the curl of velocity, the velocity-pressure form of the Navier-Stokes equations can be translated into the vorticity transport equations, which state that in an inviscid fluid, vorticity is a kinematic property of a given fluid particle. Such particles can undergo convection and deformation only, which leads to the Lagrangian description of vorticity evolution. In viscous flow, the transport equations determine how the vorticity produced at a boundary is carried away by convection and diffusion. In homogeneous fluids, vorticity is generated only at the boundary of fluid regions. Regarding the generation of vorticity, Morton¹²³ concluded that “vorticity generation results from tangential acceleration of a boundary, from tangential initiation of boundary motion and from tangential pressure gradients acting along the boundary”.

The introduction of cutoff functions for vortices to represent some sort of finite vorticity distribution, like vorticity blobs or vortex balls, serves the purposes of eliminating the singular nature of a point vortex and alleviating the instabilities encountered in vortex computations. Several cutoff functions have been proposed and a list of commonly used ones is available.¹²⁴ The most extensively used functions are those based on the Rankine or Lamb vortices. The former assumes a constant vorticity distribution within the core radius and the latter represents an exact solution of the Navier-Stokes equations for an isolated vortex. However, the advantage arising from the solution provided by the Lamb core is offset by the fact that the result from an assembly of vortices is not the same as that obtained from a sum of individual particles, as the non-linear nature of the equations does not permit the superposition

of the vortex field.

In the definition of cutoff functions, the core radius is a major parameter. Two types of scheme have been used extensively for the evolution of this parameter, employing either a time dependent radius or a fixed radius. The core expansion technique seems to reflect the effect of viscous diffusion, but it has been argued, without the provision of error limits, that the scheme does not converge to the equations of motion except for certain special flows.¹²⁵ The fixed core technique, on other hand, violates the Euler equations and Helmholtz's laws. It has been emphasised that "the use of blobs must be regarded as a mathematical artifice to limit the large velocities induced by vortices in their immediate neighbourhood".¹¹⁴ For this reason, instead of using a complicated expression for the velocity calculation in two dimensional flow, desingularization was also proposed by multiplying the velocity of a point vortex with an artificial smoothing parameter $\frac{d^2}{(d^2+\delta^2)}$, d being the distance from the vortex point and δ being a parameter similar to core radius.¹²⁶⁻¹²⁹

Vortex amalgamation is also quite commonly employed in vortex computations^{35,53} as a smoothing technique as well as a cost saving exercise. This is achieved through the avoidance of unrealistically large velocities and a reduction in the overall number of vortices in the computation. However, as the approximation introduced by amalgamation is irreversible, it has been pointed out that merging of vortices with large circulation, large inter-vortex spacing and small distances from the body should be strongly discouraged.¹¹⁴

As alternatives to, or complementary to, vortex amalgamation, numerous schemes have been developed to reduce the CPU time involved in the vortex interactions. The discrete vortex in cell,¹³⁰ dipole-in-cell,¹³¹ Anderson's method of local corrections^{132,133} and multipole method¹³⁴⁻¹³⁶ all demonstrate the possibility of speeding up the most expensive part of the computation. The common theme of these schemes is the targeting of the influence of long-range vortices by either grouping some into single or dual vortices, or by utilising some sort of mesh and/or Taylor expansion in the computation. The interactions between vortices close to each other are computed

directly.

Instead of trying to reduce CPU time by reducing the direct summation cost of the Biot-Savart interaction, the vortex-in-cell method^{137,138} replaces the vortices at vortex points with vorticity distributed on a grid, maintaining the circulation of the original vortices. The CPU time of the interaction is proportional to the number of grid points rather than the number of vortices. Since it is possible to choose far less grid points than vortices a reduction in CPU time can be achieved. In addition to the above methods, parallel computation techniques have been developed for vortex methods in recent years.¹³⁹⁻¹⁴¹

The vortex method has been shown to be a useful tool for solving the Euler equations for incompressible inviscid flow. When solving the Navier-Stokes equations for viscous flow, however, the appearance of the diffusion term $\nu \nabla^2 \omega$ in the vorticity transport equations poses an enormous challenge to Lagrangian algorithms. To tackle this, three variations of the inviscid algorithm have been proposed: the random vortex method;¹⁴² the core expansion method;¹⁴³ the particle strength exchange algorithm.¹⁴⁴⁻¹⁴⁷ In these methods, the vorticity transport equations are split into two parts, each governed by the Euler equations and diffusion equation respectively. This is known as the operator splitting method, which simulates convection and diffusion sequentially rather than simultaneously. Whatever the method, a particle first advances in accordance with the convection prescribed by the Euler equations. The difference between the various methods appears in the simulation of diffusion. The core expansion method employs the fact that a Gaussian vortex core simulates an exact solution of the diffusion equation for a single vortex, but Greengard¹²⁵ concluded that the method solved the Euler equations incorrectly. The random vortex method adds a random walk to the particles at each time step, and approximates the equations correctly in a statistical sense. The proofs of accuracy have been provided by several investigators¹⁴⁸⁻¹⁵² although it appears that the proofs pertain to laminar flows and the absence of an interior boundary.¹¹⁴ Instead of maintaining the circulation of every particle, the particle strength exchange algorithm adjusts the circulation

in accordance with the diffusion equation, or assigns circulation to mesh points close to the particles. Despite these developments, it appears that the capacity of current techniques for simulating diffusion are still limited to the purely viscous case. It could be argued that with enough particles the vortex method could provide a direct simulation of small scale turbulence, however the number of particles required is likely to be prohibitive. Future developments in this area may lie in the association of the vortex method with techniques developed for large eddy simulation models, in which the vorticity field provides the input for the calculation of the spatial distribution of eddy viscosity.

When a body is imbedded in a flow, the surface of the body forms part of the flow boundary. On this portion of the boundary, the physical conditions of no-penetration and no-slip should normally be satisfied. In a similar manner to that previously discussed for the inviscid approximation, surface singularity distributions such as vortex or doublet sheets have been quite commonly used to satisfy the no-penetration condition. These distributions are usually divided into singularity segments over which the strength is assumed to vary piecewise constantly, piecewise linearly or in some other manner. Therefore, the nodal values describe the distributions, and these are determined by solving a set of simultaneous linear equations. As opposed to the inviscid approximation, the existence of wake vortices within an otherwise potential flow influences the normal velocity equation and hence the singularity distribution. If the flow is two dimensional, a common technique has been to introduce image vortices to cancel the normal velocity for simple geometric boundaries, like plates or circles. For complex geometries, a transformation mapping can be used, although the Routh rule is required to obtain the correct velocity in the new plane.

The vortices imbedded in the otherwise potential flow originate from the boundary. It follows that the boundary is the source of flow vorticity, from which the vortices are obtained by discretization. Such methods involve the generation of nascent vortices near the boundary at each time step. Two major parameters, strength and position, describe the shedding process from a surface, sharp edge or other separation points

obtained from experiments or boundary layer calculation.

For vortex shedding from a known separation point, it has been proposed that the shedding rate of vorticity is $\frac{d\Gamma}{dt} = \frac{1}{2}U_s^2$ with U_s as the shedding velocity. It has been suggested that the position of the nascent vortices should be chosen to satisfy the Kutta condition at the sharp edge.¹⁵³ A sharp edge shedding model has also been proposed using a vortex sheet whose length is associated with the local velocity and whose strength is determined by the Kutta condition. For unsteady flows, Sears proposed that the time rate of change of circulation is $(0.5U_s^2 - U_sU_\theta)$ where U_s is the outer flow velocity at separation and U_θ is the speed of the separation point.¹⁵⁴

In the case of surface shedding, Chorin proposed a method that creates nascent vortices near the boundary at each time step to enforce the no-slip boundary condition.^{142,155} The vortices then advance in accordance with the Euler equations and random walk algorithm. Variations of the method have been developed describing a different relationship between the nascent vortices and the boundary.^{156,157} An alternative algorithm was recently proposed which alters the strength of existing vortex blobs in the vicinity of the boundary to simulate the shedding of vorticity from the boundary.^{146,147}

The preceding discussion on the background and techniques behind the vortex method has illustrated that the method has developed to the stage where its application to the computation of aerofoil flows is practicable. Most of the applications specify the trailing edge as the vortex shedding point, or a point upon the upper surface determined from a boundary layer calculation.

Kim¹⁵⁸ proposed a method for solving the unsteady, incompressible, inviscid two-dimensional flow over an aerofoil by placing continuous vorticity on the aerofoil surface, with vortices shedding from the trailing edge at each time step. The strength of the shed vortex, whose initial position was not made clear, is determined by equalizing the pressure on the upper and lower surfaces at the trailing edge. The unsteady flow case presented was that of an aerofoil in plunge motion. As the model is inviscid, no viscous effects were included, and as the incidence remained low for the case

presented, no surface separation would have been expected.

Another inviscid flow simulation was performed by Choi,⁴¹ who developed a conformal mapping technique to analyse a similar flow. In his model, however, a nascent vortex is created near the trailing edge at each time step. The position of the vortex is arbitrarily specified and its strength is determined by satisfying the Kutta condition of zero velocity at the sharp edge.

In Tuncer's simplified vortical flow analysis,⁵¹ no diffusion of vorticity was considered. The model applies to unseparated flow, so vorticity is shed from the trailing edge only. The position and strength of the nascent vortex are determined from the conservation of momentum and mass in a sufficiently small control volume at the trailing edge. The computational lift coefficient for an oscillating aerofoil with maximum incidence below the static stall angle shows reasonably good agreement with experimental data.

Ham³⁵ used classical potential theory to calculate the unsteady aerodynamic loading on an aerofoil during dynamic stall. The aerofoil was modelled by a flat plate, with emission of free vortex elements from both the leading and trailing edges. Their strengths are calculated by enforcing stagnation at these points. This highly simplified model illustrated the variations in aerodynamic loading and main flow features during the pitching of the plate although, as expected, accuracy was not high.

In a viscous simulation of the separated flow around an oscillating aerofoil using a vortex method, Spalart divided the flow domain into inner and outer regions.⁵³ The flow in the inner region was treated as viscous and was represented by the boundary layer equations, which were solved by employing the finite difference method together with the Baldwin-Lomax turbulence model. The flow in the outer region was regarded as inviscid and the Euler equations were solved by a vortex method. Across the interface between the two regions, velocity continuity was maintained. This resulted in the introduction of a vortex sheet along the zonal interface. With the instantaneous pressure distribution calculated from the outer flow at each time step, the separation point was predicted by the boundary layer computation. The release of vortices

from the inner zone was suppressed along the segment between the leading edge and the separation point. In so doing, only the separation which progresses from the trailing edge was evident. The vortex pattern predicted for dynamic stall flow was representative, but discrepancies existed in the airload comparisons with experimental data, especially for angles of attack at which the influence of the dynamic stall vortex was expected to be dominant.

In a variation of Chorin's method,¹⁵⁵ Shih used the random vortex method to study dynamic stall flow of an aerofoil.²¹ The surface of the aerofoil was mapped into a circle by a generalised von Mises transform mapping, and mirror vortices were introduced to maintain zero relative normal velocity at the surface. To maintain the no-slip boundary condition, vortices were added near the boundary at a distance of 0.675 times the random step size

$\sqrt{2\nu \Delta t}$. Each vortex advanced with the same velocity as the associated flow particle, with the addition of a random walk during the time step. At each new time step, vortices within twice the creation distance of the boundary were removed and a ring of new vortices created. The instantaneous streamline pattern and distribution of vortices for the NACA0012 resembled the velocity field from experiment in terms of the structure of the dynamic stall vortex. No airload data were presented.

Instead of using vortex sheets as in Chorin's method,¹⁵⁵ Huyer et al.¹⁵⁹ proposed a model which employed uniform rectangular elements to represent vorti-

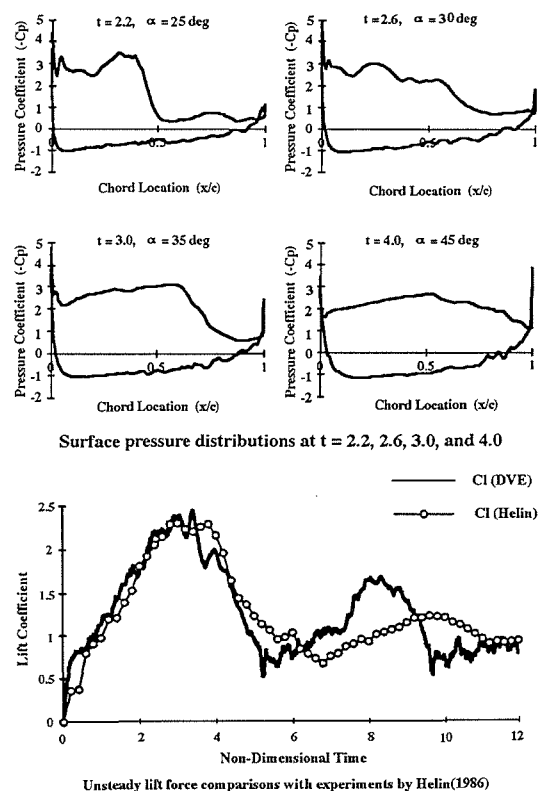


Figure 1.8: Pressure and lift coefficient from ref.¹⁵⁹

city near the body surface. The elements underwent convection and viscous diffusion, simulated by random walk, in the same fashion as for vortex sheets, and subsequently shrank into vortices after a number of time steps. In its application to pitching aerofoil flow, the formation and convection of the dynamic stall vortex were captured. The value and timing of the maximum lift coefficient were in good agreement with experiment, although there was no explanation of the discrepancy at lower angles of attack prior to stalling (figure 1.8)

The development of the vortex method and its application to aerofoils indicate its suitability for the simulation of unsteady separated flows, especially vortex dominated flows typical of dynamic stall. However, the discrepancies between the calculated and experimental airloads, or the absence of the airload data altogether, suggest the need for further improvements in the method.

1.5 Summary of present method

The development and application of a vortex model is presented herein to simulate unsteady separated flow around a pitching aerofoil. Through the division of the flow domain into a creation zone and a wake zone, the model is capable of simulating general vortex shedding from a surface rather than from points predetermined by some other method, as is the case for most of the other models. The model is also extended to incorporate the influence of external constraints such as those provided by wind tunnel walls. The application of the method to pitching aerofoil flow produces encouraging results both in regard to the flow patterns obtained and the airloads predicted.

As a vortex method, vorticity in both zones is represented by discretized vortices, but in a different manner. Within the creation zone, discretization is performed at fixed points along a line that is “parallel” to the surface. A piecewise linear distribution of the vortex sheet strength is assumed within the creation zone over the panels used to discretize the body surface. The vortex strengths are determined by

implementing the no-penetration boundary condition expressed in terms of zero mass flux through each panel. Within the wake zone, on the other hand, vorticity is discretized in accordance with the Lagrangian description of the vortices. During a time step, subject to an addition of random walks for viscous diffusion,¹⁴² vortices in both zones convect with the velocity of the particles to reflect the convection and diffusion of vorticity. Those remaining in the wake zone retain their identity, while vorticity within the creation zone is discretized together with the new vorticity generated at the boundary. The shedding of vorticity across the interface from creation zone to wake zone is represented by newly created vortices in the wake zone the strength of which reflects the amount of shedding.

Amalgamation is employed to reduce the total number of vortices in the velocity summation which in turn reduces the CPU time. As vortices which are shed near the leading edge have potential to return close to the surface, the amalgamation is only performed for those vortices which have passed the trailing edge. The amalgamation of two vortices is subject to a criterion similar to the one used by Spalart,⁵³ but a variation is introduced to reduce the CPU time of the merging process and to maintain a convergent Taylor series.

Chapter 2 details the governing equations and velocity expression in integral form, which includes the influence of the moving boundary caused by the motion of the aerofoil. The derivation is sufficiently general to include flow with external constraints such as wind tunnel walls. In chapter 3, the numerical implementation of the governing equations for the vortex method is presented. Results for the NACA0012 and NACA0015 undergoing impulse start, ramp-up, ramp-up and ramp-down motion are presented in chapter 4 in the form of vortex patterns and velocity/streamline diagrams. Also presented are plots of normal force, tangential force and pitching moment against time and angle of attack, as well as selected instantaneous pressure distributions. The results with the influence of wind tunnel walls are also presented in this chapter. Chapter 5 is intended to summarize the main conclusions of the study and suggest future developments.

Chapter 2

MATHEMATICAL FORMULATION

The main dynamic properties of interest include the velocity and static pressure. The determination of such parameters at relevant positions within the flow field for any instant is the main task of flow analysis through numerical simulation.

In this chapter, the relationships between the main parameters in two dimensional incompressible flows are presented in both the forms of the Navier-Stokes equation and the vorticity transport equation. Emphasis has been placed on the limited vortical flow region and the influence of the time dependent boundary caused by the moving body. The velocity field is expressed in an integral form after incorporating the boundary conditions of undisturbed infinite flow, no-slip and no-penetration on the moving inner boundary and the exterior body surface. The pressure gradient is obtained in terms of the rate of change of vorticity on the moving body surface, and then integrated into the force and moment actions on the body.

2.1 Governing equations

The following continuity and Navier-Stokes equations govern incompressible flows:

$$\nabla \cdot \vec{\mathbf{u}} = 0 \quad (2.1)$$

$$\frac{\partial \vec{\mathbf{u}}}{\partial t} + (\vec{\mathbf{u}} \cdot \nabla) \vec{\mathbf{u}} = -\frac{1}{\rho} \nabla p + \nu \nabla^2 \vec{\mathbf{u}} \quad (2.2)$$

Both the velocity $\vec{\mathbf{u}}(x, y, z, t)$ and pressure $p(x, y, z, t)$ are functions of the position (x, y, z) and time t . The flow density ρ and kinematic viscosity ν are constant in the flows of interest due to the assumptions of the incompressibility and homogeneity.

Taking the curl of the momentum equation results in the velocity-vorticity form corresponding to the vorticity transport equation, which for two dimensional flow is

$$\frac{\partial \vec{\omega}}{\partial t} + (\vec{\mathbf{u}} \cdot \nabla) \vec{\omega} = \nu \nabla^2 \vec{\omega} \quad (2.3)$$

The vorticity $\vec{\omega}$ is defined as

$$\vec{\omega} = \nabla \times \vec{\mathbf{u}} \quad (2.4)$$

This is also a function of position (x, y) and time t and can be written as $\vec{\omega} = \vec{\mathbf{k}}\omega$ in two dimensional flow. Note that the distortion term $(\vec{\omega} \cdot \nabla) \vec{\mathbf{u}}$ only arises in three dimensional flows.

It can be seen that in the vorticity transport equation, pressure does not appear explicitly. The change in vorticity at a particular position is influenced by the surrounding vorticity and the velocity of the flow, either through convection or diffusion.

By defining the Reynolds number

$$Re = \frac{u_\infty L}{\nu} \quad (2.5)$$

where L is a characteristic length, usually the chord length when the body is an aerofoil, and u_∞ is the velocity at infinity, the vorticity transport equation becomes, for unity L and u_∞ ,

$$\frac{\partial \omega}{\partial t} + (\vec{\mathbf{u}} \cdot \nabla) \omega = \frac{1}{Re} \nabla^2 \omega \quad (2.6)$$

which shows that with increasing Reynolds number, the influence of viscous diffusion $\frac{1}{Re} \nabla^2 \omega$ becomes less important while convection $(\vec{\mathbf{u}} \cdot \nabla) \omega$ increasingly dominates the time change rate of the vorticity.

One extreme case is when vorticity diffusion becomes insignificant. The vorticity transport equation reduces to

$$\frac{D\omega}{Dt} = 0 \quad (2.7)$$

This indicates that the vorticity associated with a particular flow particle is unchanged and, therefore, the vorticity forms one of the conserved properties of the flow particles.

In addition the velocity of transportation of the vorticity is equal to that of the particles.

The Navier-Stokes and vorticity transport equations do not have unique solutions unless the boundary and initial conditions are implemented. The kinematic conditions of no-slip and no-penetration on the surface of the solid body are commonly used in viscous flow. These require the flow particles on the surface to have the same velocity as that of the body point. For unrestricted flow, the outer boundary lies at infinity, where the flow is undisturbed. For constrained flow, some boundary conditions similar to those for the original body are required for the external physical constraints.

2.2 Influence of moving body

The incorporation of body motion differentiates the flow simulation from that associated with stationary bodies. The flow is time dependent due to the time varying internal boundary, which adds to the complexity of both the surface integrals, when Green's theorem is employed, and the pressure relations.

In accordance with the kinematics, the velocity of an individual point \vec{r} on the boundary of the body i can easily be described as

$$\vec{u}_i = \vec{u}_{c_i} + \Omega_i \vec{k} \times (\vec{r} - \vec{r}_{c_i}) \text{ on } S_i \quad (2.8)$$

Reference point \vec{r}_{c_i} is a point fixed on the body i , \vec{u}_{c_i} is the velocity of the fixed point and $\vec{\Omega}$ is the rotational velocity of the body, as shown in figure 2.1.

The velocity \vec{u}_i on the boundary is also the velocity of the attached flow particle as required by the no-slip and no-penetration boundary conditions. To evaluate the influence of the velocity of the moving boundary S_i on the flow, the solenoidal velocity

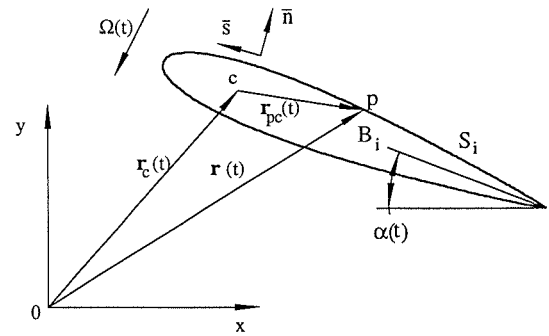


Figure 2.1: Reference coordinate system

field described by the above equation is applied within the area of body B_i . Such a velocity distribution is equivalent to that of the solid body in transit and rotational motion. It is obvious that the boundary condition is fully satisfied.

The velocity field has uniform vorticity within the defined area B_i

$$\omega_i = \vec{k} \cdot (\nabla \times \vec{u}_i) = 2\Omega_i \quad (2.9)$$

which is twice the rotational velocity. From the vorticity and Stokes' Theorem, the circulation of velocity around the boundary contour can be easily obtained as

$$\Gamma_i = \oint_{S_i} \vec{u}_i \cdot \vec{s} dS_i = \iint_{B_i} (\nabla \times \vec{u}_i) \cdot \vec{k} dB_i = 2\Omega_i A_i \quad (2.10)$$

where A_i is the area of B_i .

The solenoidal property of the velocity field in B_i , $\nabla \cdot \vec{u}_i = 0$, indicates there exists a stream function ψ_i such that $\vec{u}_i = \nabla \times (\vec{k}\psi_i)$ and $\vec{k} \cdot \nabla \psi_i = 0$. Such ψ_i is a solution of the following Poisson equation

$$\nabla^2 \psi_i = -2\Omega_i \quad (2.11)$$

and satisfies both the boundary requirements

$$\begin{aligned} \vec{n} \cdot \nabla \psi_i &= -\vec{s} \cdot [\vec{u}_{c_i} + \Omega_i \vec{k} \times (\vec{r} - \vec{r}_{c_i})] \\ \vec{s} \cdot \nabla \psi_i &= \vec{n} \cdot [\vec{u}_{c_i} + \Omega_i \vec{k} \times (\vec{r} - \vec{r}_{c_i})] \text{ on } S_i \end{aligned} \quad (2.12)$$

It can be proved that the two boundary conditions are compatible and either one is enough to produce a unique solution for the Poisson equation up to a constant. Let ψ'_i be another solution of the equation. $(\psi_i - \psi'_i)$ should satisfy the Laplace equation in B_i . On the boundary, either the corresponding Neumann condition of zero normal gradient of $(\psi_i - \psi'_i)$, or the Dirichlet condition of constant $(\psi_i - \psi'_i)$, requires constant $(\psi_i - \psi'_i)$ throughout the whole of B_i . Uniqueness of ψ_i suggests that the two boundary conditions imply each other as ψ_i always satisfies both.

By using Green's theorem, one can prove ψ_i satisfies the following relationship

$$\oint_{S_i} (\varphi \nabla \psi_i - \psi_i \nabla \varphi) \cdot \vec{n} dS_i = \iint_{B_i} \varphi \nabla^2 \psi_i dB_i = - \iint_{B_i} 2\Omega_i \varphi dB_i \quad (2.13)$$

where $\varphi = \frac{1}{2\pi} \ln |\vec{\mathbf{r}} - \vec{\mathbf{r}}_p|$, and $\vec{\mathbf{r}}_p \notin B_i$. $\nabla^2 \varphi = 0$ when $\vec{\mathbf{r}} \neq \vec{\mathbf{r}}_p$

The equation evaluates the surface integral containing the values of ψ_i on the boundary. This integral will later be used to obtain the stream function in the exterior flow field.

The acceleration accompanying boundary movement produces extra forces acting on the flow particles, resulting in additional surface force gradients.

The acceleration of the boundary is expressed as

$$\frac{D\vec{\mathbf{u}}_i}{Dt} = \frac{D\vec{\mathbf{u}}_{c_i}}{Dt} + \frac{D\Omega_i}{Dt} \vec{\mathbf{k}} \times (\vec{\mathbf{r}} - \vec{\mathbf{r}}_{c_i}) - \Omega_i^2 (\vec{\mathbf{r}} - \vec{\mathbf{r}}_{c_i}) \quad (2.14)$$

The three components are due to linear acceleration of the reference point, rotational acceleration and centripetal acceleration, and are a consequence of the body kinematics.

The component tangential to the boundary

$$\vec{\mathbf{s}} \cdot \frac{D\vec{\mathbf{u}}_i}{Dt} = \vec{\mathbf{s}} \cdot \frac{D\vec{\mathbf{u}}_{c_i}}{Dt} + \frac{D\Omega_i}{Dt} \vec{\mathbf{n}} \cdot (\vec{\mathbf{r}} - \vec{\mathbf{r}}_{c_i}) - \Omega_i^2 \vec{\mathbf{s}} \cdot (\vec{\mathbf{r}} - \vec{\mathbf{r}}_{c_i}) \quad (2.15)$$

directly influences the pressure gradient along the boundary.

2.3 Influence of external boundary

Most of the experimental studies of aerofoil flows are conducted in wind tunnels. The influence of the wind tunnel is regarded as insignificant when the outer constraints are far enough from the area of most interest and the blockage is relatively small. Such cases may include tests at low angles of attack in large wind tunnels. However, dynamic stall normally occurs at higher angles of attack and the presence of the dominant dynamic stall vortex increases the influence of any external boundaries due to the expanded region of flow disturbance.

Compared with unbounded flows, the main effect of wind tunnel walls is the limitation of the flow region. The appropriate boundary conditions on the external surfaces are again the no-slip and no-penetration conditions. Like the previous discussion, it can be proved that no-penetration implies no-slip if vortex sheets are introduced on

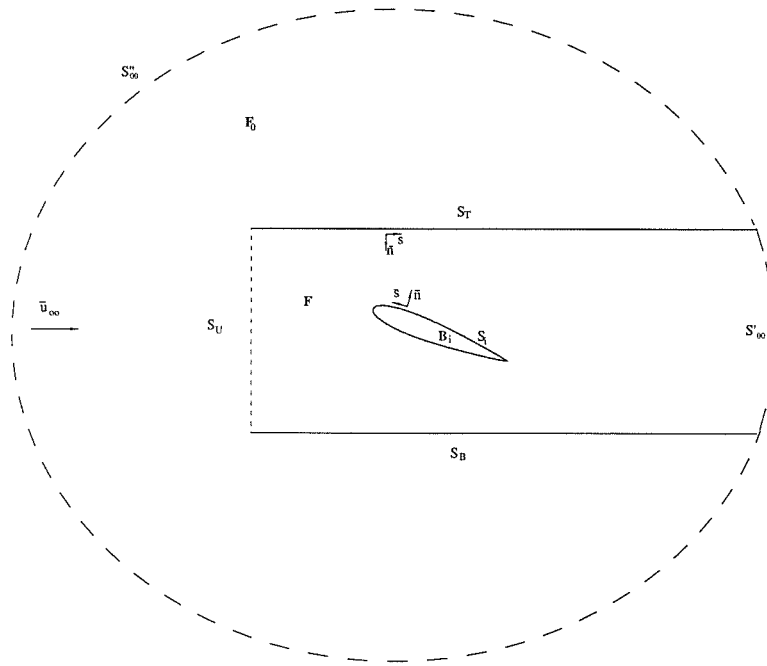


Figure 2.2: Flow regions

the boundary, and therefore only the former need be implemented. The technique is to consider the assumed irrotational velocity field outside the bounded flow region.

As shown in figure 2.2, S_T and S_B are the tunnel walls. Both are parallel to the velocity of flow at infinity, $\bar{\mathbf{u}}_\infty$. These surfaces are connected upstream by surface S_U , which is perpendicular to $\bar{\mathbf{u}}_\infty$. S_T and S_B divide the boundary at infinity S_∞ into two, S''_∞ and S'_∞ . $S_0 = S''_\infty + S_T + S_U + S_B$ is a closed contour. So is $S = S'_\infty + S_T + S_U + S_B$. The field enclosed by S_0 is denoted F_0 .

$\bar{\mathbf{u}}_0$ is the velocity in the field F_0 . It can be assumed to be solenoidal and irrotational, that is, $\nabla \cdot \bar{\mathbf{u}}_0 = 0$ and $\nabla \times \bar{\mathbf{u}}_0 = 0$. The corresponding stream function ψ_0 is the solution of Laplace's equation

$$\nabla^2 \psi_0 = 0 \quad (2.16)$$

subject to boundary conditions. On boundary S_U , which is far away from the airfoil, it is relatively safe to assume that there is a uniform velocity $\bar{\mathbf{u}}_0 = \bar{\mathbf{u}}_\infty$, corresponding

to $-\vec{\mathbf{k}} \times \nabla \psi_0 = \vec{\mathbf{u}}_\infty$. The other boundary conditions are

$$\begin{aligned} -\vec{\mathbf{k}} \times \nabla \psi_0 &= \vec{\mathbf{u}}_\infty \quad \text{at } S_\infty'' \\ \vec{\mathbf{s}} \cdot \nabla \psi_0 &= 0 \quad \text{on } S_T \text{ and } S_B \end{aligned}$$

where only the normal components of velocity on S_T and S_B are specified.

It is easily shown that the stream function associated with the uniform velocity field $\vec{\mathbf{u}}_0 = \vec{\mathbf{u}}_\infty$ is a solution. Using a similar argument to that given in the previous section, it can be further deduced that this solution is a unique one, up to an arbitrary constant. The existence of uniform velocity field $\vec{\mathbf{u}}_0$ means that there is a tangential velocity component equal to u_∞ on both S_T and S_B . Therefore the no-slip condition on the side of the boundaries in region F , denoted S_T^- and S_B^- , can only be satisfied if the tangential velocities in the two regions F_0 and F are discontinuous across the borders S_B and S_T . This can be achieved by the introduction of vortex sheets of constant strength, $\gamma = -u_\infty$ on S_T and $\gamma = u_\infty$ on S_B , so that zero tangential velocity on S_T^- and S_B^- can be guaranteed. This proves that, with the additional vortex sheets, the no-penetration condition will imply the no-slip condition as far as the real flow in F is concerned.

By applying Green's Theorem to region F_0 , the stream function ψ_0 satisfies the following integral

$$\oint_{S_0} (\varphi \nabla \psi_0 - \psi_0 \nabla \varphi) \cdot \vec{\mathbf{n}} dS_i = 0 \quad (2.17)$$

where $\varphi = \frac{1}{2\pi} \ln |\vec{\mathbf{r}} - \vec{\mathbf{r}}_p|$, and $\vec{\mathbf{r}}_p \notin F_0$. $\nabla^2 \varphi = 0$ when $\vec{\mathbf{r}} \neq \vec{\mathbf{r}}_p$

2.4 Velocity field in terms of the vorticity

Knowledge of the velocity field is of particular importance for both the flow transportation and the implementation of the boundary conditions. Flow particles progress in accordance with their velocity, and the boundary conditions (e.g. no-slip, no-penetration) can be expressed explicitly in terms of the velocity. Furthermore, in

inviscid flow, vorticity is a conserved property of the flow particles, and is transported with the particles.

The vorticity field is obtained from the curl of the velocity field. The inverse solution, i.e. expressing the velocity in terms of the vorticity, is accomplished by the Biot-Savart law, and is straightforward for flow in an infinite homogeneous domain. The presence of flow constraints and/or interior boundaries, however, presents an added difficulty. Vezza¹⁶⁰ has derived the velocity expression for the two dimensional infinite flow around moving bodies using Green's Theorem. A similar approach is employed to formulate the velocity field for flow with exterior limits similar to wind tunnel wall constraints.

Referring to figure 2.2, the whole two dimensional space is considered to consist of three regions; B_i , F_0 , as described in the previous two sections, and F , which is the area enclosed by the contour S , but excluding that enclosed by S_i . The vorticity in both F_0 and B_i is known to be zero and $2\Omega_i$ respectively, while vorticity in F is the subject of solution.

The velocity field \vec{u} in flow region F is solenoidal due to the continuity equation $\nabla \cdot \vec{u} = 0$. This indicates the existence of a vector potential $\vec{\Psi}$, which satisfies $\vec{u} = \nabla \times \vec{\Psi}$. In two dimensional flow the vector potential is reduced to $\vec{k}\psi$, in which ψ , the stream function, is related to vorticity through the equation

$$\nabla^2 \psi = -\omega \quad (2.18)$$

This combines with the vorticity transport equation (2.3) in the vorticity/stream function form of the governing equations.

There is a unique solution, up to an arbitrary constant, for stream function ψ in the above Poisson equation provided that the following boundary conditions are satisfied:

$$\begin{aligned} -\vec{k} \times \nabla \psi &= \vec{u}_\infty \quad \text{on } S'_\infty \\ -\vec{k} \times \nabla \psi &= \vec{u}_\infty \quad \text{on } S_U \quad \text{and} \end{aligned}$$

$$\begin{aligned}
&\text{either } \vec{\mathbf{n}} \cdot \nabla \psi = -\vec{\mathbf{s}} \cdot [\vec{\mathbf{u}}_{c_i} + \Omega_i \vec{\mathbf{k}} \times (\vec{\mathbf{r}} - \vec{\mathbf{r}}_{c_i})] \text{ on } S_i \\
&\quad \vec{\mathbf{n}} \cdot \nabla \psi = 0 \text{ on } S_T \text{ and } S_B \\
&\text{or } \vec{\mathbf{s}} \cdot \nabla \psi = \vec{\mathbf{n}} \cdot [\vec{\mathbf{u}}_{c_i} + \Omega_i \vec{\mathbf{k}} \times (\vec{\mathbf{r}} - \vec{\mathbf{r}}_{c_i})] \text{ on } S_i \\
&\quad \vec{\mathbf{s}} \cdot \nabla \psi = 0 \text{ on } S_T \text{ and } S_B
\end{aligned}$$

These conditions encompass the no-slip and no-penetration conditions on the physical borders of regions B_i and F_0 and also the far field requirements. Uniform inflow has been assumed on the surface S_U .

It is convenient to combine the boundary conditions for regions F_0 , F and B_i on common boundary surfaces. This results in the following expressions

$$\begin{aligned}
&-\vec{\mathbf{k}} \times \nabla \psi = \vec{\mathbf{u}}_\infty \text{ on } S'_\infty \\
&-\vec{\mathbf{k}} \times \nabla (\psi - \psi_0) = 0 \text{ on } S_U \text{ and} \\
&\text{either } \vec{\mathbf{n}} \cdot \nabla (\psi - \psi_i) = 0 \text{ on } S_i \\
&\quad \vec{\mathbf{n}} \cdot \nabla (\psi - \psi_0) = u_\infty \text{ on } S_T \\
&\quad \vec{\mathbf{n}} \cdot \nabla (\psi - \psi_0) = -u_\infty \text{ on } S_B \\
&\text{or } \vec{\mathbf{s}} \cdot \nabla (\psi - \psi_i) = 0 \text{ on } S_i \\
&\quad \vec{\mathbf{s}} \cdot \nabla (\psi - \psi_0) = 0 \text{ on } S_T \text{ and } S_B \tag{2.19}
\end{aligned}$$

The above conditions state that the velocity is continuous between the regions F and B_i and between F and F_0 except on S_T and S_B , where there is a jump in tangential velocity of u_∞ . However, only the no-penetration conditions on physical boundaries and the condition at infinity are required to be implemented explicitly because the other conditions, including no-slip, follow from previous arguments.

The solution of the Poisson equation subject to the above boundary conditions can be achieved by using Green's Theorem, which states

$$\oint_{S+S_i} (\varphi \nabla \psi - \psi \nabla \varphi) \cdot \vec{\mathbf{n}} dS = - \iint_F (\varphi \nabla^2 \psi - \psi \nabla^2 \varphi) dF \tag{2.20}$$

Choosing the fundamental solution to be

$$\varphi = \frac{1}{2\pi} \ln |\vec{\mathbf{r}} - \vec{\mathbf{r}}_p| \tag{2.21}$$

in which p is a point in flow F , it can be shown¹⁶¹ that

$$\nabla^2 \varphi = \delta(|\vec{r} - \vec{r}_p|) \quad (2.22)$$

By substituting φ into Green's theorem, the stream function at point p is obtained

$$\psi_p = - \iint_F \varphi \omega dF + \oint_{S+S_i} (\varphi \nabla \psi - \psi \nabla \varphi) \cdot \vec{n} dS \quad (2.23)$$

The results by similar use of Green's theorem on region B_i , and F_0 have been obtained in the previous sections. Since p is a point in region F , it cannot be a point in regions B_i and F_i .

Combining the three equations, 2.13, 2.17 and 2.23, obtained from these regions, results in

$$\begin{aligned} \psi_p &= - \iint_F \varphi \omega dF - \iint_{B_i} 2\Omega_i \varphi dB_i \\ &+ \int_{S_T+S_U+S_B} [\varphi \nabla (\psi - \psi_0) - (\psi - \psi_0) \nabla \varphi] \cdot \vec{n} dS \\ &+ \int_{S_i} [\varphi \nabla (\psi - \psi_i) - (\psi - \psi_i) \nabla \varphi] \cdot \vec{n} dS_i + \int_{S_\infty} [\varphi \nabla \psi - \psi \nabla \varphi] \cdot \vec{n} dS_\infty \end{aligned}$$

Implementation of the "relative" boundary conditions (2.19) gives,

$$\psi_p = - \iint_F \varphi \omega dF - \iint_{B_i} 2\Omega_i \varphi dB_i - \int_{S_T} \varphi \nabla \psi_0 \cdot \vec{n} dS - \int_{S_B} \varphi \nabla \psi_0 \cdot \vec{n} dS + \psi_\infty \quad (2.24)$$

where ψ_∞ represents the integral at infinity and satisfies the boundary condition $\nabla \psi_\infty \times \vec{k} = \vec{u}_\infty$

The velocity field corresponding to the above stream function is

$$\begin{aligned} \vec{u}_p &= \iint_F \frac{\omega(\vec{r} - \vec{r}_p) \times \vec{k}}{2\pi |\vec{r} - \vec{r}_p|^2} dF + \iint_{B_i} \frac{2\Omega_i(\vec{r} - \vec{r}_p) \times \vec{k}}{2\pi |\vec{r} - \vec{r}_p|^2} dB_i + \int_{S_T} \frac{(\vec{r} - \vec{r}_p) \times \vec{k}}{2\pi |\vec{r} - \vec{r}_p|^2} \nabla \psi_0 \cdot \vec{n} dS \\ &+ \int_{S_B} \frac{(\vec{r} - \vec{r}_p) \times \vec{k}}{2\pi |\vec{r} - \vec{r}_p|^2} \varphi \nabla \psi_0 \cdot \vec{n} dS + \vec{u}_\infty \end{aligned} \quad (2.25)$$

The velocity of a flow particle in flow F consists of four contributions. Those from the freestream velocity \vec{u}_∞ and the vorticity field ω are standard. The others, however, are additional contributions due to the existence of the moving boundary and the external constraints.

The second contribution to $\bar{\mathbf{u}}_p$ is identical to the induced velocity by a velocity field with constant vorticity $2\Omega_i$ occupying the solid region B_i . This integral can be transformed into a surface integral along the boundary S_i , which enables a simplified evaluation of the moving boundary contribution. The third and fourth contributions, due to the exterior constraints, are effectively equivalent to the influence of vortex sheets along S_T and S_B .

Mathematically, the flow with exterior constraints and moving rigid body is the same as an unlimited flow occupying the whole space with vortex sheets located along the position of the external boundaries, and an embedded flow of uniform vorticity equal to twice the rotational velocity distributed over the area enclosed by the moving boundary.

Further discussions are needed to clarify the above results.

The involvement of the vortex sheets or vorticity inside moving bodies comes from mathematical equivalence to the boundary requirements only. This does not mean that there is any physical reality to the flows inside the body or beyond the exterior constraints.

Note that there are inconsistencies in the boundary velocity requirements at the points where the connected segments of S join. These can be resolved by assigning the points to one or other of the segments, making S a segment continuous surface upon which surface integrals exist. This treatment does not affect the result of the integrals, whether the boundary conditions are applied in the “absolute” or “relative” form.

Theoretically, segments S_T and S_B should be extended upstream to infinity and S_U should become part of S_∞ . The final formula for stream function and velocity remain the same, however, as the semi-infinite surface model, described above, can be reduced from the infinite model if S_U is far enough away from any solid body and the wall flow neighbouring the upstream boundary is not separated. The semi-infinite model represents the vorticity in the flow F beyond the truncation point with a constant vortex sheet which has the same strength but opposite sign as the vortex

sheet implemented on the rest of the exterior boundary. Since these cancel each other in this region the influence is zero. This representation is reasonable when the truncation is far from the influence of any solid bodies.

The same argument applies to the external surfaces downstream, although the flow situation is slightly different. The vorticity released from the bodies is transported downstream and the interaction with the vorticity associated with the constraint segments is relatively greater than occurs upstream. Hence the truncation points are required to be farther away from any solid bodies so that the constant vortex sheet representation of the constraints will have little erroneous impact on the flow near the bodies.

By choosing two truncation points on each segment S_T and S_B , we have reduced an infinite vortex sheet or semi-infinite one into a finite one which avoids the evaluation of an infinite integral for constant vortex sheets. The boundary condition at infinity is also satisfied as the constraints are not extended to infinity. Despite these two truncations, the above formula for stream function and velocity remain the same if we regard S_T and S_B as finite.

The assumption of uniform velocity distribution at inlet and outlet will make some difference to flow nearby, but the influence on flow near bodies is limited if the previous conditions are fulfilled. As the bodies are of main interest, such an assumption is acceptable.

The “relative” boundary conditions, which illustrate the kinematic link between the different regions, are used to derive the velocity field in F . The velocity fields in F_0 and B_i can be expressed in a similar way by specifying point p either in F_0 or in B_i , although they are known explicitly for any given \vec{u}_∞ and Ω_i . For any p in B_i , the expression is identical to the one for F .

In the absence of the external constraints, the stream function and velocity equations are reduced to

$$\psi_p = - \iint_F \varphi \omega dF - \iint_{B_i} 2\Omega_i \varphi dB_i + \psi_\infty \quad (2.26)$$

$$\vec{u}_p = \iint_F \frac{\omega(\vec{r} - \vec{r}_p) \times \vec{k}}{2\pi |\vec{r} - \vec{r}_p|^2} dF + \iint_{B_i} \frac{2\Omega_i(\vec{r} - \vec{r}_p) \times \vec{k}}{2\pi |\vec{r} - \vec{r}_p|^2} dB_i + \vec{u}_\infty \quad (2.27)$$

respectively, which are the same as those derived by Vezza.¹⁶⁰

2.5 Conservation of circulation

The circulation along a closed curve is defined as the line integral of velocity

$$\Gamma = \oint \vec{u} \cdot d\vec{l} \quad (2.28)$$

Stokes' theorem states

$$\oint_S \vec{u} \cdot d\vec{l} = \iint_A (\nabla \times \vec{u}) \cdot \vec{k} dA \quad (2.29)$$

where A is the area enclosed by the contour S and \vec{k} is the normal of dA . For two dimensional flow where $\vec{\omega} = \vec{k}\omega$, Stokes' theorem becomes

$$\oint_S \vec{u} \cdot d\vec{l} = \iint_A \omega dA \quad (2.30)$$

The circulation along a closed curve at infinity is zero, that is

$$\Gamma_\infty = \oint_{S_\infty} \vec{u} \cdot d\vec{l} = \int_{S'_\infty} \vec{u} \cdot d\vec{l} + \int_{S''_\infty} \vec{u} \cdot d\vec{l} = 0 \quad (2.31)$$

As discussed earlier, the entire space consists of three regions, flow F with vorticity ω , externally extended irrotational region F_0 , and internal region B_i with vorticity $2\Omega_i$. Enclosing these regions are the boundaries S and S_i , S_0 , and S_i respectively, around which the circulations are

$$\begin{aligned} \Gamma &= \oint_{S+S_i} \vec{u} \cdot d\vec{l} = \iint_F \omega dF \\ \Gamma_0 &= \oint_{S_0} \vec{u} \cdot d\vec{l} = 0 \\ \Gamma_i &= \oint_{S_i} \vec{u} \cdot d\vec{l} = 2\Omega_i A_i \end{aligned}$$

After implementing the velocity boundary conditions, the result is

$$\iint_F \omega dF + 2\Omega_i A_i + \int_{S_T} \vec{u}_0 \cdot d\vec{l} + \int_{S_B} \vec{u}_0 \cdot d\vec{l} = 0 \quad (2.32)$$

where \vec{u}_0 is \vec{u}_∞ as discussed previously. The equation states that the circulation of all the vorticity, including that inside the bodies and the vortex sheets used to represent the external constraints, is zero. The equation holds whether the flow is inviscid or viscous. Note that Kelvin's theorem, which states that the rate of change of circulation is zero around a finite closed material curve, is valid only in inviscid flow. In the case of viscous flow there is diffusion of vorticity through the contour.

In the absence of the external constraints, the conservation equation becomes

$$\iint_F \omega dF + 2\Omega_i A_i = 0 \quad (2.33)$$

If there are multiple bodies immersed in the flow, the second term should be summed for all bodies, while the first term represents the circulation of all the flow vorticity in F regardless of origin. Some methods, by constructing a material contour around each body, employ a similar equation for each body. In doing so, this implies the flow is inviscid. For viscous flow, there is an equation governing the rate of change of circulation around each body. The equation is similar to the inviscid one, however the physical meaning is quite different. Details will be given in later sections.

2.6 *Boundary conditions*

Given a vorticity field, the velocity field is determined by solving the Poisson equations derived previously. Such a relationship indicates that the vorticity field cannot be arbitrary as the surface velocities must satisfy the boundary conditions. It is in fact these conditions which are used to completely determine the vorticity field.

It has been shown¹⁶² that the vorticity originates from the boundary and that it is convected and diffused in accordance with the vorticity transport equation. For any instant, vorticity in the flow can be categorised into that pre-existing and that newly created. The latter is defined only in the thin layer around the boundary. From this

fact, the flow region F is divided into F_B , the thin layer around the boundary, and F_W , the rest of F . The vorticity in F_W evolves in accordance with the vorticity transport equation and the exchange between F_W and F_B . The strength of vorticity in F_B is unknown but can be calculated by implementing both the boundary conditions and additional conditions on the circulation.

Referring to the previous sections, the boundary S consists of the boundary at infinity S'_∞ , physical boundaries, S_i , S_T and S_B , and imaginary boundary S_U for the case in which S_T and S_B are extended downstream to infinity. The expressions for velocity employ the relative boundary requirements rather than the absolute velocity values. The absolute value of velocity on the inner boundary is given in section 2.2 while, on the external constraints, the velocity on the physical surfaces, S_T and S_B , is zero. The velocity on imaginary surface S_U is that of the free stream. Both the inner and external requirements are incorporated into the equations governing the vorticity field.

The boundary conditions can be implemented either in Neumann form or in a manner similar to the Dirichelet form. The requirements for the former are

$$\begin{aligned}
\iint_{F_B} \frac{\omega(\vec{\mathbf{r}} - \vec{\mathbf{r}}_p) \times \vec{\mathbf{k}}}{2\pi |\vec{\mathbf{r}} - \vec{\mathbf{r}}_p|^2} dF &= - \iint_{F_W} \frac{\omega(\vec{\mathbf{r}} - \vec{\mathbf{r}}_p) \times \vec{\mathbf{k}}}{2\pi |\vec{\mathbf{r}} - \vec{\mathbf{r}}_p|^2} dF - \iint_{B_i} \frac{2\Omega_i(\vec{\mathbf{r}} - \vec{\mathbf{r}}_p) \times \vec{\mathbf{k}}}{2\pi |\vec{\mathbf{r}} - \vec{\mathbf{r}}_p|^2} dB_i \\
&- \int_{S_T} \frac{(\vec{\mathbf{r}} - \vec{\mathbf{r}}_p) \times \vec{\mathbf{k}}}{2\pi |\vec{\mathbf{r}} - \vec{\mathbf{r}}_p|^2} \nabla \psi_0 \cdot \vec{\mathbf{n}} dS - \int_{S_B} \frac{(\vec{\mathbf{r}} - \vec{\mathbf{r}}_p) \times \vec{\mathbf{k}}}{2\pi |\vec{\mathbf{r}} - \vec{\mathbf{r}}_p|^2} \varphi \nabla \psi_0 \cdot \vec{\mathbf{n}} dS \\
&- \vec{\mathbf{u}}_\infty + \vec{\mathbf{u}}_{c_i} + \Omega_i \vec{\mathbf{k}} \times (\vec{\mathbf{r}} - \vec{\mathbf{r}}_c) \quad \text{on } S_i
\end{aligned} \tag{2.34}$$

$$\begin{aligned}
\iint_{F_B} \frac{\omega(\vec{\mathbf{r}} - \vec{\mathbf{r}}_p) \times \vec{\mathbf{k}}}{2\pi |\vec{\mathbf{r}} - \vec{\mathbf{r}}_p|^2} dF &= - \iint_{F_W} \frac{\omega(\vec{\mathbf{r}} - \vec{\mathbf{r}}_p) \times \vec{\mathbf{k}}}{2\pi |\vec{\mathbf{r}} - \vec{\mathbf{r}}_p|^2} dF - \iint_{B_i} \frac{2\Omega_i(\vec{\mathbf{r}} - \vec{\mathbf{r}}_p) \times \vec{\mathbf{k}}}{2\pi |\vec{\mathbf{r}} - \vec{\mathbf{r}}_p|^2} dB_i \\
&- \int_{S_T} \frac{(\vec{\mathbf{r}} - \vec{\mathbf{r}}_p) \times \vec{\mathbf{k}}}{2\pi |\vec{\mathbf{r}} - \vec{\mathbf{r}}_p|^2} \nabla \psi_0 \cdot \vec{\mathbf{n}} dS \\
&- \int_{S_B} \frac{(\vec{\mathbf{r}} - \vec{\mathbf{r}}_p) \times \vec{\mathbf{k}}}{2\pi |\vec{\mathbf{r}} - \vec{\mathbf{r}}_p|^2} \varphi \nabla \psi_0 \cdot \vec{\mathbf{n}} dS - \vec{\mathbf{u}}_\infty \\
&\quad \text{on } S_T \text{ and } S_B
\end{aligned} \tag{2.35}$$

$$\begin{aligned}
\iint_{F_B} \frac{\omega(\vec{\mathbf{r}} - \vec{\mathbf{r}}_p) \times \vec{\mathbf{k}}}{2\pi |\vec{\mathbf{r}} - \vec{\mathbf{r}}_p|^2} dF &= - \iint_{F_W} \frac{\omega(\vec{\mathbf{r}} - \vec{\mathbf{r}}_p) \times \vec{\mathbf{k}}}{2\pi |\vec{\mathbf{r}} - \vec{\mathbf{r}}_p|^2} dF - \iint_{B_i} \frac{2\Omega_i(\vec{\mathbf{r}} - \vec{\mathbf{r}}_p) \times \vec{\mathbf{k}}}{2\pi |\vec{\mathbf{r}} - \vec{\mathbf{r}}_p|^2} dB_i \\
&- \int_{S_T} \frac{(\vec{\mathbf{r}} - \vec{\mathbf{r}}_p) \times \vec{\mathbf{k}}}{2\pi |\vec{\mathbf{r}} - \vec{\mathbf{r}}_p|^2} \nabla \psi_0 \cdot \vec{\mathbf{n}} dS \\
&- \int_{S_B} \frac{(\vec{\mathbf{r}} - \vec{\mathbf{r}}_p) \times \vec{\mathbf{k}}}{2\pi |\vec{\mathbf{r}} - \vec{\mathbf{r}}_p|^2} \varphi \nabla \psi_0 \cdot \vec{\mathbf{n}} dS \\
&\text{on } S_U \text{ and on } S'_\infty
\end{aligned} \tag{2.36}$$

In the absence of the external constraints, the equations are reduced to

$$\begin{aligned}
\iint_{F_B} \frac{\omega(\vec{\mathbf{r}} - \vec{\mathbf{r}}_p) \times \vec{\mathbf{k}}}{2\pi |\vec{\mathbf{r}} - \vec{\mathbf{r}}_p|^2} dF &= - \iint_{F_W} \frac{\omega(\vec{\mathbf{r}} - \vec{\mathbf{r}}_p) \times \vec{\mathbf{k}}}{2\pi |\vec{\mathbf{r}} - \vec{\mathbf{r}}_p|^2} dF - \iint_{B_i} \frac{2\Omega_i(\vec{\mathbf{r}} - \vec{\mathbf{r}}_p) \times \vec{\mathbf{k}}}{2\pi |\vec{\mathbf{r}} - \vec{\mathbf{r}}_p|^2} dB_i \\
&- \vec{\mathbf{u}}_\infty + \vec{\mathbf{u}}_{c_i} + \Omega_i \vec{\mathbf{k}} \times (\vec{\mathbf{r}} - \vec{\mathbf{r}}_c) \quad \text{on } S_i
\end{aligned} \tag{2.37}$$

In the alternative, and considered superior, form the boundary conditions are expressed in terms of stream function, and the requirements become

$$\begin{aligned}
\frac{\partial(\psi - \psi_i)}{\partial s} &= 0, \quad \frac{\partial(\psi - \psi_i)}{\partial n} = 0 \quad \text{on } S_i \\
\frac{\partial\psi}{\partial s} &= 0, \quad \frac{\partial\psi}{\partial n} = 0 \quad \text{on } S_T, \text{ and } S_B
\end{aligned} \tag{2.38}$$

where $\frac{\partial\psi_i}{\partial s} = \vec{\mathbf{s}} \cdot \nabla \psi_i$ has been given previously in equations 2.12. $\frac{\partial(\psi - \psi_i)}{\partial s} = 0$ indicates that $\psi - \psi_i$ remains constant along S_i . That is, for any a, b on S_i , $(\psi_a - \psi_{i_a}) - (\psi_b - \psi_{i_b}) = 0$, or,

$$\begin{aligned}
\iint_{F_B} (\varphi_a - \varphi_b) \omega dF &= - \iint_{F_W} (\varphi_a - \varphi_b) \omega dF - \iint_{B_i} 2\Omega_i(\varphi_a - \varphi_b) dB_i \\
&- \int_{S_T} (\varphi_a - \varphi_b) \nabla \psi_0 \cdot \vec{\mathbf{n}} dS - \int_{S_B} (\varphi_a - \varphi_b) \nabla \psi_0 \cdot \vec{\mathbf{n}} dS \\
&- (\vec{\mathbf{r}}_a - \vec{\mathbf{r}}_b) \cdot (\vec{\mathbf{k}} \times \vec{\mathbf{u}}_{c_i}) + \frac{1}{2} \Omega_i (|\vec{\mathbf{r}}_a - \vec{\mathbf{r}}_c|^2 - |\vec{\mathbf{r}}_b - \vec{\mathbf{r}}_c|^2) \\
&+ (\vec{\mathbf{r}}_a - \vec{\mathbf{r}}_b) \cdot (\vec{\mathbf{k}} \times \vec{\mathbf{u}}_\infty) \quad \text{for any } a, b \text{ on } S_i
\end{aligned} \tag{2.39}$$

Similarly, for any a, b on S_T or S_B , $\frac{\partial\psi}{\partial s} = 0$ implies that ψ is a constant along either surface, or

$$\iint_{F_B} (\varphi_a - \varphi_b) \omega dF = - \iint_{F_W} (\varphi_a - \varphi_b) \omega dF - \iint_{B_i} 2\Omega_i(\varphi_a - \varphi_b) dB_i$$

$$\begin{aligned}
& - \int_{S_T} (\varphi_a - \varphi_b) \nabla \psi_0 \cdot \vec{\mathbf{n}} dS - \int_{S_B} (\varphi_a - \varphi_b) \nabla \psi_0 \cdot \vec{\mathbf{n}} dS \\
& + (\vec{\mathbf{r}}_a - \vec{\mathbf{r}}_b) \cdot (\vec{\mathbf{k}} \times \vec{\mathbf{u}}_\infty) \quad \text{for any } a \text{ } b \text{ on } S_T \text{ or on } S_B \quad (2.40)
\end{aligned}$$

Since a uniform velocity distribution is assumed on S_U , the difference in stream function between S_T and S_B should be $(\vec{\mathbf{u}}_\infty \cdot \vec{\mathbf{n}} |S_U|)$, in which $\vec{\mathbf{n}}$ is the unit normal and $|S_U|$ the dimension of S_U respectively. Implementation results in

$$\begin{aligned}
\iint_{F_B} (\varphi_a - \varphi_b) \omega dF &= - \iint_{F_W} (\varphi_a - \varphi_b) \omega dF - \iint_{B_i} 2\Omega_i (\varphi_a - \varphi_b) dB_i \\
& - \int_{S_T} (\varphi_a - \varphi_b) \nabla \psi_0 \cdot \vec{\mathbf{n}} dS - \int_{S_B} (\varphi_a - \varphi_b) \nabla \psi_0 \cdot \vec{\mathbf{n}} dS \\
& - u_\infty |S_U| \\
& \text{for any } a \text{ on } S_T \text{ and } b \text{ on } S_B \quad (2.41)
\end{aligned}$$

For unbounded flows, the boundary conditions on S_i become

$$\begin{aligned}
\iint_{F_B} (\varphi_a - \varphi_b) \omega dF &= - \iint_{F_W} (\varphi_a - \varphi_b) \omega dF - \iint_{B_i} 2\Omega_i (\varphi_a - \varphi_b) dB_i \\
& - (\vec{\mathbf{r}}_a - \vec{\mathbf{r}}_b) \cdot (\vec{\mathbf{k}} \times \vec{\mathbf{u}}_{c_i}) + \frac{1}{2} \Omega_i (|\vec{\mathbf{r}}_a - \vec{\mathbf{r}}_c|^2 - |\vec{\mathbf{r}}_b - \vec{\mathbf{r}}_c|^2) \\
& + (\vec{\mathbf{r}}_a - \vec{\mathbf{r}}_b) \cdot (\vec{\mathbf{k}} \times \vec{\mathbf{u}}_\infty) \quad \text{on } S_i \quad (2.42)
\end{aligned}$$

The Dirichelet form of the boundary conditions given above only accounts for the normal component of velocity on the boundary, while the Neumann conditions include the tangential component. However, both forms are compatible. This follows from the flow conditions on the boundaries between F and F_0 and F and B_i as discussed previously, from which the implementation of no-penetration on the boundaries of F implies no-slip, that is satisfaction of the tangential conditions.

The Dirichelet conditions and the conclusion that normal boundary conditions imply tangential conditions are both based on the definitions of normal and tangential. However there may be some points, such as an aerofoil trailing edge, where the definitions are ambiguous, although well defined on either side of the point. At any smooth surface points near a sharp edge, continuous normal velocity is required. Fortunately the velocity field does not allow for jumps in velocity unless there is

a singularity, which does not exist. Therefore, the “normal” velocity components should be continuous at a sharp edge irrespective of the side on which the “normal” is defined. This requires the velocity to be continuous in any direction at these points in order to satisfy this condition.

It is apparent therefore that no special treatment is required for sharp edges if there are only a finite number of such points on a contour and if the above Dirichelet conditions are applied to the contour continuously. Continuity of the velocity component in either normal direction of a sharp edge will guarantee continuity in the other normal direction because of the satisfaction of the Dirichelet conditions at nearby smooth surface points.

2.7 Evaluation of the force and moment

The force and moment can be calculated by integrating the pressure and shear stress along the body surface. From the Navier-Stokes equation one can obtain the pressure gradient, which can then be integrated along the surface to produce the pressure distribution. N-S equation (2.2) from section 2.1 can be rewritten

$$\frac{D\vec{u}}{Dt} = -\frac{1}{\rho} \nabla p + \nu \nabla^2 \vec{u}$$

Applying this equation to the interior boundary, where $\frac{D\vec{u}}{Dt}$ (2.14) is known, the pressure gradient is obtained by considering the component equation in the direction of the unit tangential vector \vec{s}

$$\frac{1}{\rho} \frac{\partial p}{\partial s} = -\vec{s} \cdot \frac{D\vec{u}_{ci}}{Dt} - \frac{D\vec{\Omega}_i}{Dt} \cdot \vec{n} \cdot (\vec{r} - \vec{r}_{ci}) + \Omega_i^2 \vec{s} \cdot (\vec{r} - \vec{r}_{ci}) + \nu \frac{\partial \omega}{\partial n} \quad (2.43)$$

The term, $\vec{s} \cdot \nu \nabla^2 \vec{u} = -\nu \vec{n} \cdot \nabla \omega = -\nu \frac{\partial \omega}{\partial n}$, is the *rate of vorticity creation* on the boundary. Spalart¹²⁹ proved this for stationary bodies. For moving bodies the time rate of change of vorticity is defined as a material derivative $D\omega/Dt$ rather than the temporal derivative $\partial\omega/\partial t$, as the velocity of the flow particle on the boundary is that of the body. Rewriting the vorticity transport equation (2.3) as

$$\frac{D\omega}{Dt} = -\nabla \cdot (-\nu \nabla \omega) \quad (2.44)$$

$-\nu \nabla \omega$ is the rate of increase of vorticity, which at the boundary is $-\nu(\partial\omega/\partial n)$.

Pressure, which can be obtained by integrating the above pressure gradient along the surface, should be single-valued in the field, which requires a zero integral of the pressure gradient along a closed contour. Integrating the above pressure gradient along the closed boundary results in

$$-2\frac{D\Omega_i}{Dt}A_i + \oint_{S_i} \nu \frac{\partial\omega}{\partial n} dS_i = 0 \quad (2.45)$$

as integral $\oint_{S_i} -\vec{s} \cdot (D\vec{u}_{c_i}/Dt) dS_i$ and $\oint_{S_i} \Omega_i^2 \vec{s} \cdot (\vec{r} - \vec{r}_c) dS_i$ are zero. The two terms represent the total rate of change of both circulation inside the body and vorticity entering the flow respectively. The equation shows that the net increase in vorticity created at the body surface is produced at the expense of vorticity inside the body. This equation does not depend on whether vorticity diffusion occurs in the outer flow. Unlike Kelvin's theorem, which is only valid for inviscid flow, the above relationship holds for viscous flow, as the single-valued pressure requirement is a physical property of such flows.

The equation can also be interpreted as a condition for each body whereby the sum of the total interior vorticity and that created on the surface remains constant at any instant in time. Practically it is easier to implement this version rather than the zero rate of change. The constant, $C_i = 2\Omega_i(0)A_i + \Gamma_i(0)$, is the initial value of the total circulation with respect to each body. For impulse started flow, where the vorticity is not initially dispersed in the flow, the velocity field outwith the body is undisturbed and the line integral of velocity around a contour big enough to enclose the body should be zero, that is, $C_i = 0$. This means that there is non-zero initial circulation, $\Gamma_i(0)$, created by the body if there exists a non-zero initial angular velocity, $\Omega_i(0)$. Such circulation is concentrated on the boundary.

The approach described above for the pressure distribution has the advantage of guaranteeing a single valued pressure field, although this value can only be predicted up to a constant, rather than an absolute value. However, in many cases, the flow region in contact with the upstream part of the body can be assumed irrotational

and the stagnation point can be located approximately. Fortunately, the accuracy of the stagnation point does not affect the integrated body forces, that is the force and moment, parameters which are of most interest for pitching aerofoils and many other cases. If the pressure outwith the boundary is required the boundary values can be used in the solution of the Poisson's equation $(1/\rho) \nabla^2 p = - \nabla \cdot ((\vec{u} \cdot \nabla) \vec{u})$

2.8 Conclusion

Incompressible two dimensional flow is governed by the continuity and N-S equations which, as has been shown, can be replaced by the Poisson and vorticity transport equations. Extension of the Biot-Savart law, which is valid for an unbounded domain, has provided the relationship between velocity and vorticity for flows bounded by moving bodies and exterior constraints. The relationship contains additional terms which have been shown to be mathematically equivalent to the influences of a constant vorticity field occupying the body area, and a constant vortex sheet of strength u_∞ on the exterior physical boundary. Such equivalence simplifies the evaluation of velocity, as both vorticity distributions are known in advance of the calculation.

Only the normal velocity component of the boundary conditions is required to be implemented in determining the vorticity field, as satisfaction of the tangential condition is subsequently implied. This is proved in regions B_i and F_0 where the vorticity field is known, and the "continuity" of velocity across the boundaries with F extends this conclusion to region F .

The method chosen to implement the normal boundary condition employs the stream function difference along the boundary. The velocity fields in B_i and F_0 are known, as are the corresponding stream functions. Hence this implementation only requires the value of stream function rather than its derivative.

The requirement for a single-valued pressure field provides an additional equation for each body, ensuring the constancy of the total vorticity contained within and emanating from the body. This relationship, together with boundary conditions,

form a set of equations which are used to determine the rate at which vorticity enters the flow at any instant in time.

Chapter 3

NUMERICAL IMPLEMENTATION

In the previous chapter it was shown how the continuous form of the equations, governing the exact requirements for the vorticity field, could be obtained by implementing the boundary conditions. However, for most cases it is impossible to solve such integral equations theoretically. One way of getting an approximate solution is to discretize the vorticity field with vortices distributed over the spatial domain. In this way one can obtain a solution numerically, although it has to be ensured that the discretization truly represents physical reality.

In this chapter is presented a numerical scheme, particularly applicable to a streamlined body with a sharp edge like an aerofoil. The scheme is based on the understanding of the vorticity behaviour and special features of flows around such bodies. The chapter begins by discussing some aspects relating to vorticity interaction with a body. This is followed by a detailed description of the model, including mathematical developments and considerations of accuracy.

3.1 Vorticity layer

Since vorticity is the curl of the velocity vector, vorticity represents the spatial change of the velocity field at any instant in time. Hence an insight into the vorticity distribution and its evolution can be obtained by looking at the velocity field and its temporal changes, especially those close to the body surface.

A common conception is that for steady unseparated aerofoil flow, substantial changes in velocity mainly occur within a thin layer close to the surface. A schematic picture of the velocity profiles for both the laminar and turbulent boundary layers along the surface normal is given in figure 3.1. There is a boundary beyond which the

velocity distribution is similar to that for irrotational flow. Within this boundary the velocity is mainly parallel to the surface and, in accordance with this distribution, vorticity is only significant in this latter region. As illustrated in figure 3.2, this thin layer, between the body surface and the boundary, is of special importance in the vortex method, and is referred to as the vorticity layer. For attached flows the thickness of this layer is small, which justifies the use of a vortex sheet placed near the surface to represent the effect of the vorticity, even in viscous flow.

A similar boundary can be identified for separated flows, which might include a vortex bubble, recirculating zone (dead zone), and vortex wake, as illustrated in figure 3.3. The main difference from attached flows is that this boundary might be far away from the body surface. Within the boundary a flow particle has a significant normal velocity component in addition to the dominant tangential component in attached flows. Furthermore, along a normal line, the tangential velocity component can change sign, resulting in a complicated vorticity distribution. Together with the enlargement of the vorticity layer, it becomes difficult to represent this influence using a simple vortex model.

The distinction between the vorticity layer and the remaining flow enables the restriction of computational resources to a relatively small area, and is one of the traditional advantages of vorticity methods. The boundary, however, is time dependent in unsteady flows, hence the vorticity layer is continually evolving. Boundary layer theory explains the formation process of the velocity profile for attached flows. Microscopically the exchange of molecules between different layers results in the exchange of their momentum, which retards the faster layer while speeding up the slower. Macroscopically the shear force, which exists because of viscosity and the flow velocity gradient, has a tendency to neutralise the speed differences. This formation mechanism leads to an assumption that the boundary layer is gradually moving from its initial position, which is coincident with the body surface at the start, to its final steady position. Correspondingly the thickness of the vorticity boundary increases from zero initially to a stable value.

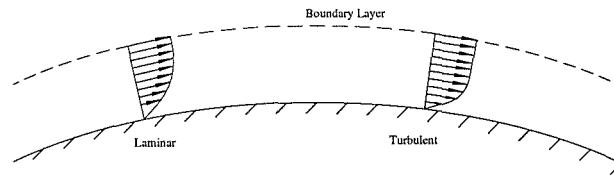


Figure 3.1: Illustration of velocity distribution near surface

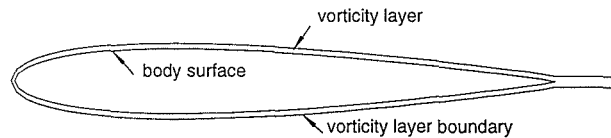


Figure 3.2: Illustration of vorticity layer of attached flows

In accordance with the developing velocity profile and vorticity layer thickness, the vorticity at the surface reduces from infinity at the start to a finite value. However, the integrated vorticity in the normal direction throughout the layer remains finite and constant, indicating that vorticity originates at the body surface. The development of the vorticity layer proceeds through a continuous process of creation followed by diffusion and convection, although the latter has less effect initially.

Further expansion of the vorticity layer arises when the flow starts to separate. In the early stages of separation, the normal velocity component is gradually increased at some points within the vorticity layer, hence the resultant velocity vector is diverted from the previously dominant tangential direction. The additional normal velocity component carries the vorticity away from the body and thus the vorticity layer is expanded.

The increase in normal velocity is mainly due to pressure differences, but deceleration in the tangential direction due to viscosity and turbulence also occurs. Viscous and turbulent effects are believed to be the main factors in the growth of velocity gradients in the normal direction. The normal velocity gradient in the tangential direction near the separation point usually grows from a very small value. This indicates that, similar to unseparated flow, the strength of vorticity previously created at this

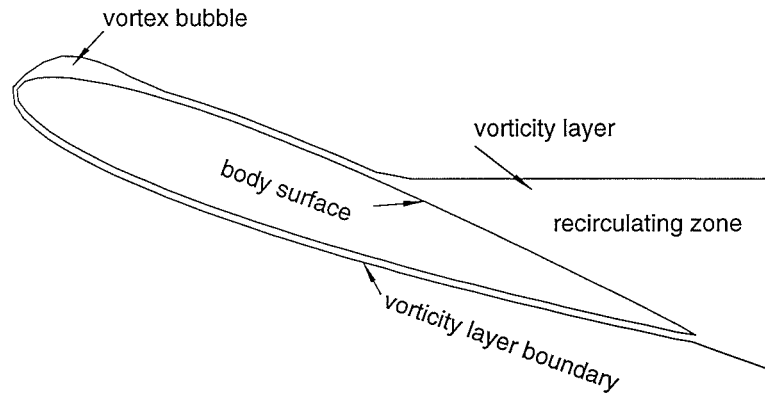


Figure 3.3: Illustration of vorticity layer of separated flows

point over a short time interval is small, although at other locations higher gradients result in greater vorticity strength. This moderate creation rate, for both unseparated flows and flows near separation points, means that only a small portion of vorticity within the layer is transferred through the previous boundary. Based on the above physical reasoning, a model is developed to represent the processes described.

3.2 Discretization – description of vorticity

Vorticity is contained within the vorticity layer, which is thin for unseparated flows but significantly larger for separated zones. Outwith this relatively small region there is zero or almost zero vorticity, therefore discretization in the form of vortices is required only within this layer.

Mathematically, vorticity $\omega(x, y, t)$, as a function of position (x, y) in two dimensional flows and time t , can be written in terms of strength $\Gamma(x_i, y_i, t)$ and associated distribution functions $f_i(x, y, t)$, that is,

$$\omega(x, y, t) = \sum_i \Gamma(x_i, y_i, t) f_i(x, y, t) \quad (3.1)$$

where (x_i, y_i) is a discrete point within the vorticity layer. Obviously, for an exact

representation, the Dirac distribution

$$f_i(x, y, t) = \delta(|x - x_i| + |y - y_i|)$$

should be associated with an infinite number of vortices, representing infinitely fine discretization. A finite discretization model is, however, accompanied by the complicated distribution functions, since the functions are dependent on all of the discrete positions as well as the Γ values. As exact distribution functions are very difficult to deduce, it is simpler to invoke an approximation whereby the (x_i, y_i) and the $f_i(x, y, t)$ are predefined. When the (x_i, y_i) are well distributed the problem can be further simplified by using the same distribution function for every discrete point at any time.

The simplest approximation employs the Dirac distribution $f_i = \delta(|x - x_i| + |y - y_i|)$. This simulation is equivalent to the model using point vortices at discrete points. However, the singularities at discrete points of the velocity field induced by this model limit its application. For example the model is inappropriate in cases where vortices are densely distributed, which is often the case for flows near bodies, in an attempt to improve the fidelity. This, however, will increase velocity field perturbations because of the singular nature of the functions.

Several cutoff functions are available which do not exhibit singular behaviour. These include Lamb and Rankine type core functions. The former can be expressed in the form

$$f(r) = \frac{1}{2\pi\sigma^2} e^{-\frac{r^2}{2\sigma^2}}$$

with corresponding velocity induced by an isolated vortex

$$u(r) = \frac{\Gamma}{2\pi r} (1 - e^{-\frac{r^2}{2\sigma^2}})$$

Similar expressions for the Rankine model are

$$f(r) = \begin{cases} \frac{1}{\pi\sigma^2} & r \leq \sigma \\ 0 & r > \sigma \end{cases}$$

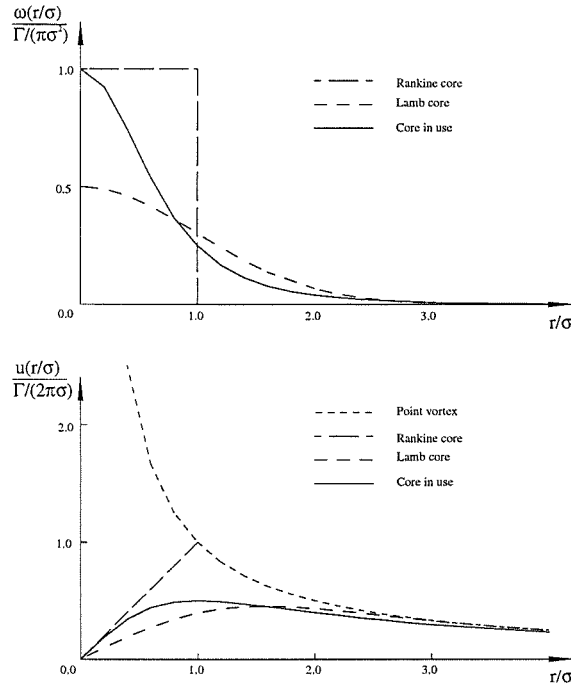


Figure 3.4: Vorticity and velocity distributions for various cores

$$u(r) = \begin{cases} \frac{\Gamma}{2\pi} \frac{r}{\sigma^2} & r \leq \sigma \\ \frac{\Gamma}{2\pi r} & r > \sigma \end{cases}$$

where parameter σ is the core radius and r is the distance between the vortex and the point of interest, $r = \sqrt{(x - x_i)^2 + (y - y_i)^2}$. The core functions and velocity profiles are illustrated in figure 3.4.

For an isolated vortex the exponential Lamb core gives an exact solution for the N-S equations if the core is expanded as $\sigma = \sqrt{2\nu t}$. However it has been proven that a system of vortices with expanding cores converges to the solution of a different equation.¹²⁵ Even if a fixed core radius was employed, evaluation of the exponential function consumes more computer resource than simple addition and multiplication operations.

The Rankine core has a uniform distribution of vorticity within the core. The core velocity is linear with respect to distance from the core center. Beyond the core radius the velocity profile follows that for a point vortex. There is, therefore, a

requirement for a decision process, which increases the computing cost.

Further simplifying the Rankine core results in another core function, that is

$$\begin{aligned} f(r) &= \frac{\sigma^2}{\pi(\sigma^2 + r^2)^2} \\ u(r) &= \frac{\Gamma}{2\pi} \frac{r}{(\sigma^2 + r^2)} \end{aligned} \quad (3.2)$$

which was first proposed by Spalart.¹²⁹ This profile is also illustrated in figure 3.4.

Comparing the various cores, the main differences in velocity are concentrated near the core center. Since no single core function can exactly simulate the real vorticity distribution, especially for flows governed by the non-linear N-S equations, it is difficult to claim superiority for any one core. It can be seen, however, that the point vortex yields the worst representation of vorticity, with the induced velocity tending to infinity as the distance goes to zero. The simplified Rankine core function has the advantage of utilising the same formula regardless of distance, thereby dispensing with the requirement for a decision process.

With this core the velocity $\vec{u}(\vec{r})$ of a particle with position vector \vec{r} , induced by the vorticity field discretized into a number of vortices of strength Γ_i at position \vec{r}_i , is

$$\vec{u}(\vec{r}) = \sum_i \frac{\Gamma_i}{2\pi} \frac{\vec{k} \times (\vec{r} - \vec{r}_i)}{(\sigma^2 + |\vec{r} - \vec{r}_i|^2)} \quad (3.3)$$

which is equivalent to the first integral in the velocity expression (2.25) given in the previous chapter. The corresponding stream function ψ is

$$\psi = - \sum_i \frac{\Gamma_i}{4\pi} \ln(\sigma^2 + |\vec{r} - \vec{r}_i|^2) \quad (3.4)$$

The flux through a panel connecting two points a and b equals the difference in the stream function evaluated at these points. Therefore the contribution from the vorticity to this flux is

$$\Delta\psi_{ab} = - \sum_i \frac{\Gamma_i}{4\pi} \ln \frac{(\sigma^2 + |\vec{r}_b - \vec{r}_i|^2)}{(\sigma^2 + |\vec{r}_a - \vec{r}_i|^2)} \quad (3.5)$$

In addition to an appropriate core function, proper distribution of the discrete points makes for a better representation of the vorticity field, and hence contributes to a successful simulation. The level of difficulty in determining such points depends on the complexity of the underlying vorticity distribution. The task is relatively easy for thin layers in which the significant vorticity variation occurs in one dimension. Hence discrete points can be distributed in the relevant direction without causing significant discrepancy. However, the above scheme is suitable only for the early stages of vorticity production, when the layer is normally thin. As the layer expands vorticity variations in other dimensions become important, and careful thought must be given to the discretization process.

The fact that the vorticity layer develops from a thin envelope around the body, in which vorticity is created, to become possibly more extensive suggests that it would be reasonable to divide the vorticity layer into two zones. These are the creation zone and the wake zone as shown in figure 3.5, with the zone boundary in between. The zone boundary is a curve parallel to the body surface displaced a short distance from it. Inside the creation zone, discrete points are distributed along a curve parallel to the boundary, and are fixed with respect to the surface regardless of the external flow development. These points are illustrated in figure 3.6. The distance of the curve from the surface is predefined in accordance with the assumption of velocity profile and the size of the creation zone. In the wake zone, however, the number and position of points depend on the flow evolution. The number is variable, starting from zero at the beginning when the wake does not exist. The number varies with vorticity exchange between the two zones, and vortex merging in the wake to limit computational cost. The positions are determined in accordance with the convection and diffusion scheme employed.

It is arguable whether a fixed size creation zone at the very early stage of vorticity layer formation is appropriate, when the zone might be bigger than the layer itself. It is almost impossible to simulate a very fine structure like a small vorticity layer unless a very high resolution scheme is employed. For this reason, it is assumed that

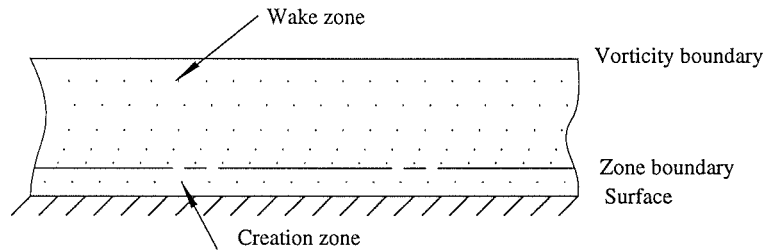


Figure 3.5: Illustration of creation zone and wake zone

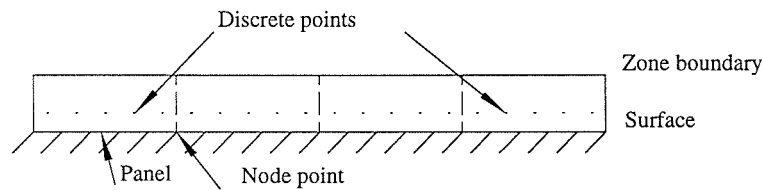


Figure 3.6: Discrete points in creation zone

the vorticity layer envelopes the entire creation zone from the start of the simulation.

As illustrated in figure 3.7, for convenience the set of discrete points used to represent the body surface also provides the basis for the discretization of the vorticity within the creation zone. (x_j, y_j) and (x_{j+1}, y_{j+1}) , or in complex notation $Z_j = x_j + \mathbf{i} y_j$ and $Z_{j+1} = x_{j+1} + \mathbf{i} y_{j+1}$, are two adjacent surface node points. They define a segment of surface and a flat panel. Further equal division of the segment by $(K - 1)$ sub-node points yields K sub-panels connecting them. It is the sub-panels which are directly related to the discretization of the vorticity in the creation zone.

A small strip of the creation zone, enclosed by the body surface normals at two adjacent node points, is divided into K sub-zones by the surface normals at the sub-node points. The vorticity in each sub-zone is represented by a vortex with the simplified Rankine core function referred to previously. As illustrated in figure 3.8, the vortices are located at points

$$Z_m = \frac{1}{2}(Z_j^k + Z_j^{k+1}) + \mathbf{i} \delta Z_n^k \quad (3.6)$$

where Z_j^k is the position of the k th sub-node on the j th segment with $Z_j^1 = Z_j$ and

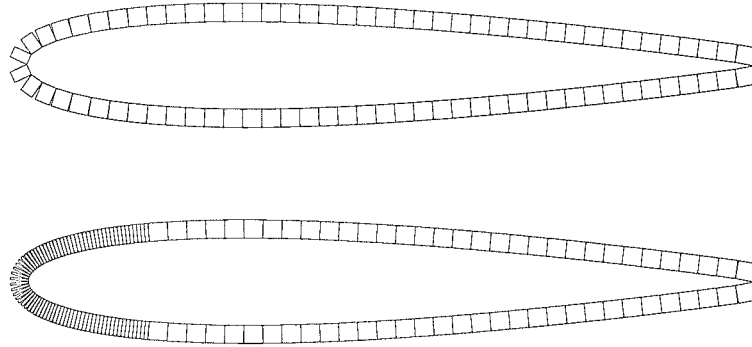


Figure 3.7: Discretization of surface

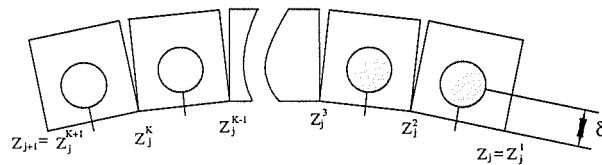


Figure 3.8: Multi-panel discretization of vorticity upon a curved segment

$Z_j^{K+1} = Z_{j+1}$, while $Z_{n_j}^k$ is the corresponding unit normal. Index m indicates the sub-zone in which the vortex is located, with $m = (j - 1) * K + k$.

In many instances the surface is relatively flat, for example most of an aerofoil surface except the leading edge. The vortex locations can then be simplified for a flat surface, and are given by

$$Z_m = \left(\frac{(K - k + 0.5)}{K} Z_j + \frac{(k - 0.5)}{K} Z_{j+1} \right) + i \delta Z_{n_j} \quad (3.7)$$

which only includes node points rather than sub-node points as the latter are implicitly defined by linear interpolation. This is illustrated in figure 3.9.

The discretization of vorticity in the creation zone into one vortex in the normal direction can only represent the integral effect of vorticity in this direction. This is equivalent to the discrete representation of a vortex sheet of strength γ on a curve displaced a distance δ from the body surface. The variation in γ along the tangential direction reflects the vorticity distribution; it is assumed to be linear within each panel and continuous across panel boundaries. The circulation of an individual vortex is

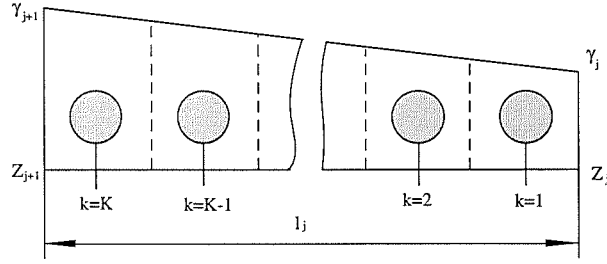


Figure 3.9: Discretization of vorticity upon a straight segment

therefore a function of γ_j , the vortex sheet strength at node point j , that is

$$\Gamma_m = \left(\frac{(K - k + 0.5)}{K} \gamma_j + \frac{(k - 0.5)}{K} \gamma_{j+1} \right) |Z_j^{k+1} - Z_j^k| \quad (3.8)$$

for segments with higher curvature or

$$\Gamma_m = \left(\frac{(K - k + 0.5)}{K} \gamma_j + \frac{(k - 0.5)}{K} \gamma_{j+1} \right) \frac{|Z_{j+1} - Z_j|}{K} \quad (3.9)$$

for plane segments. Index m , as before, is the sub-zone counter.

In contrast to the vortices in the creation zone, the positions of the vortices in the wake zone are tracked in accordance with the flow particles to which they are attached. This Lagrangian scheme provides an exact solution of the vorticity transport equation for inviscid flows. The existence of viscosity in real flows is simulated by giving the particles an additional displacement corresponding to a random walk. After a short time interval of Δt , the vortex at $(t + \Delta t)$ is moved from $Z_w(t)$ to

$$Z_w(t + \Delta t) = Z_w(t) + \left(\frac{3}{2} V_w(t) - \frac{1}{2} V_w(t - \Delta t) \right) \Delta t + (\eta_x + \mathbf{i} \eta_y) \quad (3.10)$$

Complex variable V_w is the velocity of the flow particle, and η_x and η_y are Gaussian random numbers with zero mean and standard deviation of $\sqrt{2\nu\Delta t}$, or $\sqrt{2\Delta t/Re}$ in dimensionless form.

Both convection and diffusion of vorticity during this period are reflected in the displacement of the vortices; the circulation of each vortex at the new location is unchanged, that is $\Gamma_w(t + \Delta t) = \Gamma_w$. As a result, the rediscritization process is similar to vortex advancement.

The contributions to the stream function and velocity at position Z , from the vorticity in the creation and wake zones, are

$$\psi(Z) = - \sum_{m=1}^{N_m} \frac{\Gamma_m}{4\pi} \ln(|Z - Z_m|^2 + \sigma^2) - \sum_{w=1}^{N_w} \frac{\Gamma_w}{4\pi} \ln(|Z - Z_w|^2 + \sigma^2) \quad (3.11)$$

$$V(Z) = \sum_{m=1}^{N_m} \frac{\Gamma_m}{2\pi} \frac{\mathbf{i}(Z - Z_m)}{(|Z - Z_m|^2 + \sigma^2)} + \sum_{w=1}^{N_w} \frac{\Gamma_w}{2\pi} \frac{\mathbf{i}(Z - Z_w)}{(|Z - Z_w|^2 + \sigma^2)} \quad (3.12)$$

which are the discretized version of the relevant integrals presented in the previous chapter. N_m and N_w are the total number of discrete points in the creation zone and wake zone respectively. This velocity excludes the contributions from the free stream and the body motion, which are required in the Z_w calculation.

By substituting for Γ_m , the stream function becomes a function of the unknown γ 's

$$\begin{aligned} \psi(Z) = & - \sum_{j=1}^N \frac{\gamma_j}{4\pi} \sum_{k=1}^K \frac{(K - k + 0.5)}{K} |Z_j^{k+1} - Z_j^k| \ln(|Z - Z_m|^2 + \sigma^2) \\ & - \sum_{j=1}^N \frac{\gamma_{j+1}}{4\pi} \sum_{k=1}^K \frac{(k - 0.5)}{K} |Z_j^{k+1} - Z_j^k| \ln(|Z - Z_m|^2 + \sigma^2) \\ & - \sum_{w=1}^{N_w} \frac{\Gamma_w}{4\pi} \ln(|Z - Z_w|^2 + \sigma^2) \end{aligned} \quad (3.13)$$

This indicates that the discretization has reduced the problem of determining an infinite dimensional vorticity distribution into one of evaluating a finite number of γ 's.

The overall circulation, around a contour bounded by the external and internal surfaces, which accompanies this discretization is

$$\Gamma = \sum_{m=1}^{N_m} \Gamma_m + \sum_{w=1}^{N_w} \Gamma_w \quad (3.14)$$

which contains the circulation of vortices within the creation zone and wake zone, and can, therefore, be considered also as incorporating the integral of vorticity throughout the real flow region.

An alternative to this model is a vortex simulation of flow within the vorticity layer based on the time history of the layer thickness. Its application, however, encounters

several obstacles. First of all, prior knowledge is required of the layer thickness, which is difficult to identify and might necessitate a return to a grid dependent method. Secondly, a mechanism is required to represent the effect of changing thickness at different stages. Furthermore, the capacity of such a model is limited to unseparated flows, since the layer after separation is no longer thin and the velocity profile cannot be easily represented by a simple vortex model. All of these disadvantages disappear by dividing the vorticity layer into a creation zone and wake zone as discussed.

3.3 Determination of flow

One of the main tasks in predicting incompressible flows is to determine the velocity field. This can be evaluated using the vorticity field with the assistance of the boundary conditions.

3.3.1 Vorticity field

According to the discretization previously described, the determination of the vorticity field relies on the calculation of the γ 's defined in the creation zone. This can be done through implementation of the boundary conditions.

In the previous chapter, the no-slip and no-penetration boundary conditions were reduced to a problem of maintaining the value of the surface stream function difference, between the flow and the body, equal to a constant around the surface. For a stationary body this means the surface line is a streamline. Although this alignment is destroyed by the existence of normal surface velocity due to motion of the body, the constancy of the stream function difference is equivalent to specifying the velocity of the flow particle equal to that of the associated surface point. Hence implementation of the boundary conditions only requires operating on the stream functions at the boundary.

The surface points chosen for the purposes of the stream function boundary conditions are those node points specified in the previous section identified by index j .

This index is increased in the clockwise or anticlockwise direction along the surface, therefore points j and $j + 1$ are adjacent. Through a panel j , which connects neighbouring node points Z_j and Z_{j+1} , the flux due to the velocity of a moving solid body is the difference between the stream function at points Z_{j+1} and Z_j , that is

$$F_{jS} = \Im(\bar{V}_{c_i}(Z_{j+1} - Z_j)) - \frac{1}{2}\Omega_i(|Z_{j+1} - Z_{c_i}|^2 - |Z_j - Z_{c_i}|^2) \quad (3.15)$$

resulting from the stream function given in the previous chapter. For the same panel, the flux due to the velocity field in the flow region consists of four parts, that is

$$F'_{jS} = F_{jF} + F_{jC} + F_{jW} + F_{jB} \quad (3.16)$$

which represents respectively the contributions from the free stream, vorticity in the creation zone, vorticity in the wake zone and vorticity inside the body arising from its motion. The flux from the free stream F_{jF} can be expressed as

$$F_{jF} = \Im(\bar{V}_{\infty}(Z_{j+1} - Z_j)) \quad (3.17)$$

while the fluxes from vorticity in the creation and wake zones are

$$\begin{aligned} F_{jC} = & - \sum_{i=1}^N \frac{\gamma_i}{4\pi} \sum_{k=1}^K \frac{(K - k + 0.5)}{K} |Z_i^{k+1} - Z_i^k| \ln \frac{(|Z_{j+1} - Z_m|^2 + \sigma^2)}{(|Z_j - Z_m|^2 + \sigma^2)} \\ & - \sum_{i=1}^N \frac{\gamma_{i+1}}{4\pi} \sum_{k=1}^K \frac{(k - 0.5)}{K} |Z_i^{k+1} - Z_i^k| \ln \frac{(|Z_{j+1} - Z_m|^2 + \sigma^2)}{(|Z_j - Z_m|^2 + \sigma^2)} \end{aligned} \quad (3.18)$$

$$F_{jW} = - \sum_{w=1}^{N_w} \frac{\Gamma_w}{4\pi} \ln \frac{(|Z_{j+1} - Z_w|^2 + \sigma^2)}{(|Z_j - Z_w|^2 + \sigma^2)} \quad (3.19)$$

by making use of the stream functions in the previous section.

A more complicated term is the discretized form of the flux contributed by vorticity inside the body region F_{jB} . The stream function contribution from this region can be written in integral form. In particular, the stream function at the surface point with position vector \vec{r}_s is simply

$$\psi_i(\vec{r}_s) = -\frac{\Omega_i}{\pi} \iint_{B_i} \ln |\vec{r}_s - \vec{r}| dB_i$$

which is equivalent to the effect of a uniform vorticity field, $2\Omega_i$, within this region. \vec{r} is the position vector of infinitesimal region dB_i . The logarithmic integrand can be further manipulated by employing the identity

$$\frac{\vec{r} - \vec{r}_s}{|\vec{r} - \vec{r}_s|^2} = \nabla \ln |\vec{r} - \vec{r}_s|$$

Application of Gauss' Theorem in region B_i , bounded by surface S_i , yields

$$\iint_{B_i} \frac{\vec{r} - \vec{r}_s}{|\vec{r} - \vec{r}_s|^2} dB_i = \int_{S_i} \vec{n} \ln |\vec{r} - \vec{r}_s| dS_i$$

Hence the velocity at position \vec{r}_s , written as the following double integral over region B_i

$$\vec{u}_i(\vec{r}_s) = -\frac{\Omega_i}{\pi} \iint_{B_i} \frac{\vec{k} \times (\vec{r} - \vec{r}_s)}{|\vec{r} - \vec{r}_s|^2} dB_i$$

can be cast into a line integral along boundary S_i

$$\vec{u}_i(\vec{r}_s) = -\frac{\Omega_i}{\pi} \int_{S_i} \vec{s} \ln |\vec{r} - \vec{r}_s| dS_i$$

where \vec{s} is the unit tangential vector associated with surface element dS_i at \vec{r} . The flux through panel j is the integral, over the panel, of the normal velocity component

$$F_{jB} = \int_{S_j} \vec{n} \cdot \vec{u}_i(\vec{r}_s) dS \quad (3.20)$$

which is also the difference between the relevant components of the stream functions at the panel ends. \vec{r}_s and \vec{n} are, respectively, the position and unit normal associated with infinitesimal element dS . The flux and velocity are detailed in appendix A.

Equating F_{jS} and F'_{jS} for each of the N body panels results in N simultaneous linear equations for the N unknown γ 's at the node points. However only $N - 1$ of the equations are required to satisfy the mass flow boundary conditions, and the remaining equation is therefore redundant. The N th equation comes from the single-valued pressure requirement detailed in the previous chapter, which states that the total circulation of vorticity entering the flow from the body surface is balanced by an

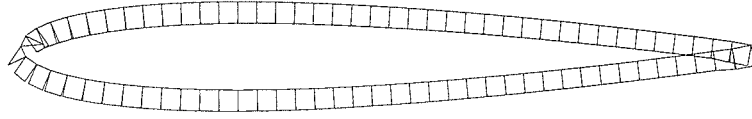


Figure 3.10: First time step γ distribution for the NACA0012 at 0°

equal reduction of circulation within the body region. The combined N independent linear simultaneous equations

$$[\mathbf{A}]\{\gamma\} = \{\mathbf{F}\} \quad (3.21)$$

is sufficient to determine the N γ 's which approximate the vorticity in the creation zone.

A continuous γ distribution may be appropriate for a smooth surface, but might not be sufficient to reflect the γ variation near a sharp edge. Further consideration of how γ can be better modelled is given in section 3.9. At present, first step γ distribution is shown in figure 3.10 for the NACA0012 at 0° . The result is from the modified model detailed in section 3.9.

Given the position and strength of the wake vortices and the γ distribution, the entire vorticity field is determined.

3.3.2 Velocity Field

Similar to the composition of the stream function, the velocity of a flow particle at position $\vec{\mathbf{r}}_p$ is composed of four components,

$$\begin{aligned} \vec{\mathbf{u}}(\vec{\mathbf{r}}_p) &= \vec{\mathbf{u}}_\infty + \sum_{m=1}^{N_m} \frac{\Gamma_m}{2\pi} \frac{\vec{\mathbf{k}} \times (\vec{\mathbf{r}}_p - \vec{\mathbf{r}}_m)}{(|\vec{\mathbf{r}}_p - \vec{\mathbf{r}}_m|^2 + \sigma^2)} \\ &+ \sum_{w=1}^{N_w} \frac{\Gamma_w}{2\pi} \frac{\vec{\mathbf{k}} \times (\vec{\mathbf{r}}_p - \vec{\mathbf{r}}_w)}{(|\vec{\mathbf{r}}_p - \vec{\mathbf{r}}_w|^2 + \sigma^2)} - \frac{\Omega_i}{\pi} \int_{S_i} \vec{\mathbf{s}} \ln |\vec{\mathbf{r}} - \vec{\mathbf{r}}_p| dS_i \end{aligned} \quad (3.22)$$

or in complex form

$$\begin{aligned} V(Z_p) &= V_\infty + \sum_{m=1}^{N_m} \frac{\Gamma_m}{2\pi} \frac{\mathbf{i}(Z_p - Z_m)}{(|Z_p - Z_m|^2 + \sigma^2)} + \sum_{w=1}^{N_w} \frac{\Gamma_w}{2\pi} \frac{\mathbf{i}(Z_p - Z_w)}{(|Z_p - Z_w|^2 + \sigma^2)} \\ &- \frac{\Omega_i}{\pi} \int_{S_i} \mathbf{i} Z_n(Z) \ln |Z - Z_p| dS_i \end{aligned} \quad (3.23)$$

representing the effects of the free stream, vorticity in the creation zone, vorticity in the wake zone and vorticity inside the body as shown previously in integral form. $Z_n(Z)$ is the unit complex normal of infinitesimal element dS_i . The last integral term is detailed in appendix A, expressed in terms of the nodal coordinates.

The above velocity governs the movement of flow particles and also the convection of vorticity, and is used in section 3.2 to determine the advancement of the vortices at each instant of time.

The discretization of the vorticity into vortices and the surface into panels means that the no-slip, no-penetration boundary conditions will not be satisfied at all points on the surface. The effect will be to produce perturbations in the velocity of particles in the flow region, both in the creation zone and the wake zone, and a mechanism will be discussed later to account for this, especially close to the body surface.

3.4 *Shedding of Vorticity*

The shedding of vorticity is defined herein as the net vorticity entering the wake zone during a given time interval, taking account of vorticity crossing the zone boundary. This process is modelled by introducing new vortices into the wake zone, with a strength consistent with the transport of vorticity between the zones.

As for general transportation of vorticity, both convection and diffusion contribute to the exchange of vorticity between the two zones. Although both processes occur simultaneously, as described by the N-S equations, (2.2), a good approximation for short time intervals is provided by operator splitting

$$\begin{aligned}\frac{\partial \omega}{\partial t} + \vec{\mathbf{u}} \cdot \nabla \omega &= 0 \\ \frac{\partial \omega}{\partial t} &= \nu \nabla^2 \omega\end{aligned}$$

Accordingly, advancement of a vortex with a velocity equivalent to that for inviscid flows is followed by a diffusion process to incorporate the influence of viscosity. In the wake zone the diffusion process is modelled by a random walk as described in

section 3.2. It is very likely that some vortices will cross the zone boundary during a given time interval and advance into the creation zone. These vortices are eliminated from the wake zone after being integrated with the existing vorticity in the creation zone, and discretized in the same manner. The eliminated particles are referred to as absorbed vortices.

Simultaneously, some of the vorticity in the creation zone may cross the zone boundary into the wake zone. This vorticity is represented by vortices, which are in fact the source of all vorticity in the wake.

The new wake vorticity can be categorised into two groups, each of which is discretized separately according to the processes of convection and diffusion. Consequently an individual vortex from the creation zone is split into three vortices, one remaining in the creation zone (remaining vortex) and the other two in the wake zone, referred to as the convected and diffused vortices.

The new wake vorticity is distributed mainly in a narrow region along the zone boundary, hence the new wake vortices are located adjacent to the boundary. For a vortex of strength Γ_m located at Z_m at time t , the diffused vortex at time $t + \Delta t$ is placed at

$$Z_m^d = Z_m + ((\beta - 1)\delta + \sqrt{\delta^2 + 2\nu\Delta t})Z_{n_j}^k$$

or

$$Z_m^d = Z_m + ((\beta - 1)\delta + \sqrt{\delta^2 + 2\nu\Delta t})Z_{n_j} \quad (3.24)$$

depending on the panel representation of the surface. The convected vortex is placed at

$$Z_m^c = Z_m^s + [(\beta + 1)\delta + (\delta_m - \delta)\frac{1}{\beta + 1}]Z_{n_m}^s \quad (3.25)$$

where $Z_{n_m}^s$ is the unit normal of the surface at point Z_m^s , the nearest surface point to

$$Z_m(t + \Delta t) = Z_m + V(Z_m)\Delta t$$

The remaining vortex is placed at

$$Z_m^r = Z_m^s + (\delta_m - (\delta_m - \delta) \frac{\beta}{\beta + 1} \delta) Z_{n_m}^s \quad (3.26)$$

δ_m is the distance from the surface. Subscripts j , k and m are related as previously indicated for surface discretization. The positions of both the convected and remaining vortices are in accordance with an assumed tangential velocity profile in the normal direction within the creation zone. This approach is taken to better represent the distribution of vorticity from the surface up into the wake zone. If y is the dimensionless distance from the surface with respect to the creation zone size, that is $y = 0$ at the surface and $y = 1$ at the zone boundary, the tangential velocity profile $u(y)$, $u(0) = 0$ and $u(1) = 1$, is assumed to be of the form

$$u(y) = 1 - (1 - y)^\beta$$

The corresponding vorticity profile $\omega(y)$, which has a maximum value of unity, is

$$\omega(y) = (1 - y)^{(\beta-1)}$$

if the normal velocity gradient in the tangential direction is ignored. $\beta = 1$ corresponds to a linear velocity distribution along the normal and a uniform vorticity, while $\beta = 2$ corresponds to a linear vorticity distribution. Both velocity profiles and vorticity profiles for $\beta = 1$ and $\beta = 2$ are shown in figure 3.11.

In accordance with the above velocity profile, the convected vortex has strength

$$\Gamma_m^c = \Gamma_m \left(\frac{\delta_m - \delta}{(\beta + 1)\delta} \right)^\beta$$

which is the circulation of the portion of vorticity located outside the zone boundary after the entire vorticity patch has moved at the velocity of its discrete point. The remaining portion is represented by another vortex, namely the remaining vortex. Clearly, there is no convected vortex if the particle has a tendency to move towards the body.

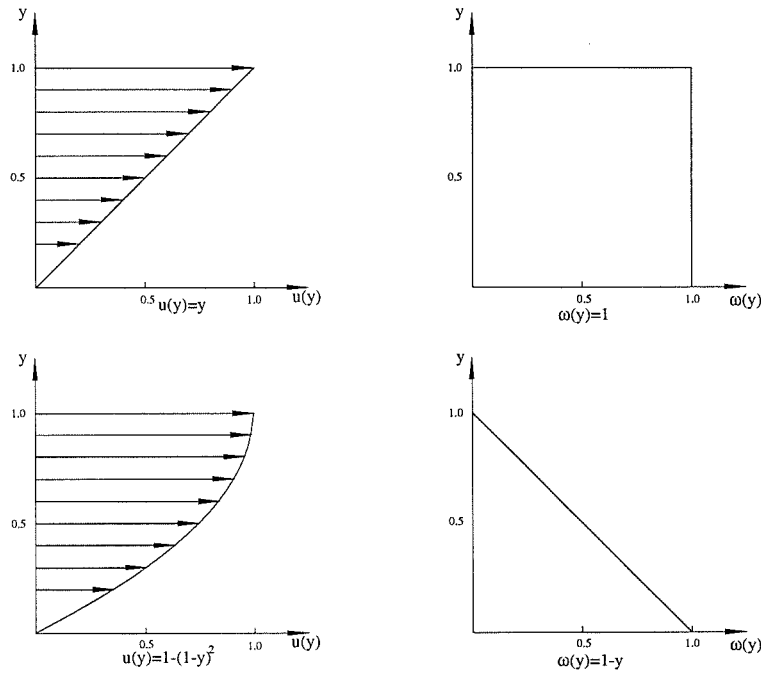


Figure 3.11: Assumed velocity and vorticity profiles in creation zone

The strength of the diffused vortex is represented by

$$\Gamma_m^d = \Gamma_m \left(1 - \sqrt{\frac{\delta^2}{\delta^2 + 2\nu\Delta t}} \right) \quad (3.27)$$

which is similar to a core expansion from δ to $\sqrt{\delta^2 + 2\nu\Delta t}$, while the strength of the remaining vortex is given by

$$\Gamma_m^r = \Gamma_m - \Gamma_m^c - \Gamma_m^d \quad (3.28)$$

The convected vortex model above only accounts for the shedding of vorticity from a smooth surface. Special treatment is required at a sharp edge, such as an aerofoil trailing edge, where there is a section of the zone boundary which is not parallel to the surface due to the undefined tangent. The same principle, which regards convection as the shifting of a patch of distributed vorticity, applies to this section of the zone boundary.

Depending on the position Z_m , there are three possible outcomes for an individual patch: no shedding; part shedding; complete shedding. The position and strength of

both the convected vortex and remaining vortex are decided in accordance with the proportion of the patch outwith or within the zone boundary, as previously described.

The diffusion is only modelled in the normal direction since the normal velocity is relatively small, especially for attached flows, in contrast to the dominant tangential velocity. The effect of diffusion in the tangential direction is outweighed by the magnitude of the convection term and associated error due to the discretization.

The distinction between the convected vortex and diffused vortex is only made for the new vorticity crossing the zone boundary. Subsequently, these vortices are all regarded as wake vortices and advance as described previously.

The significance of the contributions to the shedding of vorticity from convection and diffusion varies around the surface, depending on the flow state. For attached flow on a smooth surface, diffusion is the main cause of shedding. This contrasts with separated flow near the separation point, where the importance of convection is dramatically increased. Regardless of whether the flow is separated or not, convection always dominates the shedding at sharp edges.

The division of the flow zone and vortex splitting model described above reflect the fact that only a portion of the vorticity crosses the zone boundary through convection and diffusion, rather than the entire vortex, as simulated by some other models. Most of the vorticity strength is preserved within the creation zone and discretized at the next time instant, leaving only a small amount for the creation of new wake vortices. This scheme limits the error caused by the inaccuracy of vortex transportation within both the creation and wake zones due to the discretization, and enables the linear distribution of γ to more closely represent reality. These features have not been included in some models, where vortices of full strength are released into the wake. However, full shedding causes the errors to amplify with time, hence the linear γ distribution has increasing difficulty in representing the real vorticity distribution because of the presence of strong velocity perturbations. These errors also manifest themselves in the aerodynamic characteristics.

The capability of the model to simulate separation is attributed to the mechanism

governing diffusion and convection across the zone boundary, as this enables the gradual shedding of vorticity into the wake zone in accordance with flow viscosity and the velocity of the flow particles.

3.5 Creation of vorticity

Vorticity is created by interaction between the flow and surface of the body. The distribution of nascent vorticity is a consequence of the no-slip no-penetration boundary conditions. This new vorticity appears while existing vorticity in the creation zone is continuously shedding through the zone boundary into the wake region. The new vorticity is assumed to be contained within the creation zone during a small time interval, and is described by a vortex sheet of strength γ^n at the node points, distributed in accordance with the linear variation described previously. The created vorticity augments that already in existence due to absorption from the wake and that which remains from the previous shedding process, to form the total vorticity in the creation zone, which is described by the γ 's. The values of the γ 's are determined by implementing the boundary conditions as described previously, from which the γ^n 's are obtained by subtracting the existing vorticity, denoted γ^r . That is

$$\gamma_j^n = \gamma_j - \gamma_j^r \quad (3.29)$$

It is the distribution of γ_j^n which reflects the level of vorticity generated at the surface.

The distribution of existing vorticity within the creation zone, γ^r , is represented by a vortex sheet of the same form as the total vorticity. A vector $\{\mathbf{F}^r\}$ can be defined, whose elements are the mass flux or circulation contribution by the remaining and absorbed vortices to be eliminated. The solution for the γ^r 's is obtained from the following simultaneous linear equations

$$[\mathbf{A}]\{\gamma^r\} = \{\mathbf{F}^r\} \quad (3.30)$$

where matrix $[\mathbf{A}]$ is identical to that defined previously for the γ solution.

3.6 Pressure distribution

Static pressure on the body surface can be evaluated by integrating the pressure gradient along the surface contour. The surface pressure gradient expression was derived in the previous chapter. Together with the surface and temporal discretization, the gradient at node point j , \vec{r}_j , becomes

$$\frac{1}{\rho} \left(\frac{\partial P}{\partial s} \right)_j (t) = -\vec{s} \cdot \frac{\Delta \vec{u}_{c_i}}{\Delta t} - \frac{\Delta \Omega_i}{\Delta t} \vec{n} \cdot (\vec{r}_j - \vec{r}_{c_i}) + \Omega_i^2 \vec{s} \cdot (\vec{r}_j - \vec{r}_{c_i}) + \frac{\gamma_j^n}{\Delta t} \quad (3.31)$$

or in complex form

$$\frac{1}{\rho} \left(\frac{\partial P}{\partial s} \right)_j (t) = -\vec{s} \cdot \frac{\Delta V_{c_i}}{\Delta t} - \frac{\Delta \Omega_i}{\Delta t} \Re(Z_{n_j}(\overline{Z_j - Z_{c_i}})) - \Omega_i^2 \Im(Z_{n_j}(\overline{Z_j - Z_{c_i}})) + \frac{\gamma_j^n}{\Delta t} \quad (3.32)$$

These expressions are also valid if \vec{r}_j represents any point on the surface. A straight panel and linear γ^n distribution result in a linear distribution of pressure gradient. The pressure difference between the nodes of panel j is

$$P_{j+1} - P_j = \frac{1}{2} \left[\left(\frac{\partial P}{\partial s} \right)_{j+1} + \left(\frac{\partial P}{\partial s} \right)_j \right] \ell_j \quad (3.33)$$

while the pressure on the surface between these two points is

$$P = P_j + \left(\frac{\partial P}{\partial s} \right)_j s + \left[\left(\frac{\partial P}{\partial s} \right)_{j+1} - \left(\frac{\partial P}{\partial s} \right)_j \right] \frac{s^2}{2\ell_j} \quad (3.34)$$

with s the distance from Z_j . Both equations provide a relative pressure distribution rather than absolute pressure, for which the value of a reference pressure should be known. However, this is sufficient to determine the aerodynamic characteristics of the aerofoil.

The pressure force acting on panel j is

$$F(j) = - \left[P_j \ell_j + \frac{1}{3} \left(\frac{\partial P}{\partial s} \right)_j \ell_j^2 + \frac{1}{6} \left(\frac{\partial P}{\partial s} \right)_{j+1} \ell_j^2 \right] Z_{n_j} \quad (3.35)$$

and the corresponding moment around reference point Z_c is

$$\begin{aligned} M(j) = & \left[P_j \ell_j + \frac{1}{3} \left(\frac{\partial P}{\partial s} \right)_j \ell_j^2 + \frac{1}{6} \left(\frac{\partial P}{\partial s} \right)_{j+1} \ell_j^2 \right] \Im[(Z_j - Z_c) \overline{Z_{n_j}}] \\ & + \left[\frac{1}{2} P_j \ell_j^2 + \frac{5}{24} \left(\frac{\partial P}{\partial s} \right)_j \ell_j^3 + \frac{1}{8} \left(\frac{\partial P}{\partial s} \right)_{j+1} \ell_j^3 \right] \end{aligned} \quad (3.36)$$

After the summation of all the pressure forces on the panels of a closed body, the reference pressure term is eliminated. The same is true for the moment.

3.7 Amalgamation of vortices

Continuous convection and diffusion of vorticity through the boundary of the creation zone constantly increases the number of discrete vortices in the wake zone as the flow develops. This results in the growth of computing resource required, most noticeably in the determination of the particle velocities. However, when the vortices are far away from the body, little accuracy is lost in the induced surface velocity by employing a coarser distribution of greater strength vortices. The benefit gained is a reduction in the computational expenditure.

The reduction of vortex numbers can be achieved by merging those pairs satisfying a given criterion. For two vortices at Z_1 and Z_2 , with circulations Γ_1 and Γ_2 respectively, the corresponding induced velocities at a surface point Z_0 are

$$\begin{aligned} V_1(Z_0) &= \frac{\mathbf{i} \Gamma_1}{2\pi} \frac{1}{\overline{Z_0 - Z_1}} \\ V_2(Z_0) &= \frac{\mathbf{i} \Gamma_2}{2\pi} \frac{1}{\overline{Z_0 - Z_2}} \end{aligned}$$

The location of Z_0 is determined from either Z_1 or Z_2 , whichever is the closer to the surface. A single vortex at Z with strength Γ induces the velocity

$$V(Z_0) = \frac{\mathbf{i} \Gamma}{2\pi} \frac{1}{\overline{Z_0 - Z}}$$

without considering the vortex core effect. When the difference

$$\Delta V = V(Z_0) - V_1(Z_0) - V_2(Z_0)$$

is sufficiently small, vortices at Z_1 and Z_2 are merged into a single vortex at Z .

The velocity difference can be written as

$$\Delta V = \frac{\mathbf{i}}{2\pi} \frac{1}{\overline{Z_0 - Z_n}} \left[\Gamma \frac{\overline{Z_0 - Z_n}}{\overline{Z_0 - Z}} - \Gamma_1 \frac{\overline{Z_0 - Z_n}}{\overline{Z_0 - Z_1}} - \Gamma_2 \frac{\overline{Z_0 - Z_n}}{\overline{Z_0 - Z_2}} \right]$$

where Z_n is a selected point such that $\left| \frac{\overline{Z_1 - Z_n}}{Z_0 - Z_n} \right| < 1$, $\left| \frac{\overline{Z_2 - Z_n}}{Z_0 - Z_n} \right| < 1$ and $\left| \frac{\overline{Z - Z_n}}{Z_0 - Z_n} \right| < 1$. Provided these conditions are satisfied the terms can be expanded in Taylor series

$$\frac{\overline{Z_0 - Z_n}}{\overline{Z_0 - Z_1}} = 1 + \frac{\overline{Z_1 - Z_n}}{Z_0 - Z_n} + \left(\frac{\overline{Z_1 - Z_n}}{Z_0 - Z_n} \right)^2 + \dots$$

with similar expressions for $\frac{\overline{Z_0 - Z_n}}{Z_0 - Z_2}$ and $\frac{\overline{Z_0 - Z_n}}{Z_0 - Z}$. The error is minimized for the following merged vortex values

$$\Gamma = \Gamma_1 + \Gamma_2 \quad (3.37)$$

$$Z = \frac{\Gamma_1 Z_1 + \Gamma_2 Z_2}{\Gamma} \quad (3.38)$$

The merging criterion, which is based on the residual error, is

$$\frac{\Gamma_1 \Gamma_2}{\Gamma} \left| \frac{(Z_2 - Z_1)^2}{(Z_0 - Z_n)^3} \right| < V_{crit} \quad (3.39)$$

Z_n must satisfy the previously stated conditions. If Z_1 is closer to Z_0 than Z_2 , and Z_n coincides with Z_1 , the combined criteria are

$$\begin{aligned} |Z_2 - Z_1| &< \min \left(1, \frac{|\Gamma|}{|\Gamma_2|} \right) |Z_0 - Z_1| \\ \frac{\Gamma_1 \Gamma_2}{\Gamma} \left| \frac{(Z_2 - Z_1)^2}{(Z_0 - Z_1)^3} \right| &< V_{crit} \end{aligned} \quad (3.40)$$

The merging process preserves circulation and first moment of vorticity. The merging criteria control the discrepancy in second moment of vorticity to an acceptable degree. Whether two vortices merge depends on their separation, the distance from the body surface and also their circulations. Vortices which are closer to each other and further away from body surface are more likely to be merged. In addition, vortices of the same sign and low strength are more likely to be merged than ones of opposite sign and high strength.

The critical velocity for merging is based on the lowest order residual term of the Taylor expansion, that is order 2. Neglecting the higher order terms may result in more significant discrepancy if any of the expansion terms approach unity. A conservative measure is to reduce the upper limit of the distance ratios from unity to a small value, say 0.5.

The value of the critical velocity V_{crit} depends on the accuracy requirement. For flow around an aerofoil, where most of the vortices released near the leading edge remain in close proximity to the body surface for a significant time period, the requirement should be stricter close to the surface to avoid a noisy pressure distribution. In the far wake the velocity criterion can be relaxed, and a magnitude around 10^{-4} seems to be adequate in this region.

3.8 Boundary condition enhancement

The velocity of particles at discrete points within the creation zone plays a significant role in determining the strength of the nascent vortices. However, velocity perturbations can be expected, partly due to the discretization of vorticity and partly due to the implementation of the boundary conditions on a discretized form of the boundary. To reduce these perturbations, and their wider influence, a number of mechanisms are employed, some of which have been detailed previously.

Traditionally, the singular elements of a panel method have either been a sheet or point element, such as a vortex sheet or vortex point. In most models of the latter type, there is only one vortex point for each panel, with a strength equivalent to the total panel vorticity. The surface velocity distribution produced by this coarse discretization would be quite different from that required by the boundary conditions, which will be satisfied at a minimum of one location on each panel. This distribution can be greatly improved if the number of vortices per panel is increased from the solitary one. A comparison is given in figure 3.12, which shows the normal velocity distribution on a panel of the NACA0012 aerofoil at 0° angle of attack with different numbers of vortices. With the boundary conditions being implemented in the form of zero panel mass flux, the normal velocity is cancelled at more than ten locations in the five vortex model, compared with only five cancellations in the two vortex model. More generally, an increase in the number of vortices greatly reduces the normal velocity perturbation. This is in addition to the advantage, described previously, of

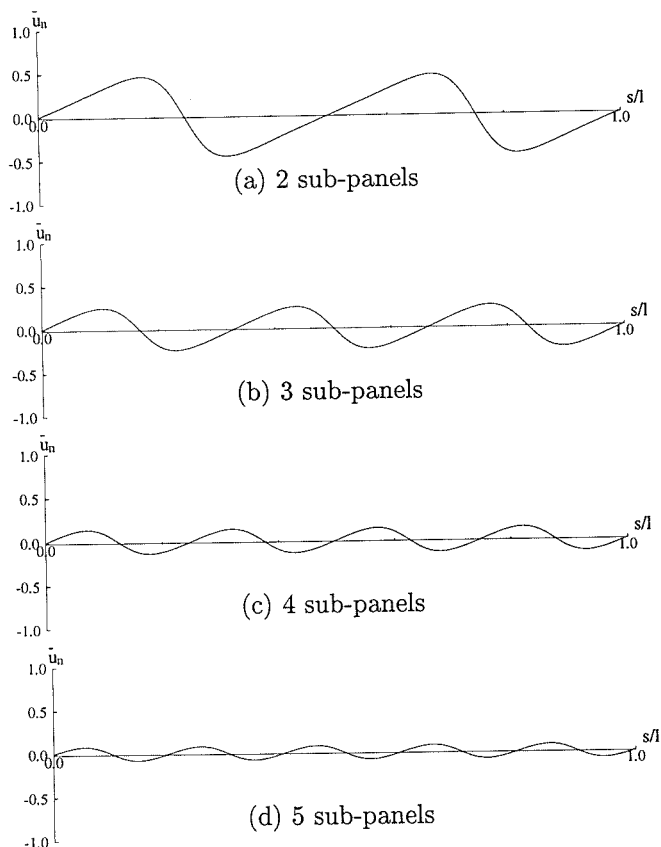


Figure 3.12: Normal velocity on panel for different numbers of panel vortices

a multi-panel discretization of the surface to represent high curvature segments.

A further advantage of the multi-vortex model comes from the reduced amount of vorticity crossing the zone boundary due to the above mentioned velocity perturbations. Increasing the number of vortices on the panels reduces the strength of each vortex. Combined with the accompanying lower normal velocity components, either towards or away from the body, the desired effect is achieved. A comparison of normal velocity components for models with different number of vortices is given in figure 3.13. The difference from the previous figure is in the sampling of the velocity along the line of the nascent vortices.

The continuous vortex sheet model may be more effective in reducing velocity perturbations because of the smoother vorticity and velocity distributions along the sur-

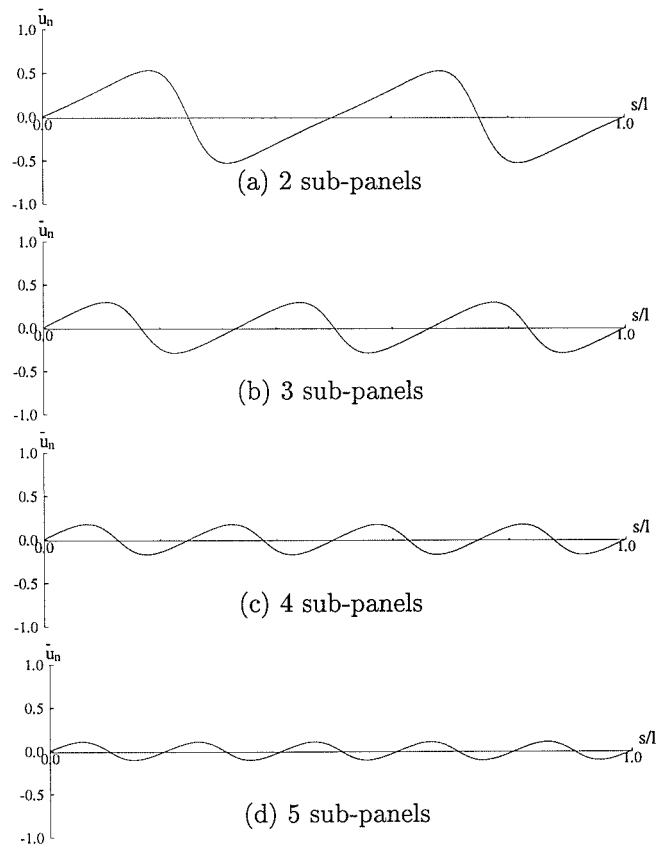


Figure 3.13: Normal velocity comparison along vortex creation line for different numbers of panel vortices

face and creation line. However, this advantage is usually offset by the perturbations introduced by subsequent discretization into vortices, which is normally necessary when advancing the vortex sheets in the wake. However, by discretizing the vortex sheet initially, before implementation of the boundary conditions and calculation of particle velocities, the present model exhibits the useful property of consistency.

Another measure which has been introduced is a grace strip, shown in figure 3.14, which is a small area attached to the outer boundary of the creation zone. If vorticity remains within this area after convection, it does not become a wake vortex. This has the dual effect of eliminating spurious separation due to velocity perturbations and removing convected vortices with very small strength. The addition of such vortices

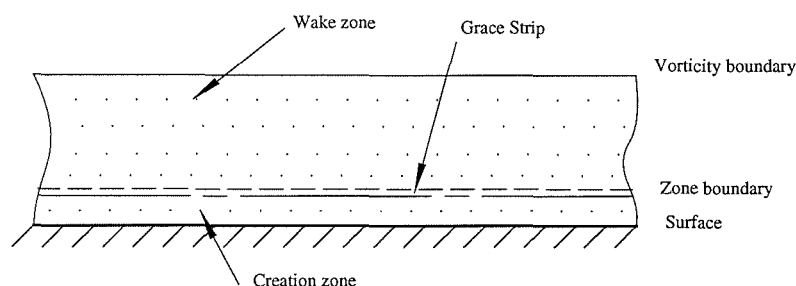


Figure 3.14: Additional control strip

to the wake zone can dramatically increase the computational cost without much benefit in terms of accuracy.

3.9 Sharp edge modelling

Along most of the surface, the piecewise continuity of the vortex sheet strength γ is acceptable for smooth segments where the change in normal from one panel to another is moderate. However special treatment is required at a sharp edge, such as an aerofoil trailing edge.

The value of γ represents the difference between the velocities at the zone boundary and corresponding point on the body surface. This difference does not change much across the junction of smooth segments due to gradual changes which occur there in the velocity field. However, this is not true at a sharp edge, and it is questionable whether panels joined at such points should share the same value of γ . It is desirable to have two separate γ values on each side of the sharp edge, although this requires one more relationship in addition to those arising from the regular boundary and pressure conditions.

In steady potential flow simulations, an infinitely thin vortex sheet is placed on the body surface, across which the velocity jumps by a value of γ . At a sharp edge, both the joined surface segments and the vortex sheet meet at a point, hence the flow velocity at this point should be the same on either segment. This establishes a

relationship between the two γ s and leads to the Kutta condition for aerofoils. In the present model, the flow is unsteady and the introduction of a creation zone separates the two corresponding zone boundary points, therefore the local velocity field implied by the steady Kutta condition does not exist. This extra relationship must come from other sources.

Along the creation zone boundary the above type of singularity does not exist, which implies that the velocity distribution along this curve does not exhibit sharp changes. This means that γ changes smoothly in the absence of a strong vortex group nearby, which should be the case during the first time step of the calculation, at least on the surface segment encountering the free stream. The γ distribution employed should therefore reflect these conditions.

A test case in which no distinction between a sharp or smooth edge was made, that is the two γ s were equalised, did not provide satisfactory results. Figure 3.15 illustrates the first time step γ distribution near the trailing edge of a NACA0012 aerofoil at 0° and 10° . As can be seen the γ distribution changes dramatically near the trailing edge over both upper and lower surfaces when the aerofoil is at 0° . The distribution near the trailing edge is spiky, changing rapidly from about zero. Such a distribution obviously does not satisfy the requirement previously discussed in relation to γ around the trailing edge area. Furthermore, the calculated γ in this region is highly dependent on the choice of node points, although the pattern is preserved. It can also be seen that, away from the trailing edge, the distribution is smooth and, in the most part, close to linear. Such linearity persists unless a strong vortex group is located around that portion of the surface. A much stranger result is observed in the 10° case, where γ on both the lower and upper surfaces changes erratically within a few panels near the trailing edge. This panel dependent γ can result in unrepresentative release of vorticity from the trailing edge at this early stage of the flow, although the change in γ becomes less pronounced at later time steps when the value at the trailing edge approaches zero.

Another test case was run in which a constant vorticity was specified on the lower

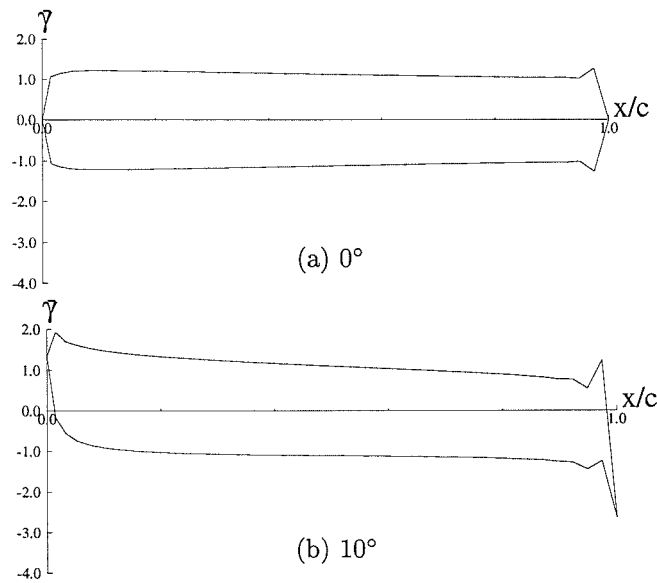


Figure 3.15: First time step γ distribution for model with equal trailing edge γ for upper and lower surface

surface panel connected to the sharp trailing edge. This was done by equating the γ values at the two panel nodes. The γ distribution for the first time step is shown in figure 3.16, from which it is apparent that the sudden changes in γ on the lower surface in the trailing edge region have been eliminated. Furthermore, increasing the number of vortices on each panel results in an even smoother γ distribution. Equally interesting is the constant γ achieved for the corresponding upper surface panel for this symmetric aerofoil at 0° .

For an aerofoil at 10° , one could expect a strong vortex group on the upper surface in the region near the trailing edge when the flow is impulsively started. This is reflected by the erratic γ variation on the associated panels in figure 3.16. In contrast to the case with equal γ at the trailing edge, the variation becomes insignificant with the full development of the flow when the bound circulation is established.

An alternative way to eliminate the additional unknown is to make use of the relatively smooth γ distribution on the lower surface, shown in figure 3.16, by linearly interpolating a node point value of γ from neighbouring trailing edge nodes. The first

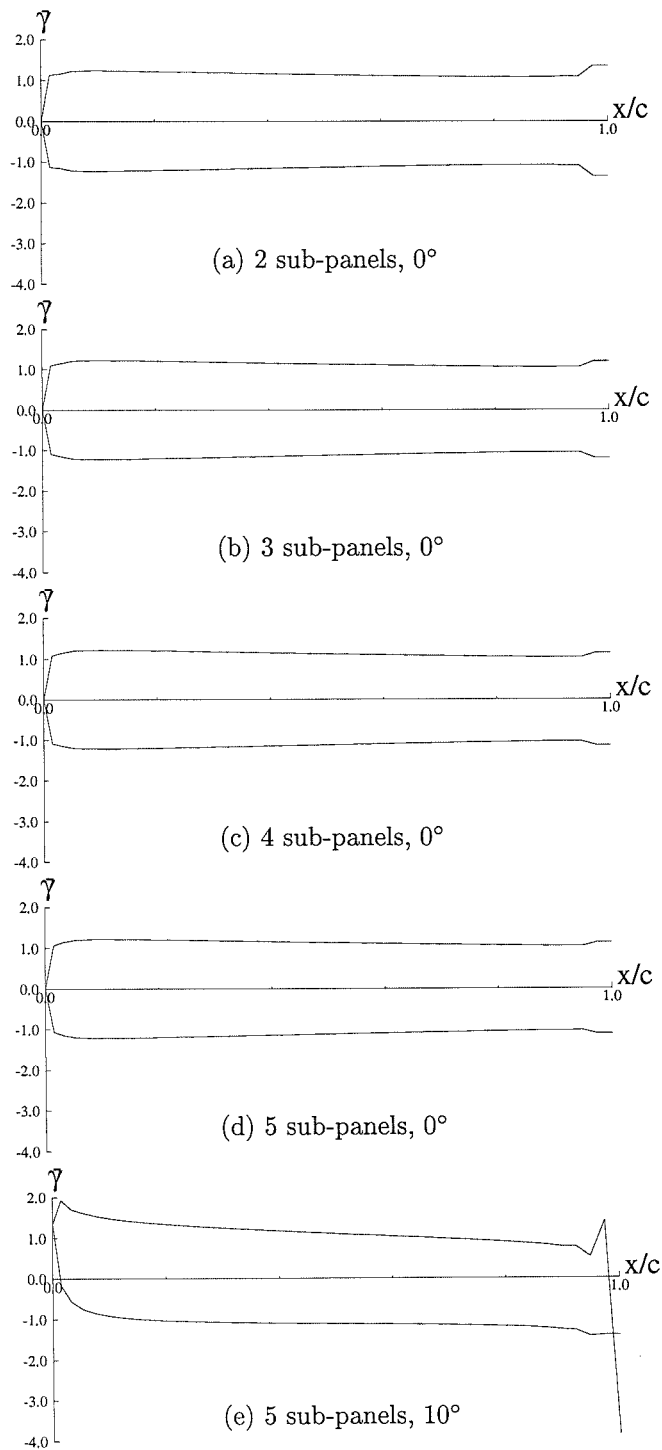


Figure 3.16: First time step γ distribution for model with constant γ on lower surface trailing panel

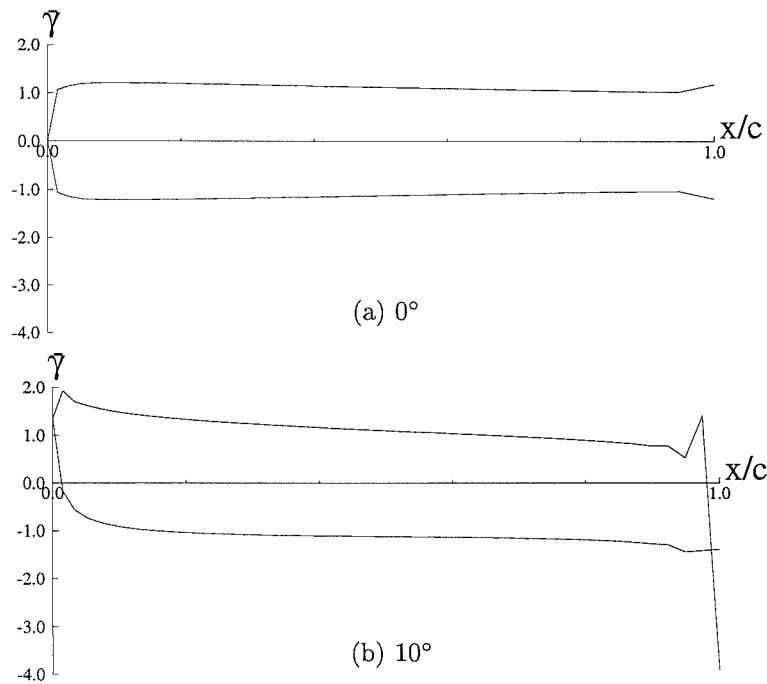


Figure 3.17: First time step γ distribution for model which interpolates γ on lower surface

time step result is illustrated in figure 3.17, with not much difference observed from the previous case. Both models fulfil the previously discussed requirements. For this reason the γ distribution defined in the previous case is employed in the model.

However, such γ de-coupling presents a new difficulty in representing the vorticity in a small region following the trailing edge. As shown, for 0° case, in figure 3.16, the magnitude of γ is large but of opposite sign on the adjoining panels. Consequently, in this trailing edge region, convected vortices of large circulation but opposite signs could be produced. Their interaction could produce unrealistic instabilities in the flow at later times. To avoid this, the following model is employed, which re-discretizes the vorticity in the trailing edge region into vortices.

As illustrated in figure 3.18, the trailing edge region is defined as the area enclosed by the two panel normals, two extended control zone boundaries which are parallel to the edge bisector, and a line normal to the bisector located $0.6V_\infty \Delta t$ downstream

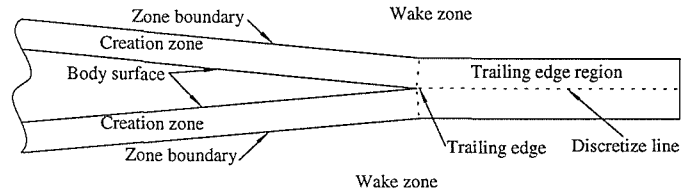


Figure 3.18: Illustration of trailing edge region

from the edge. Vortices within this zone are combined together and re-discretized into vortices along the bisector. The underlying γ distribution is assumed to be linear, and is determined by conserving both the stream function contribution at the trailing edge and the total circulation.

3.10 External constraints

The influence of the external constraints, detailed in continuous form in the previous chapter, has been implemented numerically. The explicit differences in the implementation from those without the constraints appear in equations (3.16), (3.23), (3.21) and (3.30) respectively for mass flux, velocity and linear simultaneous equations for γ and γ^r . The implicit differences exist in equations (3.19), (3.13), (3.23) and (3.18), which includes the interaction of vortices originating from the constraint surfaces.

The two vortex sheets at the external constraints, which are required to maintain the no slip and no penetration conditions, result in two additional terms in equation (3.16), representing their contribution to $\{\mathbf{F}\}$. Similarly, their contributions to velocity, equation (3.23), are accounted for by two additional terms which correspond to the relevant terms in equation (2.25). Since the vortex sheets have constant strength equal to $-/+u_\infty$, the above calculations are standard.

In addition to vorticity creation on the aerofoil surface, a thin region attached to each constraint is also identified as part of the creation zone. An identical discretization process is employed for all nascent vorticity, hence there are more unknown γ s

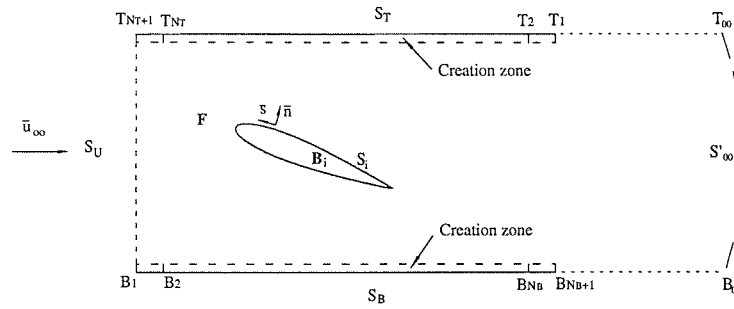


Figure 3.19: Illustration of constraints

associated with the constraints in equation (3.18).

The system is still solvable since more equations are available due to the boundary conditions at the constraints. As shown in figure 3.19, truncation occurs at T_1 and B_{N_B+1} on the upper and lower constraints, with T_∞ and B_∞ being their respective extensions to infinity. There are $(N_T + 1)$ unknown γ s for the N_T upper constraint panels and $(N_B + 1)$ γ s for the N_B lower constraint panels. This results in $(N_T + N_B)$ additional equations for the additional $(N_T + N_B + 2)$ unknowns. However, zero flux is prescribed on pseudo panels T_1 to T_∞ and B_{N_B+1} to B_∞ in order to fully satisfy the boundary conditions in region F_0 . This provides two more equations which combine with those for the body to form the expanded system of linear equations (3.21) and (3.30) for γ and γ^r .

3.11 Computational procedure

A diagram of the computational procedure is given in figure 3.20. The computation begins with preliminary procedures which include geometric calculations and initial construction of matrix $[\mathbf{A}]$ and vector $\{\mathbf{F}\}$ in equation (3.21). The geometric calculations are standard and generate the following: area of the body A ; length and unit normal of each panel ℓ_j and Z_{n_j} ; positions of vortices in creation zone Z_m (3.7). However, to avoid unnecessary repetition, the elements in $[\mathbf{A}]$ are divided into two groups representing the time independent components and those associated with the

motion of the body. Similar division of $\{\mathbf{F}\}$ is also made.

The computation proceeds as follows:

1. Calculate the time dependent components of elements in $[\mathbf{A}]$, (3.18 and section 2.7), and $\{\mathbf{F}\}$, (3.15, 3.17, 3.19, 3.20, and section 2.7), and combine them with the time independent components to generate the full $[\mathbf{A}]$ and $\{\mathbf{F}\}$.
2. Solve the simultaneous linear equations (3.21) for $\{\gamma\}$.
3. Obtain, from the γ s, the circulation of vortices in the creation zone in accordance with equations (3.8) or (3.9).
4. Calculate the velocity of vortices in the creation zone and in the wake zone, if any, by making use of equation (3.23).
5. Increase the time by a step Δt .
6. Update the position of the body surface, the surface normals $Z_{n,j}$ and the nascent vortex positions in the creation zone Z_m in accordance with the prescribed motion.
7. Convect and diffuse vortices in the creation zone, calculate the shedding of vorticity across the zone boundary in accordance with section 3.4, and record the contribution to $\{\mathbf{F}^r\}$ from existing vortices within the zone earmarked for rediscrretization.
8. Convect and diffuse vortices in the wake zone, if any, in accordance with equation (3.10), eliminating those which cross the creation zone boundary. Solve equation (3.30)
9. Merge pairs of vortices satisfying criteria (3.40).
10. Calculate the contribution to $\{\mathbf{F}\}$ from the vortices in the wake zone.
11. Repeat steps 1 and 2.

12. Obtain $\{\gamma^n\}$, representing the newly created vorticity during the time step, from 3.29.
13. Calculate the surface pressure gradient (3.32), force (3.35) and moment (3.36).
14. Repeat the above steps, starting from step 3.

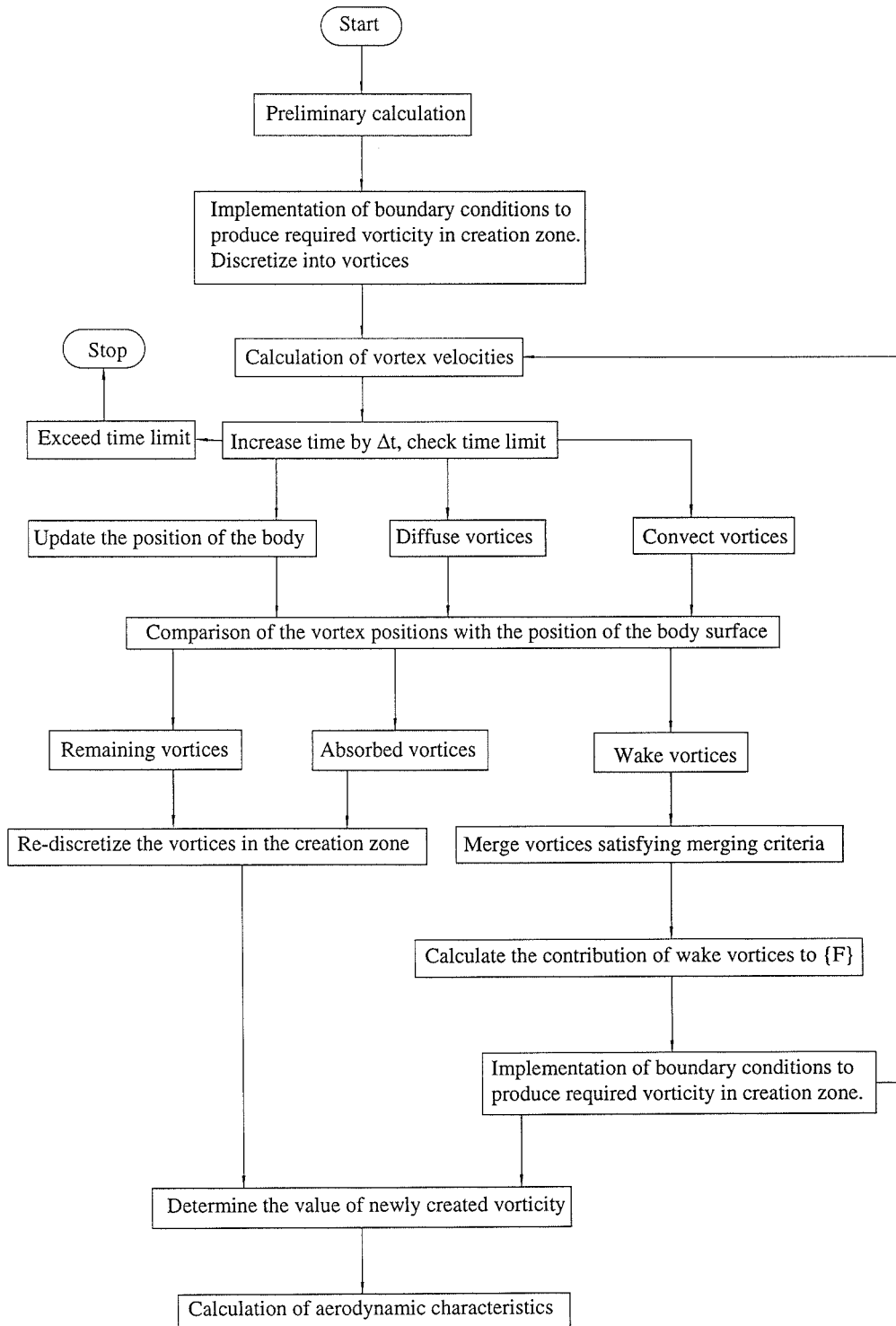


Figure 3.20: Flow diagram of computational procedure

Chapter 4

FLOW PREDICTION AND ANALYSIS

Presented in this chapter are the results obtained from the application of the numerical model described in chapters 2 and 3 to a variety of flows around aerofoils. The test cases demonstrate the capabilities of the model and therefore, to some extent, serve the purpose of validation. Whereas the results presented in many previous simulation studies of dynamic stall flow have been limited to the qualitative geometric flow structures, this study incorporates quantitative comparisons with experimental data. Results are presented for both the NACA0012 and NACA0015, although more detail is given for flows around the former section.

Three types of unsteady flow cases are considered: impulsively started flows; flows around pitching aerofoils; constrained flow around aerofoils. The flows are all assumed to be incompressible and two dimensional.

For all cases, eighty panels are used to represent the aerofoil surface, each panel composed of five sub-panels. Most of the panels are of similar length, especially away from the leading edge. To provide a better representation of surface curvature, however, the panel length is gradually reduced as the leading edge is approached. At the leading edge, the length is about half of those panels close to the trailing edge.

In common with most flow simulations using vortex methods, empirical parameters are employed in the computation. These include the vortex core radius and the creation distance from the surface of the nascent vortices. Both values have comparable dimensions to the sub-panel lengths.

4.1 *Impulsively started flows*

This flow is also referred to as an unsteady static flow. The initial condition is of a potential flow around a fixed aerofoil with zero bound circulation. The flow velocity is uniform at infinity and there is initially no vorticity except in a thin layer enveloping the aerofoil. The vorticity in this thin layer, referred to as the creation zone in this thesis, is represented by nascent vortices. The flow evolution expected from this initial condition includes the development of the surface pressure distribution and aerodynamic loads. This is associated with the growth of bound circulation over time, counterbalanced by vortex shedding mainly from the trailing edge. The computational results reflect these events.

Figures 4.1(a) and 4.1(b) illustrate the development of the normal force coefficient at various incidences for the NACA0012 and NACA0015 aerofoils respectively. It can be seen that the results from the simulations gradually approach the corresponding experimental data, reduced from its original form². In contrast to other published results¹¹², no significant overshoot of the coefficients is predicted. The surface pressure distributions at different fixed incidences around the NACA0012 at $tV/c = 20$ are shown in figure 4.2(a), while the development of static pressure around the NACA0012 at 10° is presented in figure 4.2(b). It can be clearly seen that smooth pressure distributions are predicted by the model for these cases.

Figures 4.3(a) and 4.3(b) show the corresponding build-up of circulation within the creation zone. Since the flow is attached, the curve gradients reflect the level of the circulation of vorticity shedding from the trailing edge. It is evident that the circulation approaches constant values asymptotically, with higher circulation when the aerofoil is at higher incidences. This is echoed by the vortex pattern in figure 4.4, which illustrates the roll-up, at an early stage, of vortices shed from trailing edge. The intensity of the roll-up increases with increasing incidence as a direct consequence of the bigger circulation assigned to the vortex blobs. In addition, the vortices convect downstream as time progresses while more vortices are continually shed from the

aerofoil. The absence of roll-up of the later vortices is a sign that their total circulation is diminishing. At $tV/c = 15.00$, the starting vortex is in the far wake and a line of vortices extends from the trailing edge in a manner consistent with the Kutta condition. For unseparated aerofoil flow at small incidence, a simple vortex method with vortex shedding from the trailing edge only would produce a similar vortex pattern. The method proposed herein regains this ability in contrast to other surface vortex shedding methods, some of which employ techniques to suppress shedding to avoid early separation¹²⁹.

Presented along with the vortex patterns are the corresponding streamlines which indicate, as expected, attached flow around the aerofoil. The velocity field is directly related to compression and expansion of the streamlines as they deflect around the aerofoil, greater compression close to the surface leading to higher velocities and hence lower pressures. The extent of streamline deflection is also a measure of the strength of the starting vortex and hence the circulation around the aerofoil.

The increasing strength of starting vortex with incidence can be better identified in figure 4.5, in which the contours of velocity magnitude and vertical velocity component are presented. The area in the wake with the concentration of contour lines marks the starting vortex: the more dense the lines the higher is the gradient. Therefore the increase in contour density with incidence indicates the shedding of stronger vortices.

4.2 *Flows around pitching aerofoils*

The distinctive flow features arising from an aerofoil in pitching motion have been identified as the delay of separation, the formation of the dynamic stall vortex, and its subsequent passage over the upper surface. These processes have been simulated by the numerical model for the case of the NACA0012 undergoing a ramp-up from -1° to 40° at a pitch rate $\kappa = 0.0415$. The flow structures are illustrated in figure 4.6, and associated velocity magnitude contours in figure 4.7. The correlations of normal

force, tangential force, and moment with experimental data are given in figure 4.8, and the comparison of surface pressure distributions in figure 4.10(a).

The computation employed the same angle of attack history as in the experiment¹⁶, shown in figure 4.8. For each discretized time step in the computation, the exact value of incidence is obtained by interpolating between experimentally measured incidences, the sample frequency of which was lower. The quoted pitch rate refers to the main motion outwith the transition zones at each end for acceleration and deceleration respectively. The Reynolds number in the experiment was $Re = 1,500,000$.

During the ramp-up motion, the main features in the vortex pattern and streamlines are similar to those for attached flow described for the static case. However, this pattern occurs at an angle of attack $\alpha = 21.4^\circ$, as shown in figure 4.6, well beyond the static stall angle for this aerofoil. As can be seen, vortices are mainly shedding from the trailing edge and the flow is unseparated. This assessment is supported by the absence of circulatory regions in the streamline pattern. As the incidence continues to increase, vortices begin to accumulate on the upper surface and the associated streamlines indicate the development of a bubble-like disturbance at $\alpha = 23.6^\circ$, $\alpha = 27.8^\circ$, and $\alpha = 28.3^\circ$. An identifiable leading edge vortex has formed at $\alpha = 31.9$, along with a smaller vortex upon the rear half of the surface. As illustrated in the streamline patterns for $\alpha = 35.2^\circ$ to $\alpha = 37.6^\circ$, it seems that the stronger leading edge vortex sucks the weaker vortex forward and merges with it while being transported over the upper surface. The formation of a counter vortex near the trailing edge occurs when the dynamic vortex passes above the edge, which is clearly visible in the patterns for $\alpha = 38.4^\circ$ and $\alpha = 38.8^\circ$. The plots in lower left corners of the vortex patterns are the corresponding pressure distributions during the process.

Figure 4.7 presents velocity magnitude contours at various times during the ramp motion. At $\alpha = 21.45^\circ$, the contour pattern is typical of that for attached flow around an aerofoil. At $\alpha = 27.83^\circ$, however, the contours become more dense in the area near the upper surface, indicating the existence of high velocity gradients associated

with the presence of intense vorticity. The vortices shedding near the leading edge remain close to the surface for a substantial time period during their downstream transportation, which might be a factor in initiating the separation process along the surface. The effect could be similar to that of natural flow turbulence on the diffusion of vorticity. However, uncertainty remains about this process and further investigation is needed to establish the connection between the numerical parameters and the physical parameters like Reynolds number. The subsequent frames illustrate the formation of the dynamic stall vortex and its transport along the surface, indicated by the clusters of dense contours. The development of the counter vortex mentioned above can also be identified near the trailing edge.

The comparisons between the computational results and experimental data¹⁶ are shown in figure 4.8, which presents the normal force, tangential force and moment coefficients versus dimensionless time and angle of attack. Excellent agreement is illustrated in the normal force coefficient during the attached flow phase. In addition, the main features of the vortex-induced normal force and its subsequent collapse have been simulated, although some of the post-stall details are different. Particularly satisfying is the close agreement in the indicated time of separation.

The comparison of tangential force coefficients shows good agreement during attached flow and for part of the stall and post-stall phase. The main features of the dynamic stall vortex formation and transport have been simulated, although the details of the vortex-induced component show discrepancies.

The moment coefficient comparison also indicates excellent agreement during the attached flow phase. The build up and passage of the dynamic stall vortex have been simulated to a high degree, as has the associated moment break. The discrepancies in the post-stall region are due to the details of the counter vortex which forms near the trailing edge. Note that the moment break occurs prior to the break in normal force, which is consistent with the results of many experimental investigations.

Similar agreement is obtained with experiment⁵ for the case of the NACA0015 undergoing ramp-up motion at a pitch rate $\kappa = 0.0487$ and Reynolds number $Re =$

990,000, as illustrated in figure 4.9.

More insight into the capacity of the model is given by figures 4.10(a) and 4.10(b), which illustrate the correlation of computational and experimental pressure distributions for the NACA0012 and NACA0015 performing the previously described ramp-up motions. There is a good match between the pressures before the formation of the dynamic stall vortex. However, there is a small offset between the experimental and computational distributions, which is probably due to defining the pressure with respect to a reference at the approximate stagnation point. The adoption of this approximation avoids the necessary, and expensive, calculation of the pressure constant, which does not affect the calculation of the overall aerodynamic loads. Discrepancies exist in the detailed effects of the dynamic stall vortex on the surface pressure at higher incidences, although the main pressure pulse is simulated. The resolution of the surface geometry and vorticity representation, the size of vortex core and the lack of small scale turbulence modelling are all undoubtedly contributory factors.

The pressure spike at the leading edge originates in the vorticity solution around the high curvature zone, which requires more linear panels than were employed in the study. The unnaturally high strength vortices which enter the wake from this region could also be a factor in the core size of the stall vortex.

The ad hoc turbulence generated by vortices near the surface only exists while shed vortices remain close to the surface. However, more vortices would be required to model this effect properly. Alternatively, a distributed eddy viscosity model could be implemented as for large eddy simulations. This would lead to greater vortex diffusion and possibly better correlations in the pressure pulse and post-stall loads at higher incidence. The importance of turbulence following separation is well documented for grid base methods¹⁶³⁻¹⁶⁵, which seem to produce quite different aerodynamic characteristics with different turbulence models.

The existence of wind tunnel walls in the experiment could also affect the transportation of the dynamic stall vortex. To what extent this is the case is investigated in the next section.

Notwithstanding the above, the model has demonstrated its ability in simulating the influence of geometry and pitch rate on aerodynamic characteristics. Figure 4.11 presents the results for the NACA0012 and NACA0015 undergoing the same ramp-up motion at a pitch rate $\kappa = 0.0415$. No significant difference is observed. The results for both aerofoils at various pitch rates are shown in figures 4.12(a) and 4.12(b). As expected, higher pitch rates result in further delay of dynamic stall.

In summary, the model has demonstrated its ability to simulate the primary features of unsteady flows around pitching aerofoils, including aerodynamic characteristics in good agreement with experimental data. It is considered that the establishment of a relationship between the numerical parameters and physical properties, the modification of the leading edge modelling, and the incorporation of turbulence would further improve its capabilities.

4.3 *Constrained flows around aerofoils*

The effect of wind tunnel blockage on unsteady flows is an area which has not been significantly addressed. For a simulation, the flow region is now limited by the existence of upper and lower constraints, and only the fluid within the constraints is of interest. The determination of the effects of these constraints on the aerodynamic loads and pressures is the aim of such a study, and results are presented in this section to achieve this.

In the computation, the two parallel lines which model the constraints are separated by $3.872728c$, the width of the test section of the University of Glasgow's "Handley Page" wind tunnel. The external constraints only extend from $2c$ upstream to $4c$ downstream of the quarter chord position to avoid excessive computational cost. The aerofoil's quarter chord point is "fixed" mid-way between the constraints which corresponds with the experimental set-up¹⁶. Other conditions remain unchanged.

Figure 4.13 shows the constraint effect for impulsively started flow around the NACA0012 at 10° at the two instants $tV/c = 0.50$ and $tV/c = 15.0$. The pictures on

the left and right correspond to infinite flow and constrained flow respectively, with the position of the wind tunnel walls coinciding with the upper and lower boundaries of the relevant pictures. The streamlines next to the constraints remain parallel to them as a result of the no penetration condition, while the corresponding streamlines for the open flow are slightly deflected. The velocity magnitude contours illustrate some differences in the velocity field, but these are insignificant in the area near the body for such a moderate incidence.

The pictures in figure 4.14 illustrate the typical vortex and streamline patterns for the NACA0012 undergoing ramp-up motion at $\kappa = 0.0415$, in this case with external constraints present. Comparing with the results presented in the previous section, at $tV/c = 7.40$, the effect of the constraints on the flow near the body are not readily apparent. However, at $tV/c = 8.00$, the pressure distribution, vortex patterns and streamlines resemble more those for open flows at $tV/c = 8.20$, while those for constrained flow at $tV/c = 8.20$ are closer to those for open flow at $tV/c = 8.30$. This suggests an earlier separation for constrained flow. Comparing the pictures for $tV/c = 9.90$, the dynamic stall vortex for constrained flow has been transported further rearwards.

Figure 4.15 presents a comparison of the streamline patterns for the two flows. As in figure 4.13, the position of the wind tunnel walls coincides with the upper and lower boundaries of the pictures on the right. In contrast to the patterns for attached flow at low incidence, the effect of the constraints on the streamline pattern in the presence of the stall vortex is quite marked, with greater compression evident. It can be concluded that the dynamic stall vortex is closer to the trailing edge in the constrained case.

The difference in velocity field is shown in figures 4.16 and 4.17, in which contours of velocity magnitude and vertical velocity component are presented. It can be seen that stronger velocity gradients appear very close to the body for constrained flow at high angles of attack, which not only affects the shedding of vorticity from the surface but also influences the formation and subsequent transport of the dynamic

stall vortex.

Three sets of aerodynamic characteristics are presented in figure 4.18 for the NACA0012. The data correspond to infinite flow, flow with the previously defined constraint separation of $3.872728c$, and constrained flow with half this separation. These constraints are referred to as constraints 1 and 2 respectively. The results show that constrained flow separates earlier and stalls earlier. This effect is more pronounced in the flow with constraints 2.

In figure 4.19 experimental data are plotted with the predicted results for both infinite flow and the flow with the experimental constraints simulated. The numerical data for constrained flow are in better agreement with those from experiment.

The pressure distributions for the NACA0012 and NACA0015, during ramp-up motion at $\kappa = 0.0415$ and $\kappa = 0.0487$ respectively, are illustrated in figures 4.20(a) and 4.20(b). The plots include experimental data, infinite flow data and constrained flow data. Little effect of the constraints is observed before $\alpha = 25.8^\circ$ for the NACA0012 and $\alpha = 28.0^\circ$ for the NACA0015. However, the constrained flow pressure distribution over the rear part of the upper surface is in good agreement with experimental data at $\alpha = 36.6^\circ$ for the NACA0012 and $\alpha = 38.2^\circ$ for the NACA0015. This reflects the actual situation as the experimental data have not been subject to wind tunnel correction.

Due to a lack of techniques to account for wind tunnel wall effects, most dynamic stall experimental data have not been corrected. The differences illustrated in this section between infinite and constrained flow suggests that a more accurate representation of the flow field requires incorporation of external constraints in the numerical simulation.

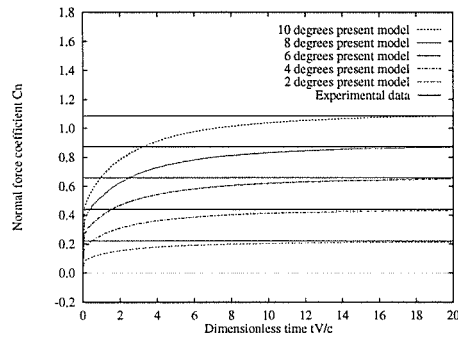
4.4 Ramp-up and Ramp-down motion

The process of flow reattachment on an oscillating aerofoil which experiences dynamic stall is of interest to aerodynamicists. Figures 4.21 and 4.22 present computational

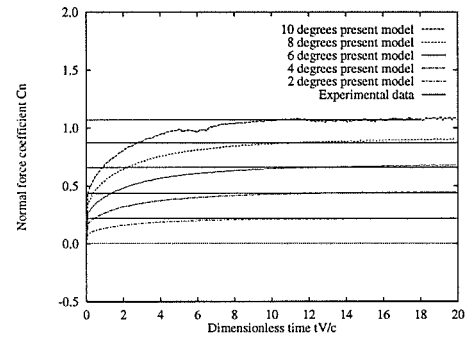
results for flow around the NACA0012 undergoing ramp-up motion immediately followed by ramp-down motion. As shown in the top picture of figure 4.22, the angle of attack increases from 0° to 40° and then decreases to -10° . The pitch rate of the motion $\kappa = 0.0415$ for ramp-up and -0.0415 for ramp-down, with smooth transition periods between the phases to avoid the generation of unrealistically high impulse forces. The Reynold number is $Re = 1,500,000$.

In figure 4.21, the vortex patterns and streamlines are shown at four instances of time, two during the upstroke and two during the downstroke. The main features discussed in previous sections for the ramp-up motion appear during the upstroke phase, where no separation is observed until an angle of attack as high as 21.35° , at $tV/c = 4.50$, is reached. With increasing angle of attack, the separation which initiates near the leading edge is followed by the formation and subsequent transport of the dynamic stall vortex over the upper surface towards the trailing edge and into the far wake. However, of particular note during the downstroke is the clear reattachment of the separation line on the upper surface from the leading edge to the trailing edge, culminating in full reattachment. This process is clearly illustrated in the lower two frames in figure 4.21.

Figure 4.22 presents the normal force, tangential force and moment coefficients against both dimensionless time tV/c and angle of attack. The hysteresis loops are apparent in this case. As expected the reattachment is delayed to a relatively low angle of attack during the down stroke.

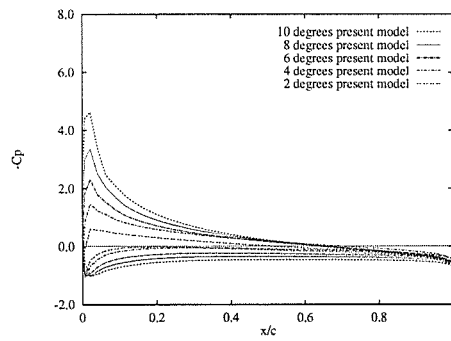


(a) NACA0012

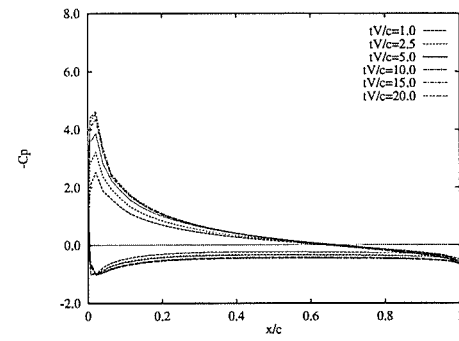


(b) NACA0015

Figure 4.1: Correlation of normal force coefficients with experimental data

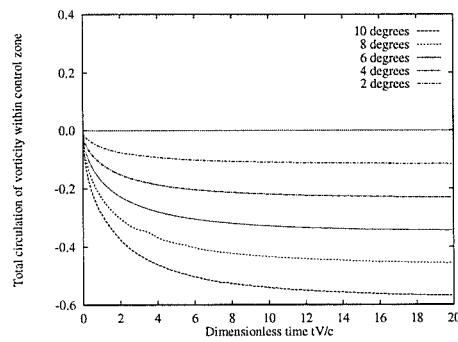


(a) At various incidences, $tV/c = 20$

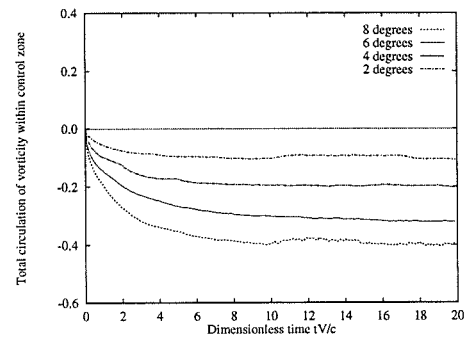


(b) At various time steps, $\alpha = 10^\circ$

Figure 4.2: Pressure distributions for the NACA0012



(a) NACA0012



(b) NACA0015

Figure 4.3: Circulation history, $Re = 990,000$

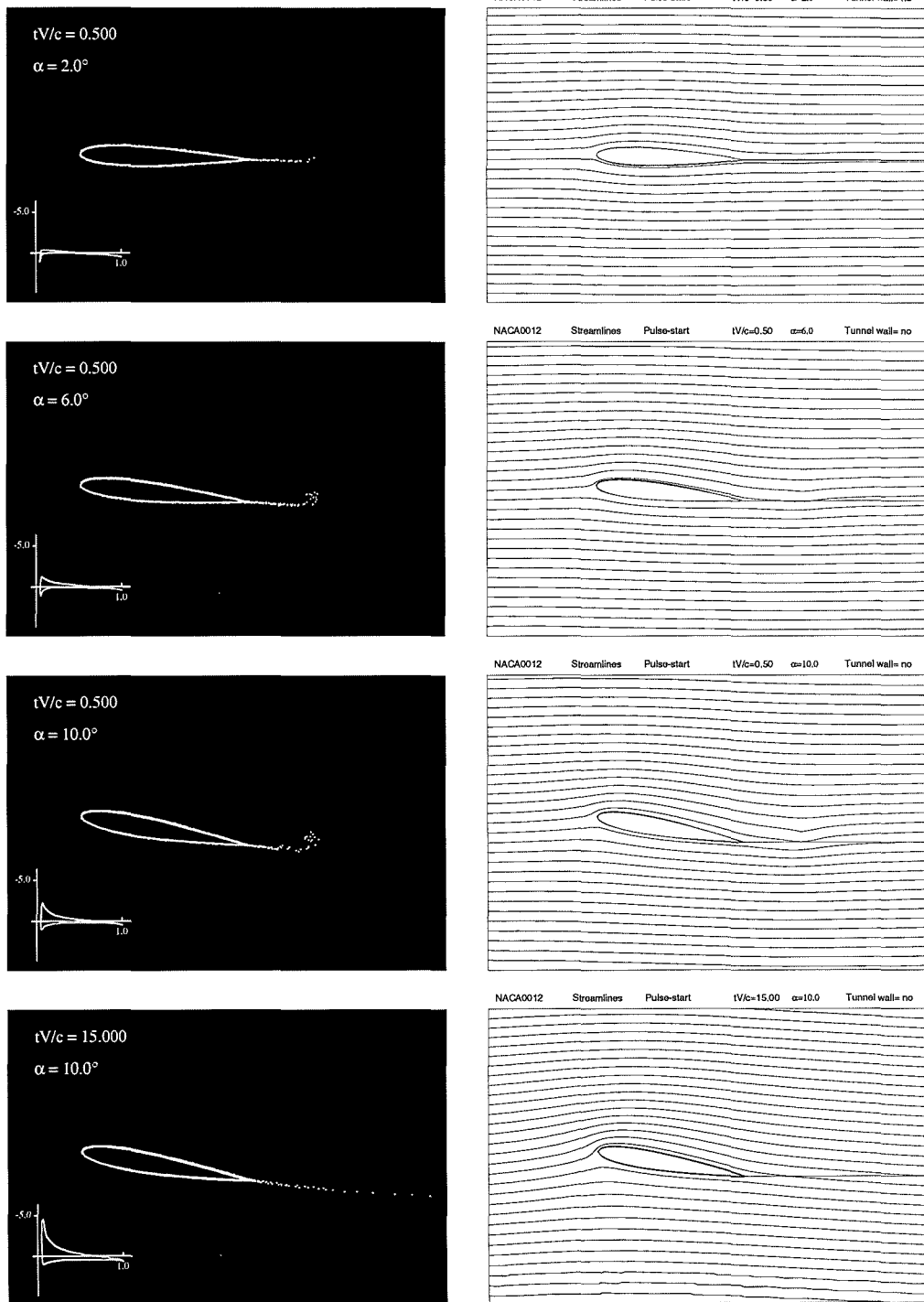


Figure 4.4: Vortex patterns and streamlines for impulsively started flow around the NACA0012

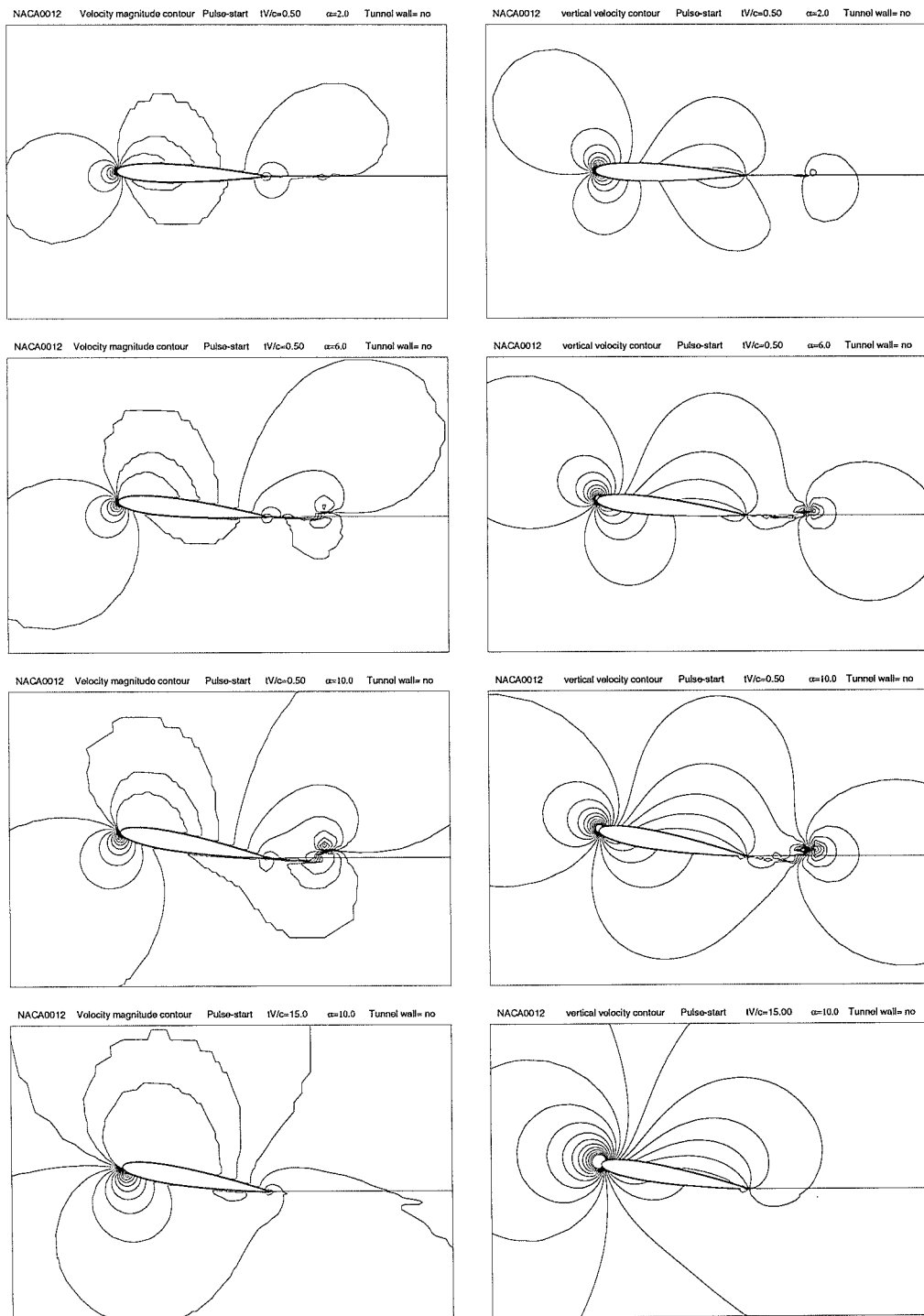


Figure 4.5: Contours of velocity magnitude and vertical velocity for impulsively started flow around the NACA0012

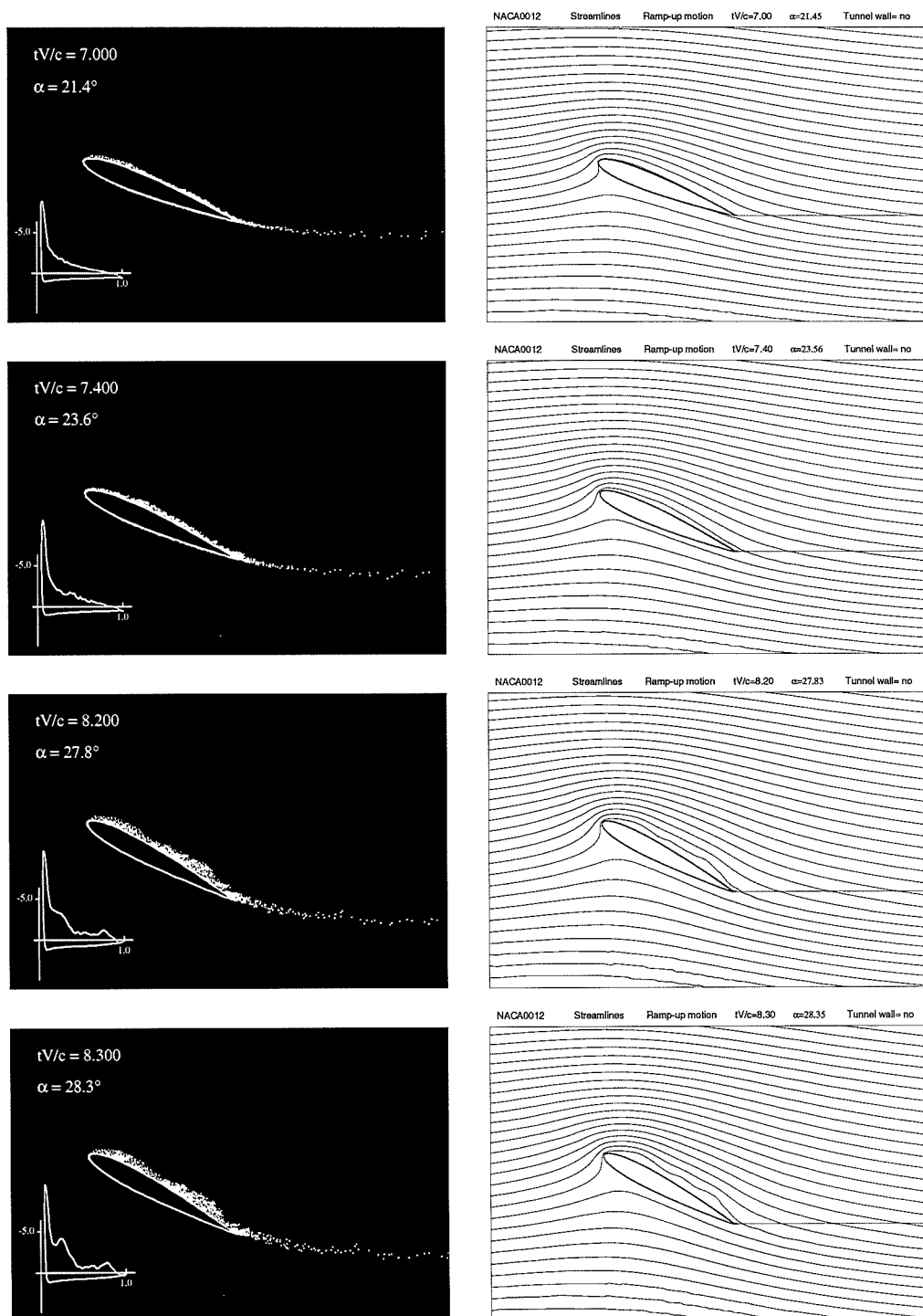


Figure 4.6: Vortex patterns and streamlines for the NACA0012 in ramp-up, $\kappa = 0.0415$

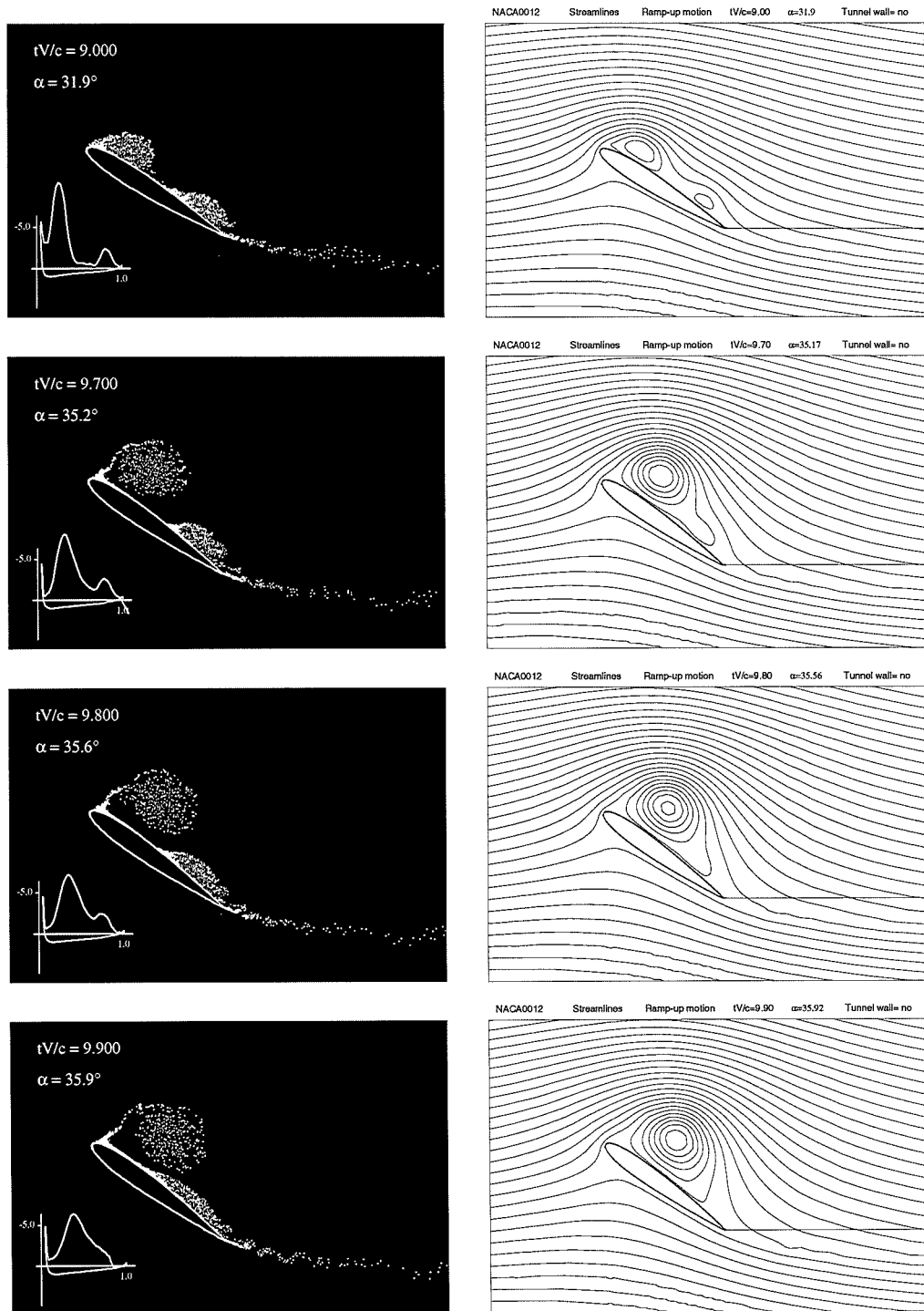


Figure 4.6: (Continued)

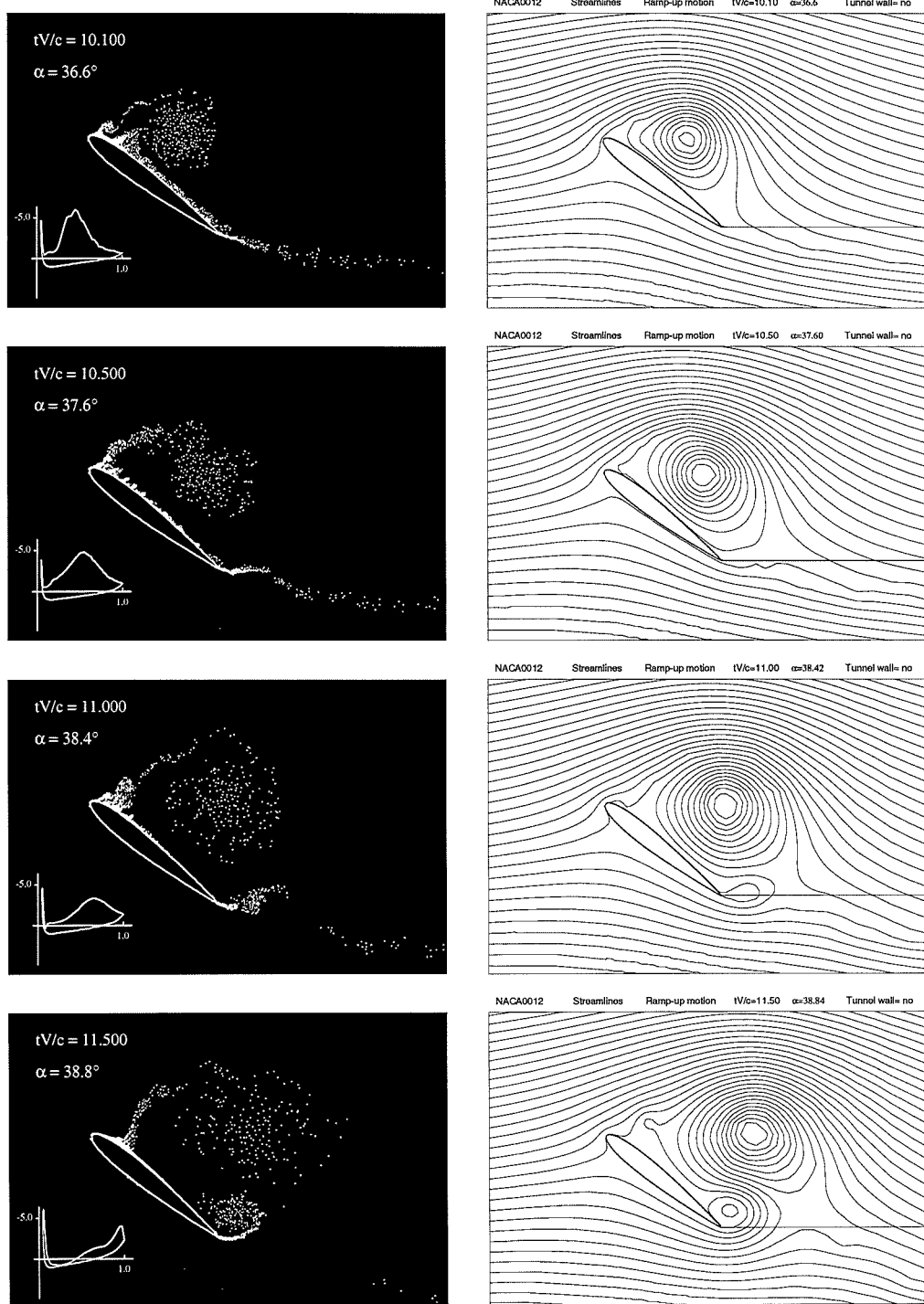


Figure 4.6: (Continued)

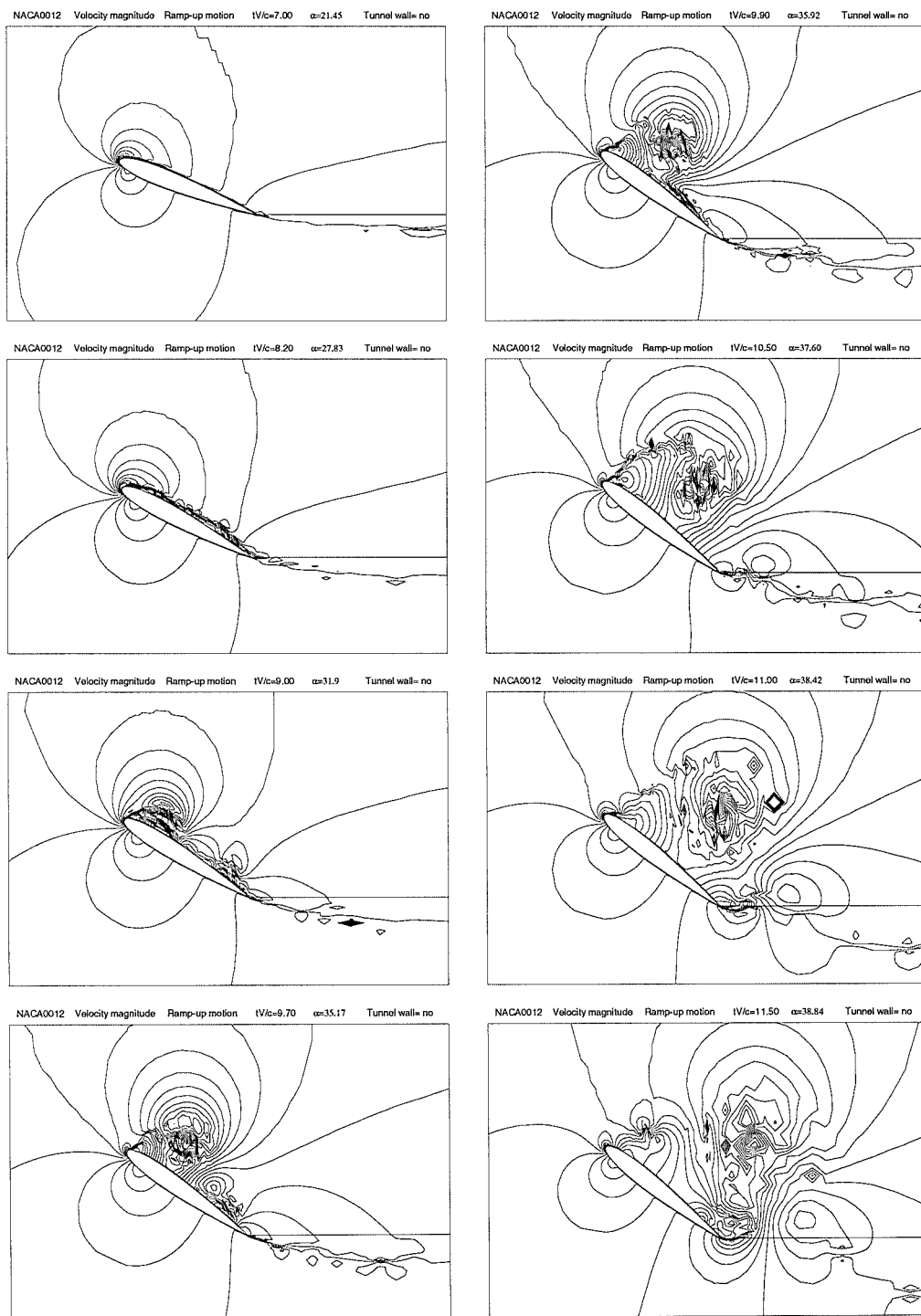


Figure 4.7: Velocity magnitude contours for the NACA0012 in ramp-up, $\kappa = 0.0415$

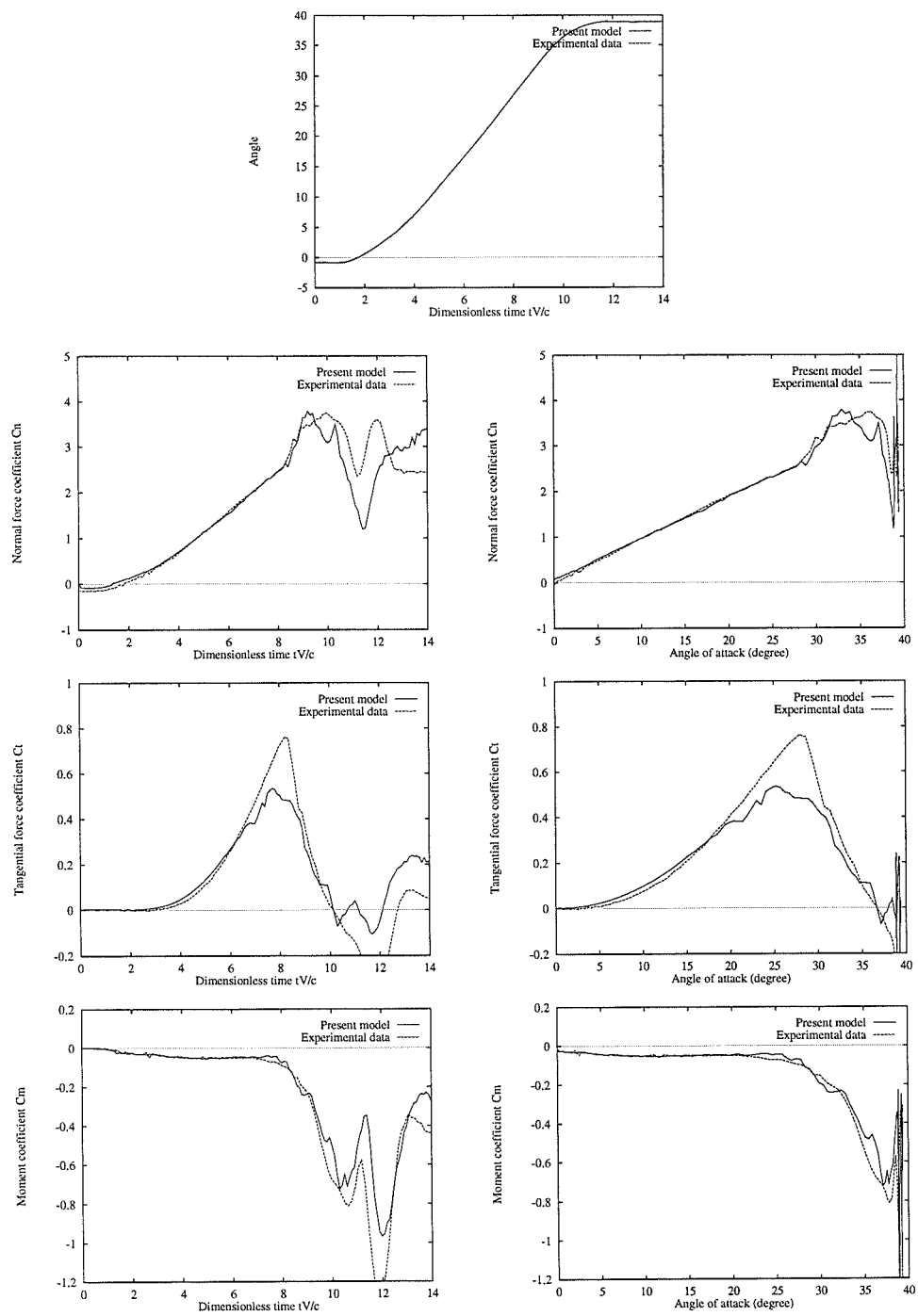


Figure 4.8: Characteristics for the NACA0012 in ramp-up, $\kappa = 0.0415$

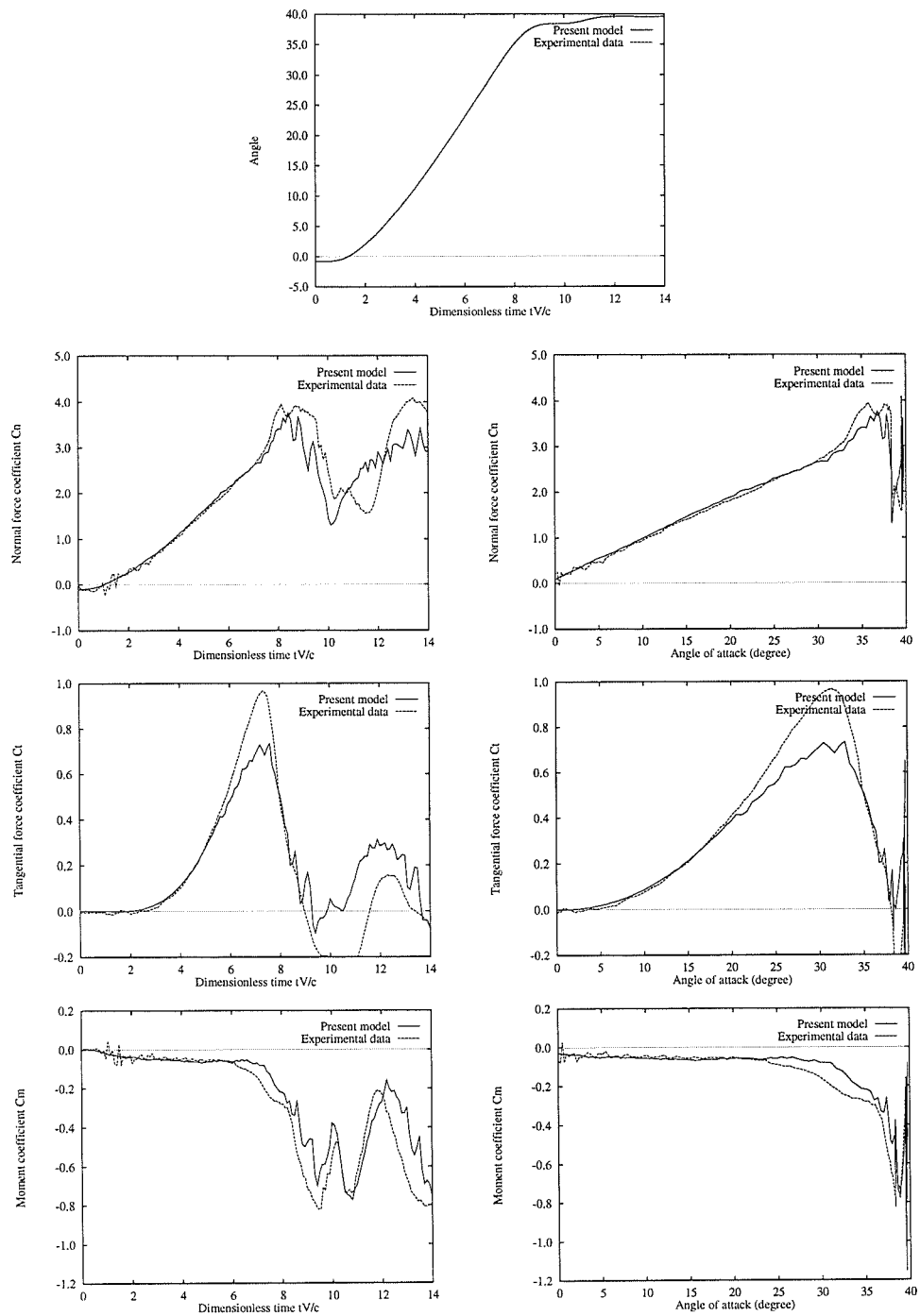


Figure 4.9: Characteristics for the NACA0015 in ramp-up, $\kappa = 0.0487$

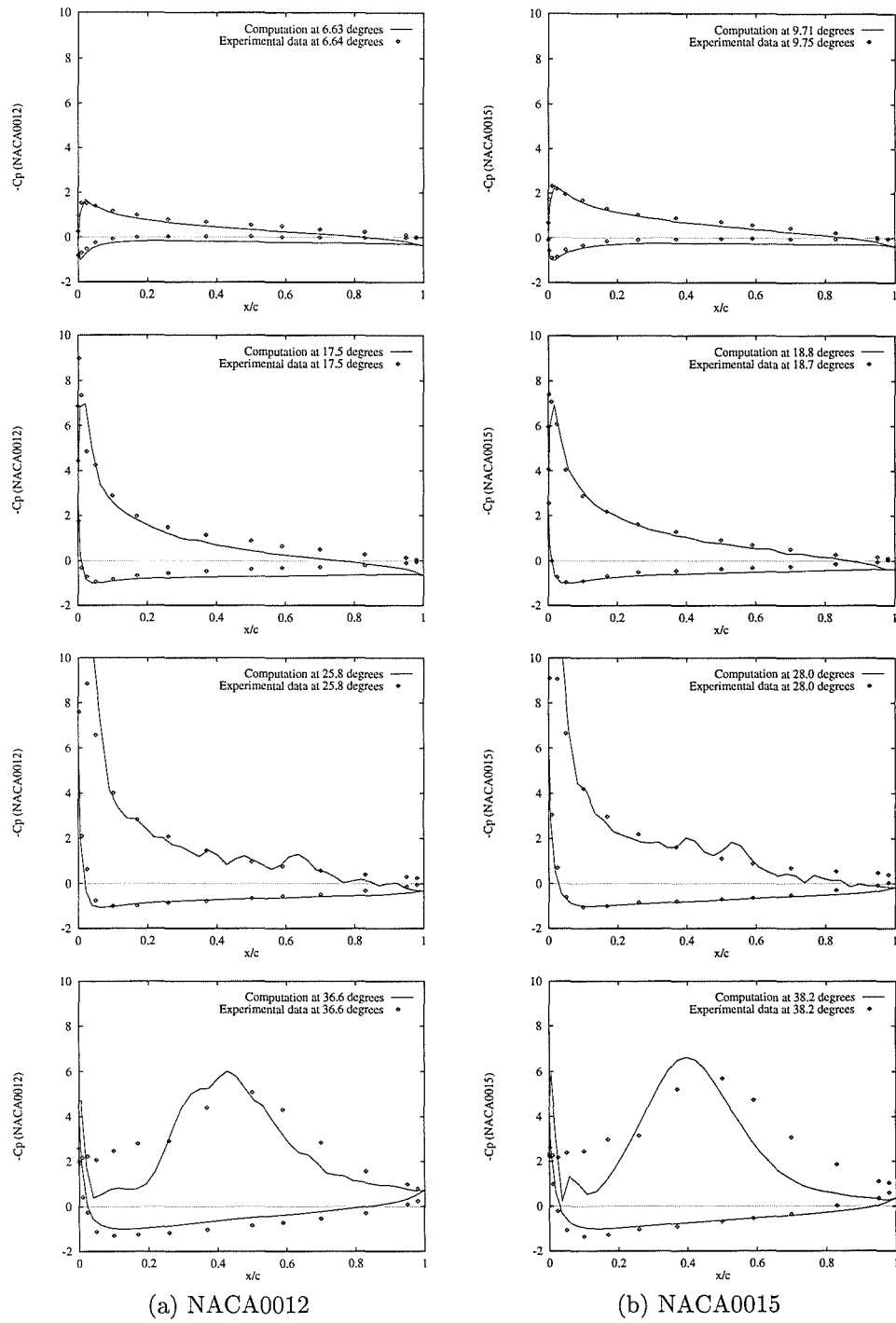


Figure 4.10: Pressure distributions for the NACA0012 and NACA0015 in ramp-up

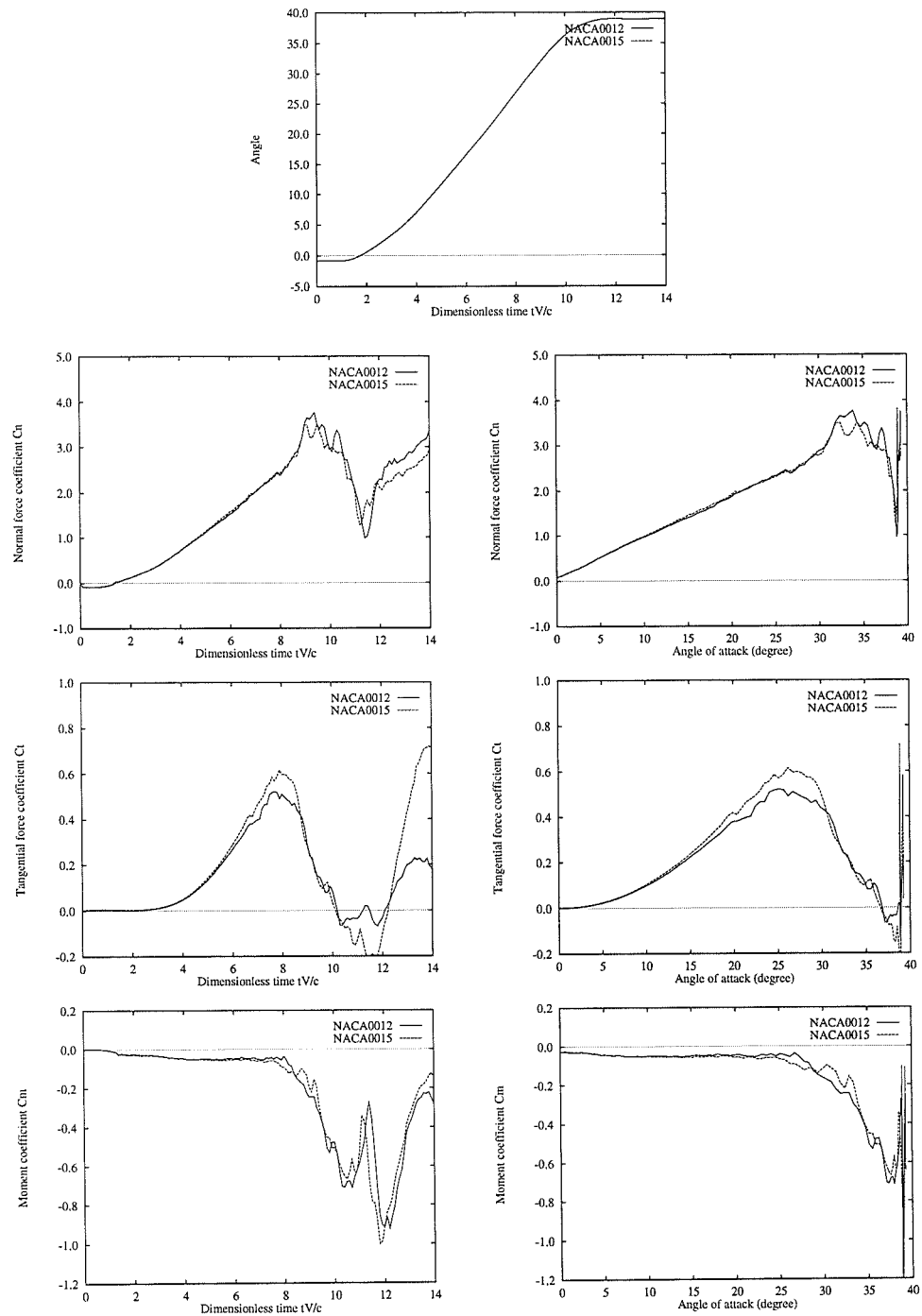


Figure 4.11: Comparison of characteristics between the NACA0012 and NACA0015, $\kappa = 0.0415$

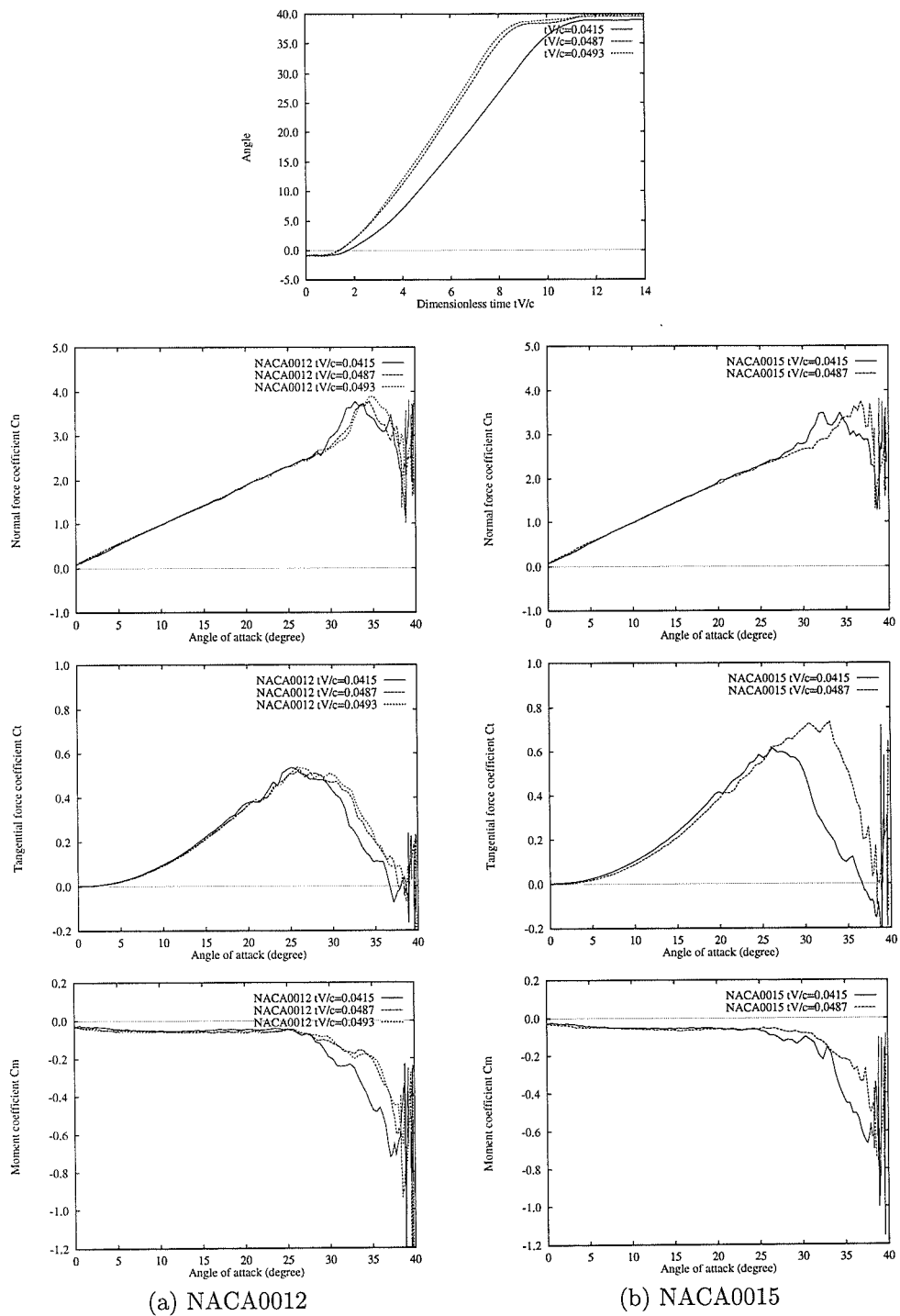


Figure 4.12: Comparison of characteristics between various pitch rates

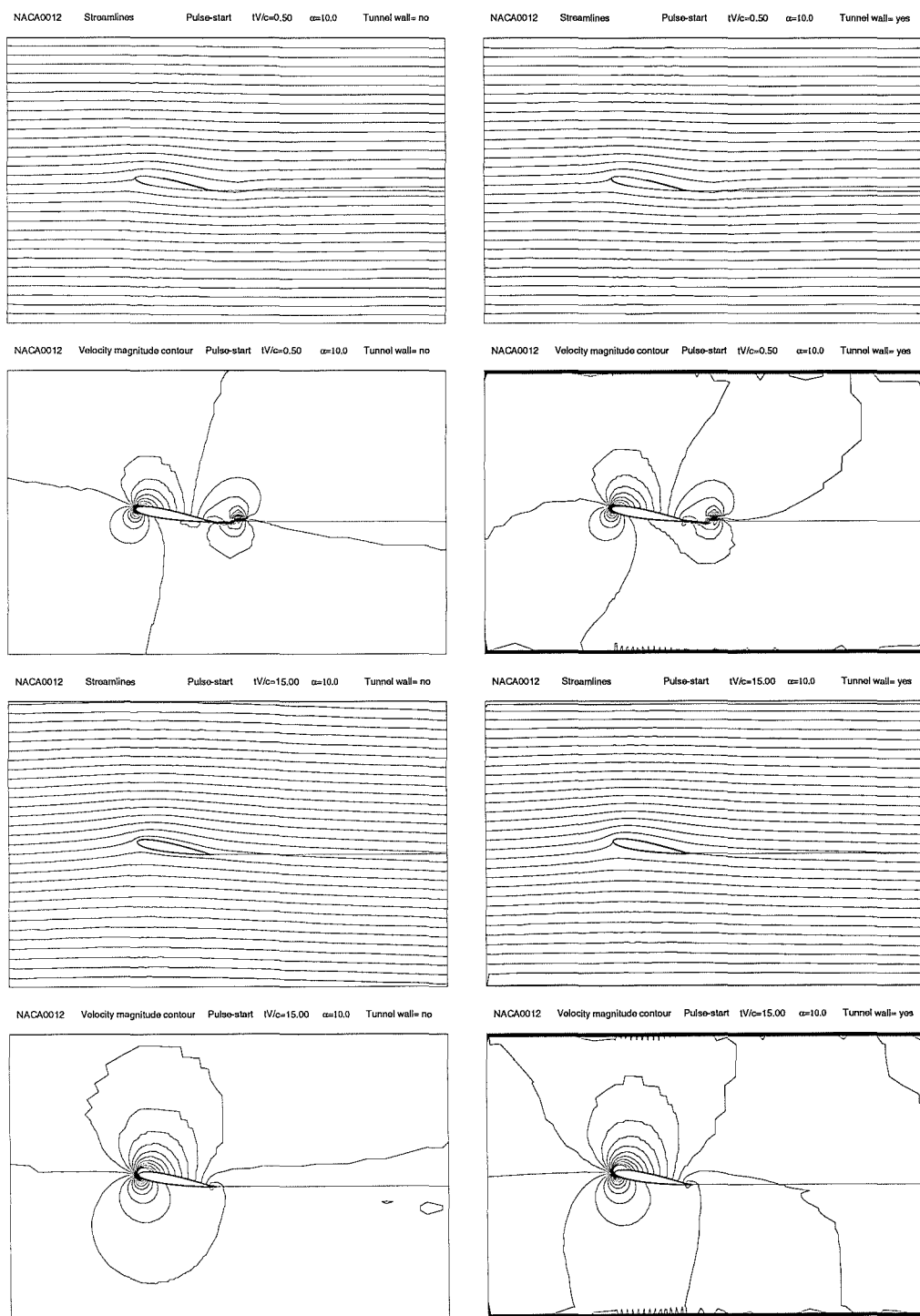


Figure 4.13: Tunnel wall effects for impulsively started flow around the NACA0012

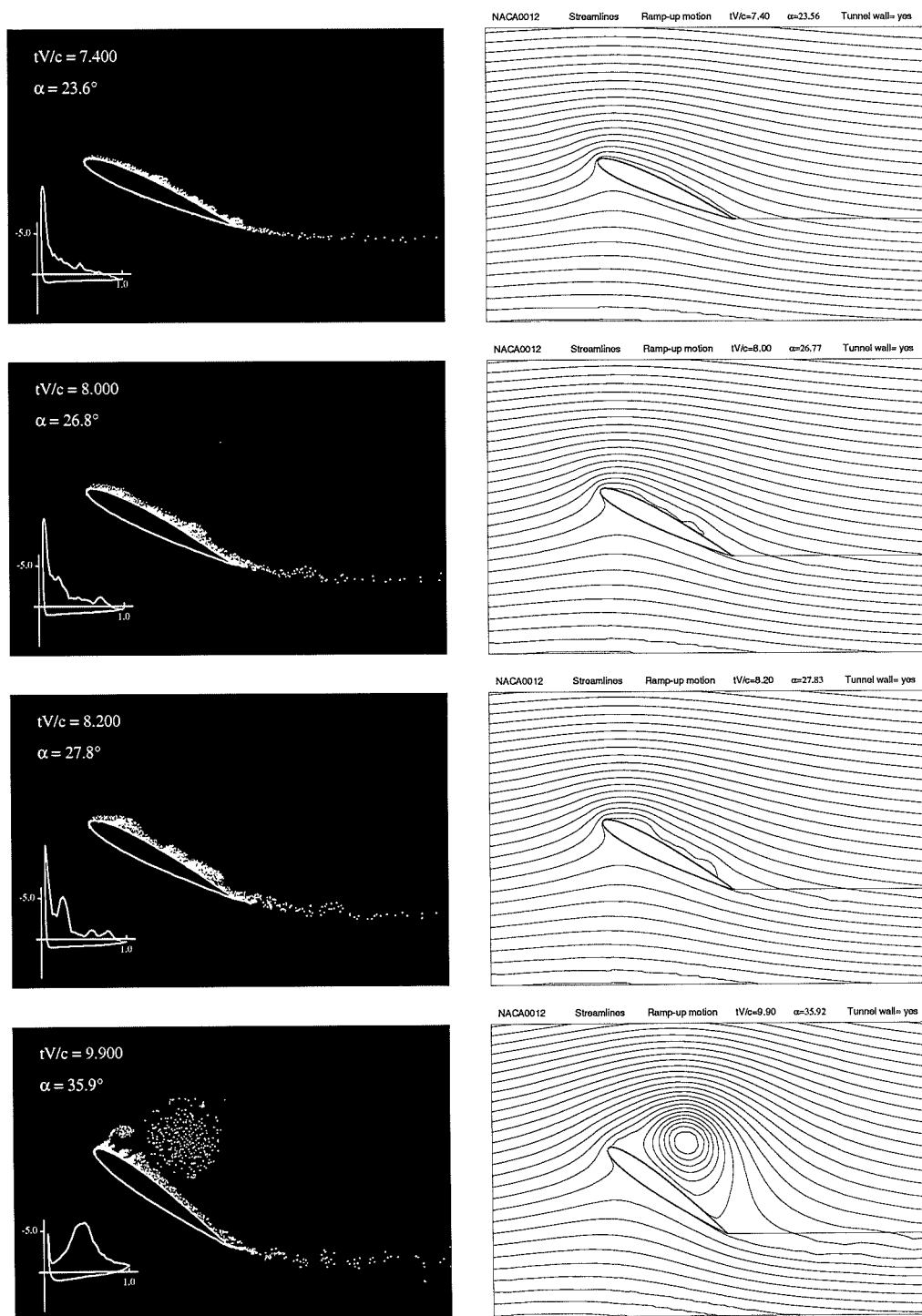


Figure 4.14: Vortex patterns and streamlines for the NACA0012 in ramp-up with wall effect

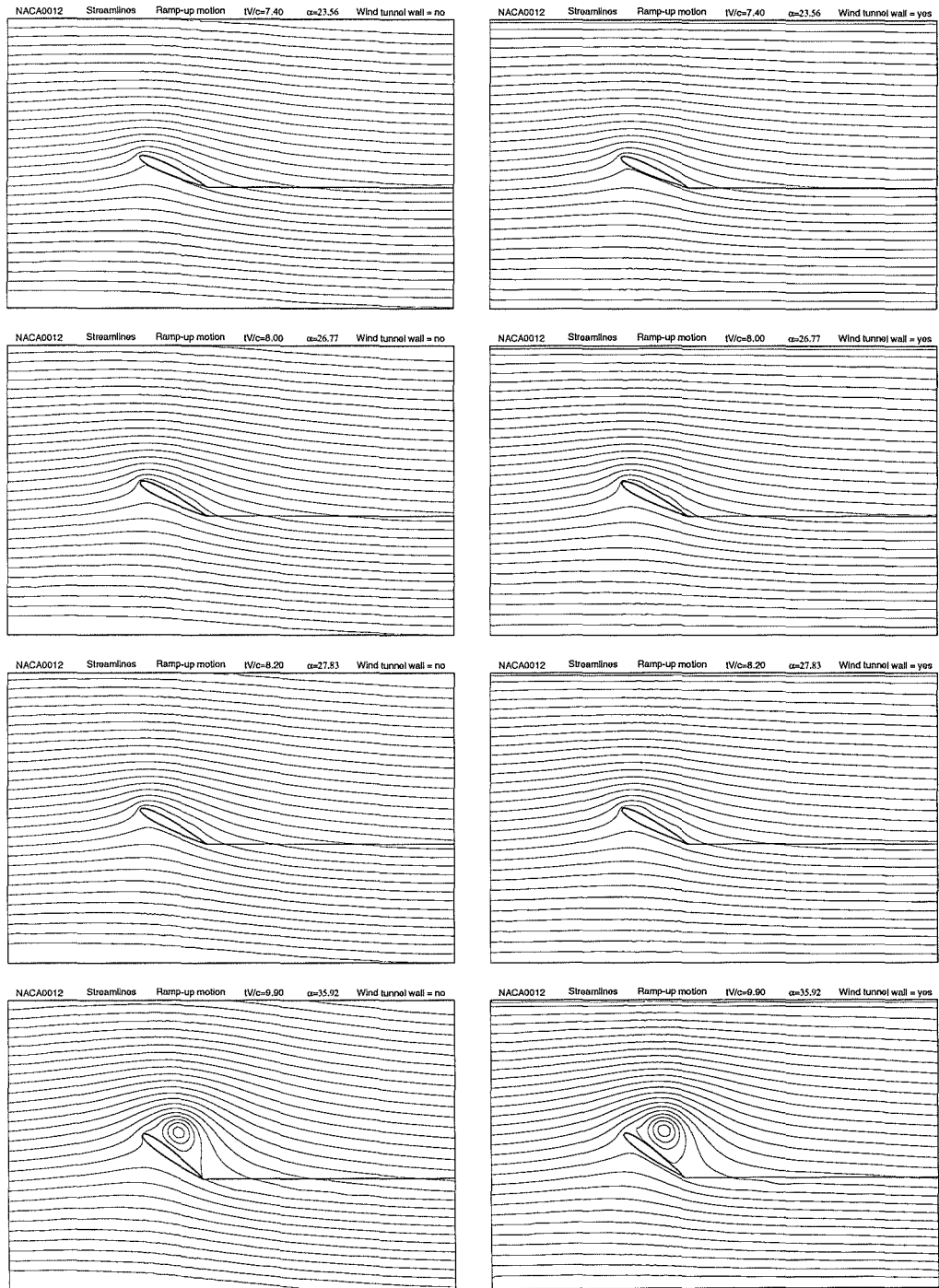


Figure 4.15: Comparison of NACA0012 streamlines with and without wall effect

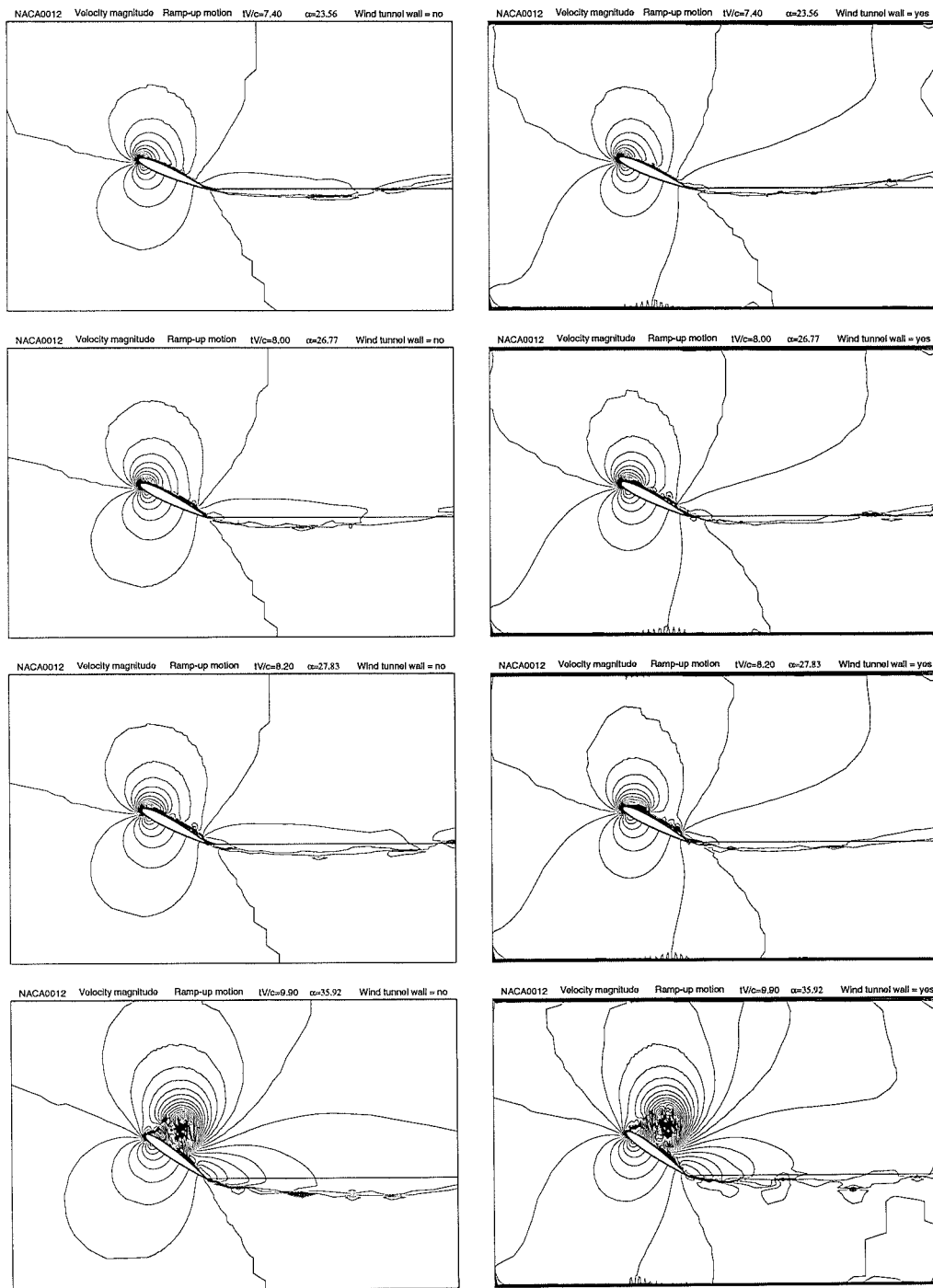


Figure 4.16: Comparison of NACA0012 velocity magnitude contours with and without wall effect

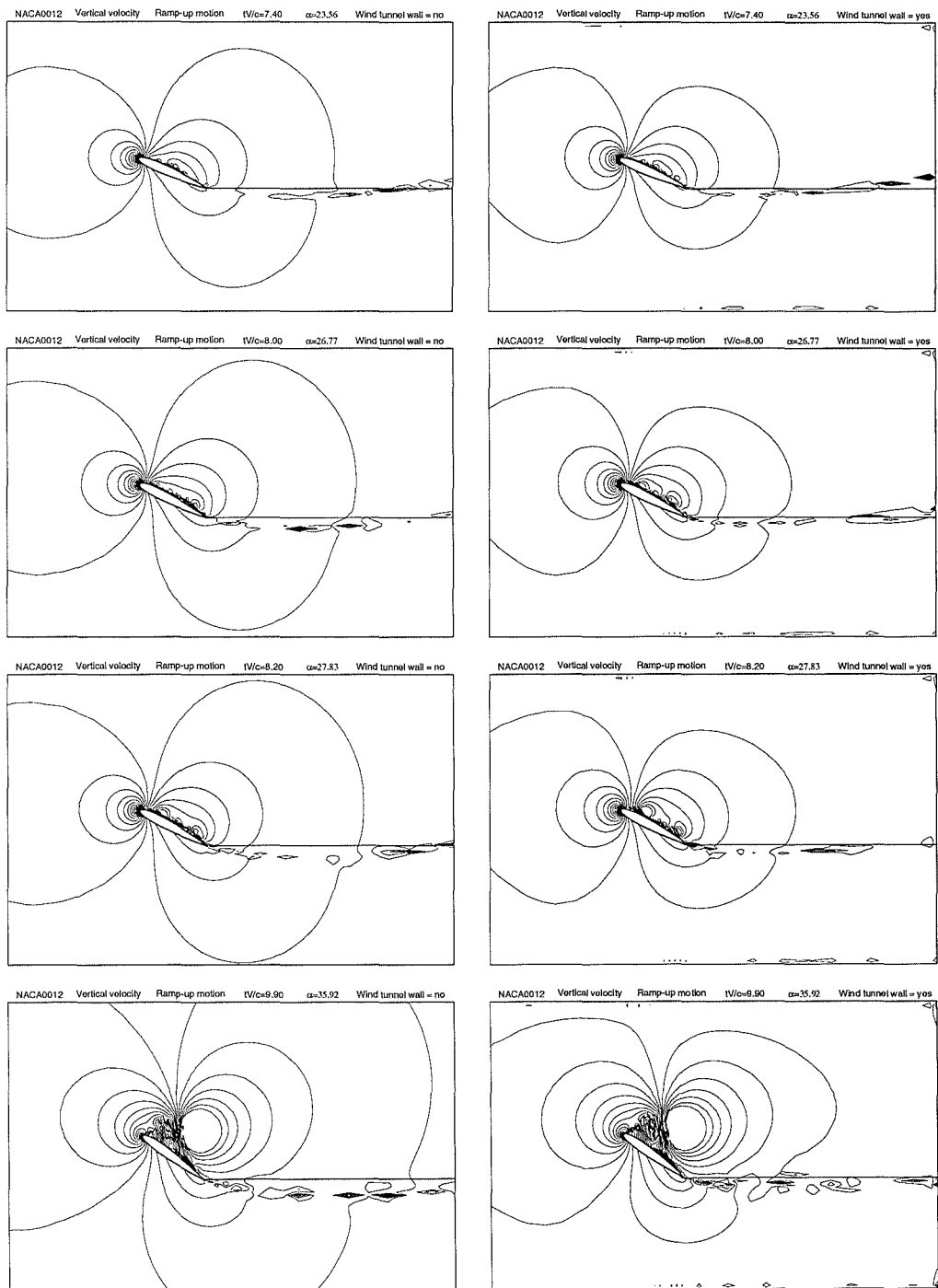


Figure 4.17: Comparison of vertical velocity contours with and without wall effect

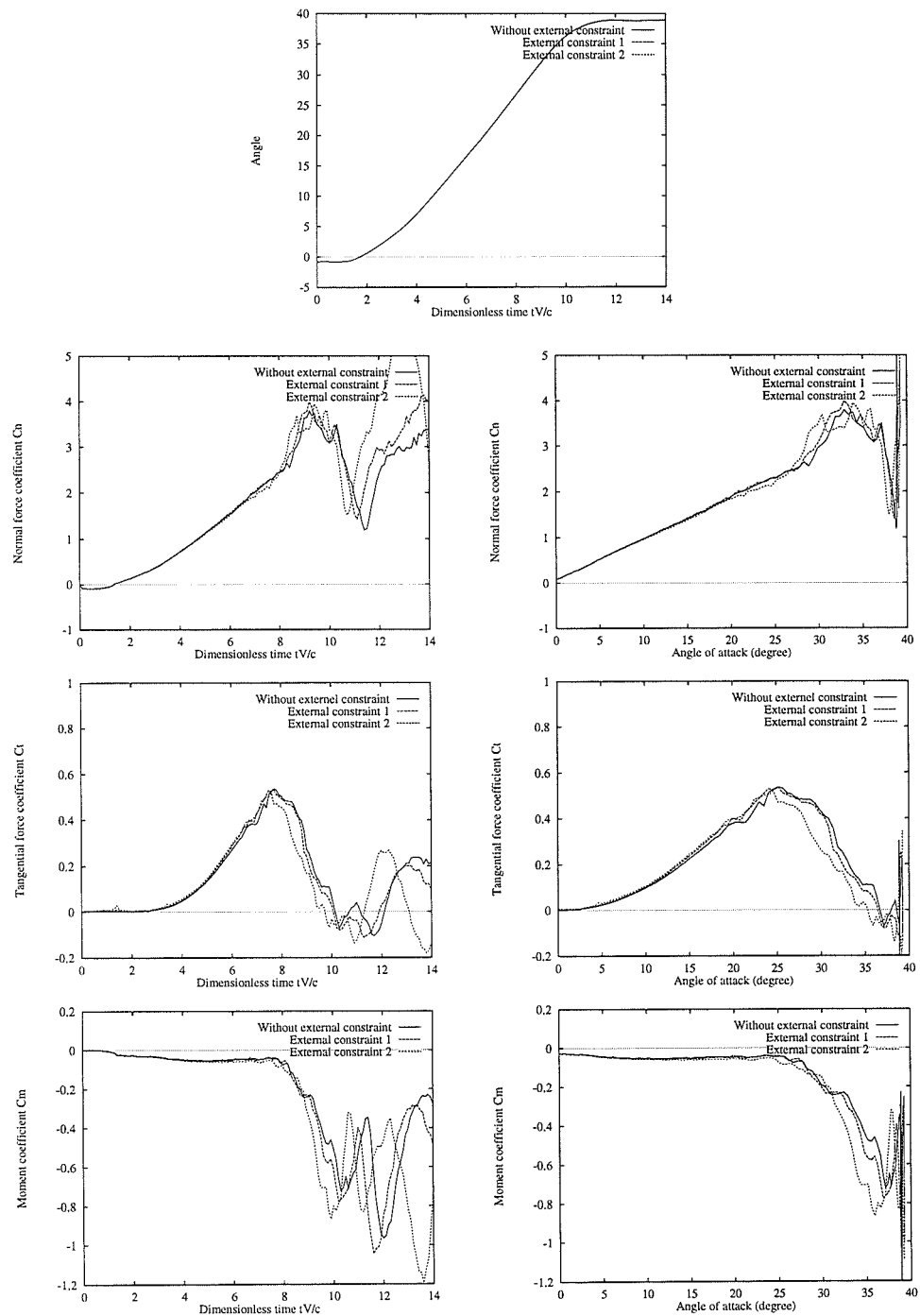


Figure 4.18: Influence of wall effects on characteristics for the NACA0012 in ramp-up, $\kappa = 0.0415$

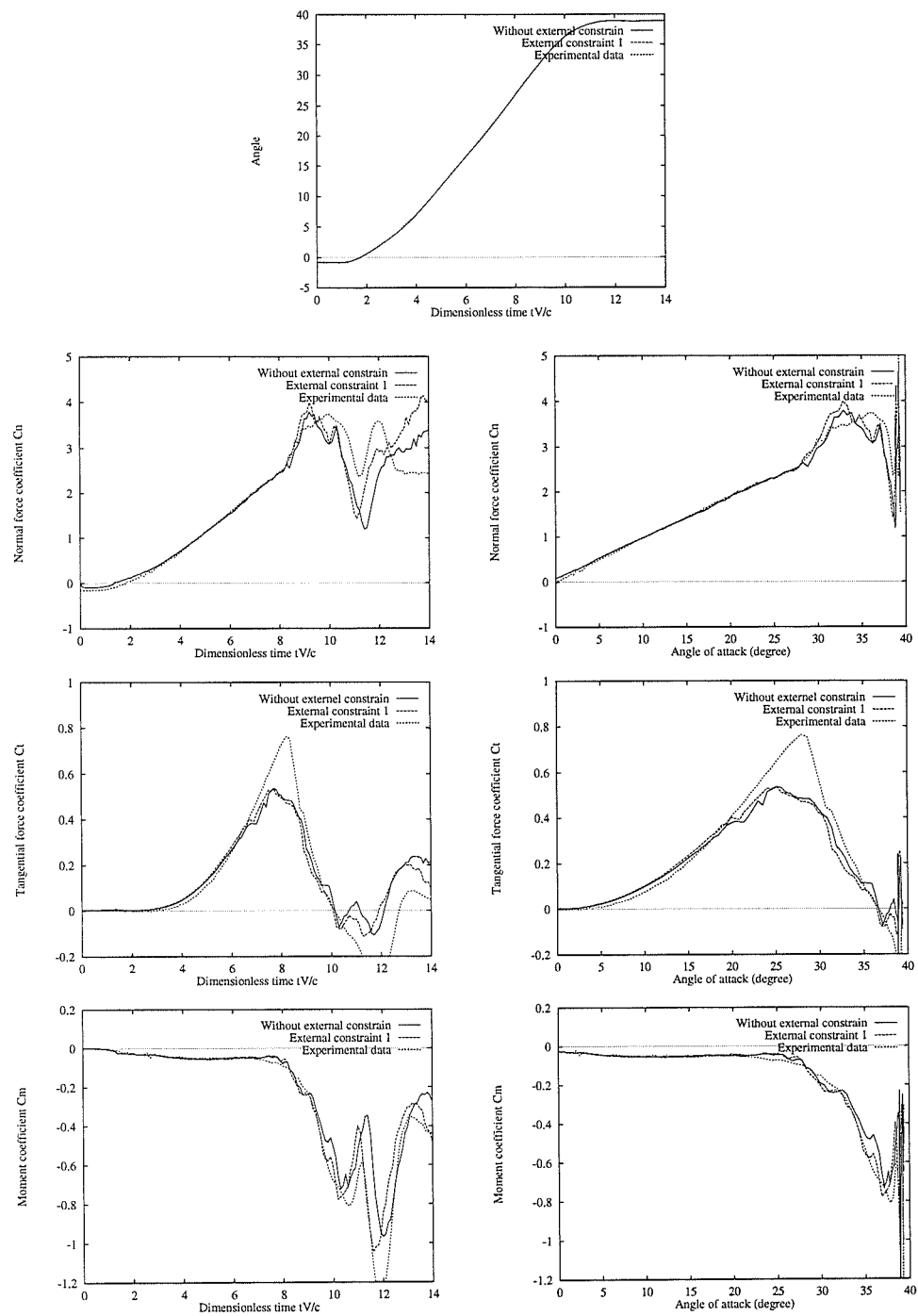


Figure 4.19: Correlation of characteristics for the NACA0012 in ramp-up with wall effect

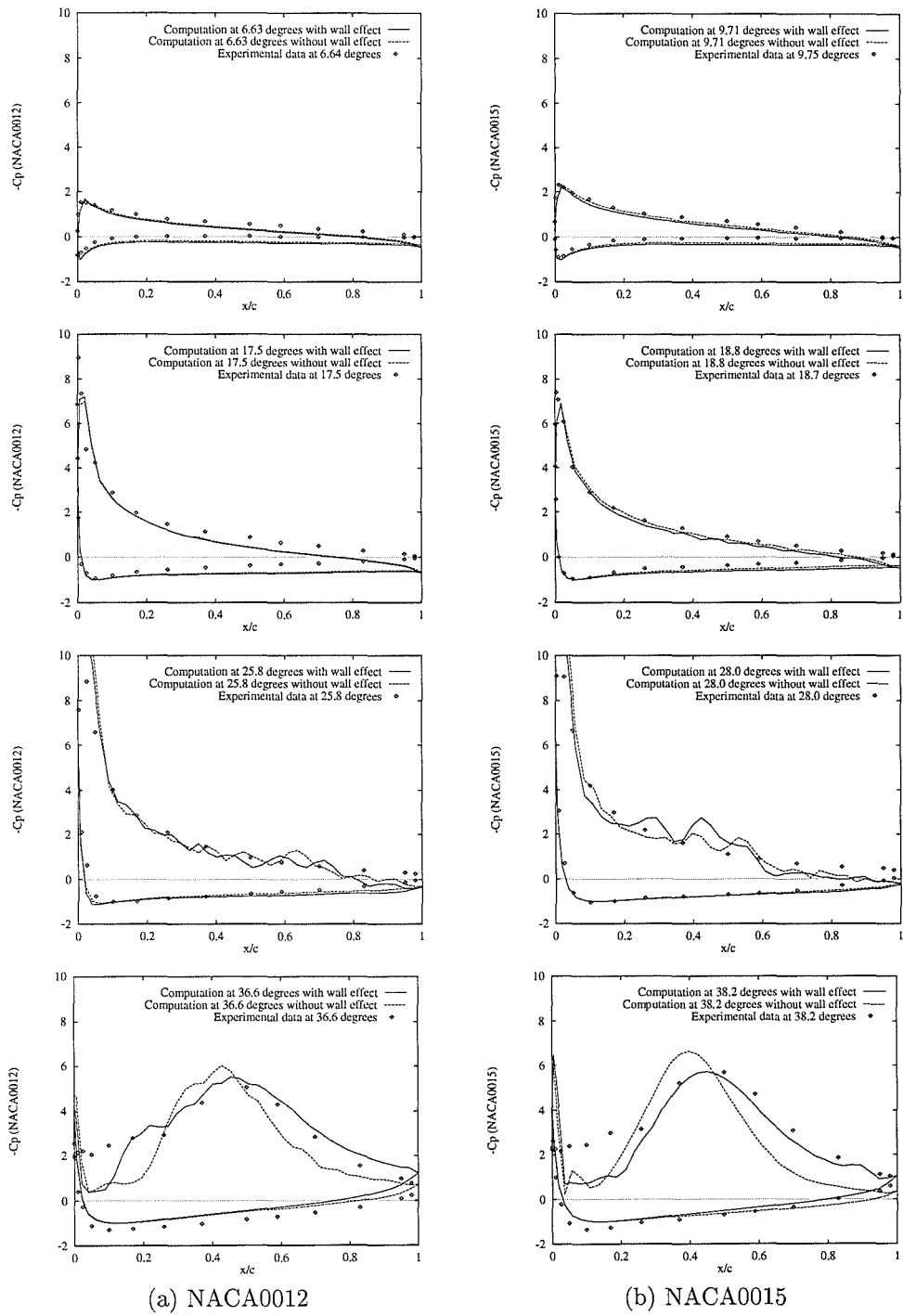


Figure 4.20: Pressure distributions with and without tunnel wall effect

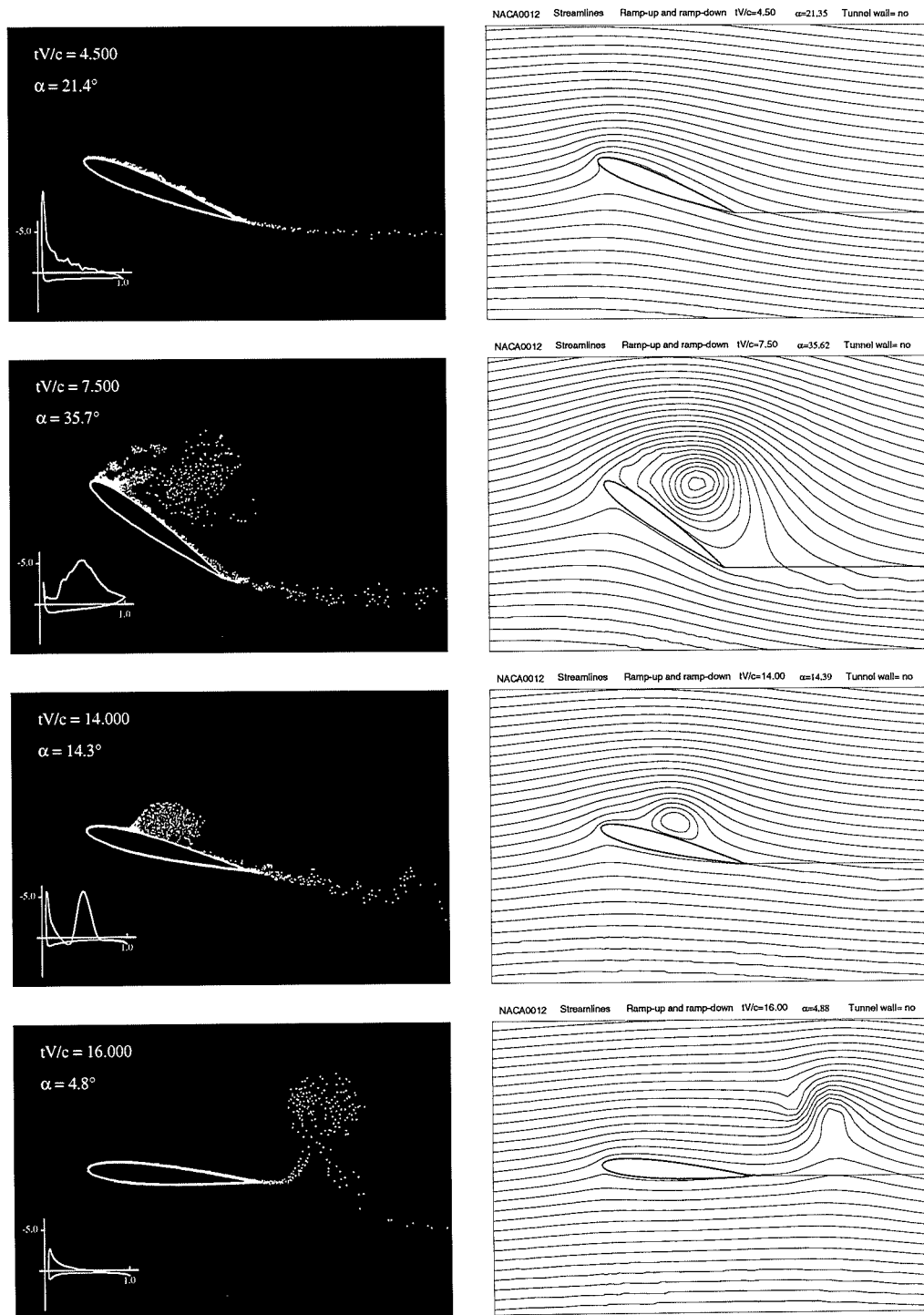


Figure 4.21: Vortex patterns and streamlines for the NACA0012 in ramp-up and ramp-down, $\kappa = 0.0415$

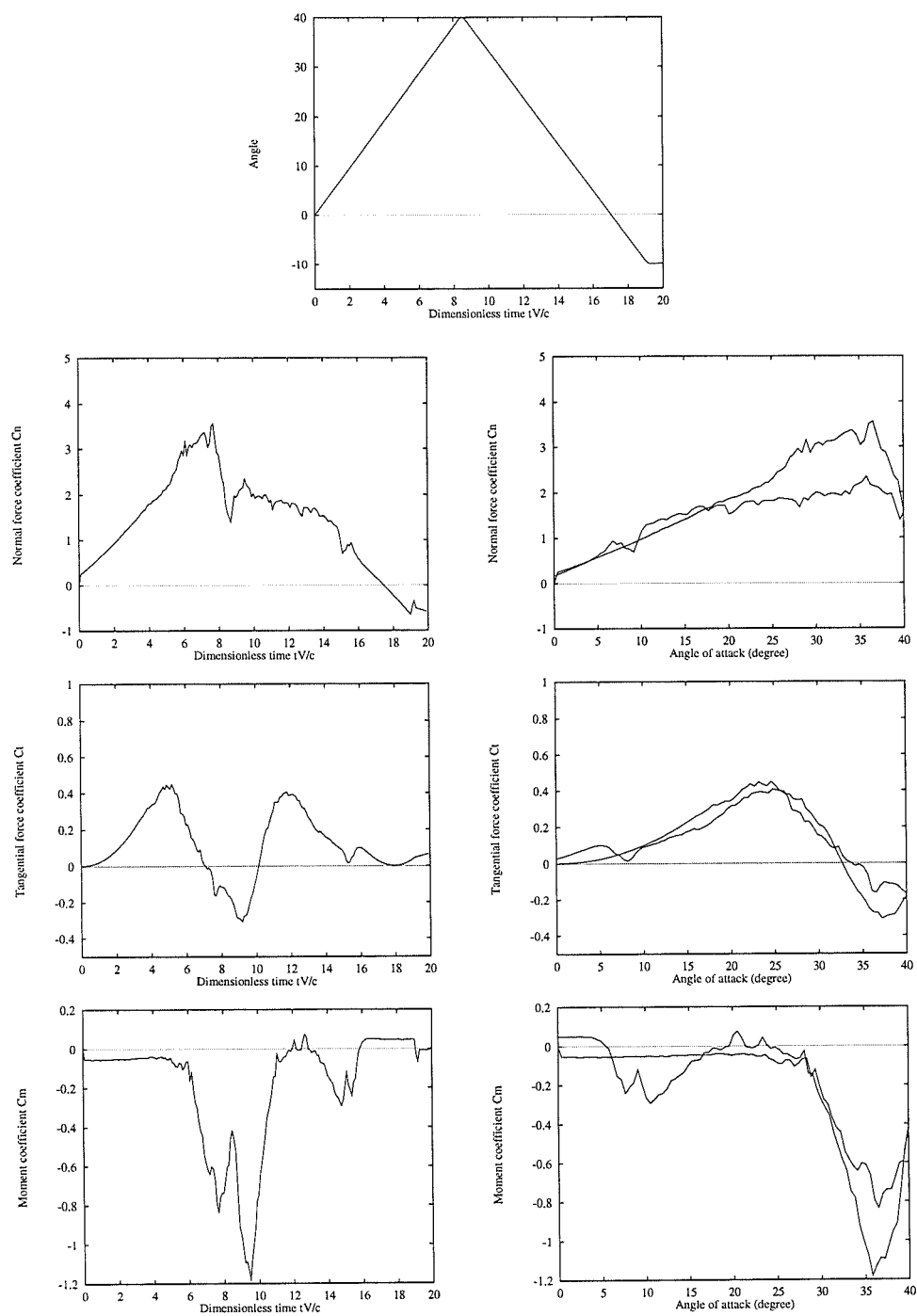


Figure 4.22: Characteristics for the NACA0012 in ramp-up and ramp-down, $\kappa = 0.0415$

Chapter 5

CONCLUDING REMARKS

This chapter presents concluding remarks with regard to the development and application of the vortex method described in the previous chapters. The remarks are split into two sections: a summary section, in which the main contributions of the research presented in this thesis are outlined; a section suggesting areas in which further improvements in the capabilities of the method could be achieved.

5.1 *Summary*

- A vortex method has been developed for simulating unsteady flows around pitching aerofoils. The capabilities of the model have been demonstrated through the prediction of both separated flows and attached flows. In particular, the structure of the flow around an aerofoil undergoing dynamic stall is well captured by the model without the need for other means to predetermine separation points. In contrast to many other vortex methods, the model can provide both qualitative and detailed quantitative information. Throughout a wide range of incidence, for the test cases considered, the predicted pressure distributions are smooth and the normal force and pitching moment are in good agreement with experimental data.
- The model has been developed to include flow around an aerofoil in the presence of external constraints. Of particular interest is the flow past a pitching aerofoil in a wind tunnel, for which the method has demonstrated an ability to predict the wall effects. Since most experimental data from dynamic stall tests are not subject to wind tunnel wall correction, the capability to model wall effects is of practical importance in the validation of numerical models and in gaining a

proper understanding of aerofoil behaviour. The predicted flow structures and quantitative results produced by the model are consistent with those expected.

- Both theoretical and numerical progress has been made in the research. Theoretically, a velocity expression has been derived for flows with both a moving inner boundary and fixed external constraints. To maintain both the no penetration and no slip conditions, it is concluded that constraints parallel to the free stream velocity can be modelled by placement of a constant vortex sheet at the boundary and the introduction of distributed vortices next to the constraints to represent vorticity creation on the surface. The strength of the vortex sheet is equivalent to the free stream velocity, while the strength of the vortices can be calculated in the same manner as for an internal boundary. This approach has the advantage of representing directly the developing boundary layer on the external surfaces, avoiding the necessity of employing mirror vortices and iteration techniques, incorporated into more traditional models.
- For the computation of surface pressure distribution, an equation has been derived relating the pressure gradient to the rate of vorticity creation on the surface. The relation was originally proved for a fixed boundary only but the validity of the conclusion is now extended in this thesis to a moving boundary, such as the surface of a moving aerofoil.
- Numerically, substantial improvements have been made in the modelling of the vorticity close to the surface. These include representation of high curvature surfaces, better discretization of vorticity, better simulation of the vorticity diffusion process and more accurate implementation of boundary conditions.
- With regard to surface representation, a sub-panel model was proposed to provide a more accurate polygonal representation of the body surface, as well as to facilitate a more straightforward vorticity discretization scheme.

- In the description of vorticity, the concept of two zone vorticity discretization is employed to represent the real vorticity field. The zones are divided into the creation zone, for the thin strip close to the boundary, and the wake zone containing the remaining vorticity. As for most vortex methods, vortices in the wake zone are tracked in a Lagrangian manner, in conjunction with the random walk method. However, vorticity in the creation zone is re-discretized every time step at predetermined points, with the strength obtained by implementing the boundary conditions. These latter vortices are considered to be a discretized representation of the vortex sheet which envelops the surface. The piecewise linear variation in the circulation density of this sheet necessitates the use of multiple vortices on each panel. This arrangement is advantageous, however, for two main reasons: the number of vortices on each panel does not affect the size of the system matrix, which depends on the number of panels only; increasing the number of vortices per panel improves the quality of the solution.
- A surface vortex shedding model has been proposed to simulate the exchange of vorticity across the interface between the two discretization zones. The model contrasts with the traditional vortex shedding from a sharp edge or predetermined points. The convection and diffusion of vorticity are reflected in the model via appropriate displacements of the vortices at each time step. The transport equations for the vortices are an approximation to the continuous equations. Since the accuracy deteriorates when the vortices are of large circulation, the surface vortex shedding model alleviates this difficulty by employing many vortices of smaller circulation.
- The assumption that the vortex sheet strength γ is continuous on a smooth surface may not be as reasonable at a sharp edge such as an aerofoil trailing edge. This distinctive feature is represented by de-coupling the vorticity strength, γ , for each panel connected to the point. In addition, the vorticity shed from the

upper and lower surfaces at the trailing edge, into a small zone immediately downstream, is re-discretized in a manner which reflects the combined vorticity of the two vortex streams.

Some standard techniques associated with vortex methods have also been implemented into the model. These include the use of vortex blobs to avoid singularities, the random vortex method for simulating viscous diffusion, a vortex merging scheme to reduce computational cost and the Adams-Bashforth second order method for vortex convection. The combination of these standard techniques with the new modelling features summarised above has led to improvements in the simulation of unsteady flows about pitching aerofoils.

5.2 Further developments

The vortex method presented in this thesis has provided encouraging results in the simulation of flows around pitching aerofoils. It is possible that the model, with the proposed new techniques, could be further developed to predict other flows, for example flows around bluff bodies, three dimensional flows. To improve the efficiency and accuracy of the model, the following modifications are suggested.

1. Implementation of a fast method to compute the vortex velocities. In a vortex method, most of the CPU time is consumed in the computation of the interaction between vortices during the velocity computation. In the current model, only the amalgamation process provides a reduction in computation time. This is due mainly to the fact that the computational speed is not prohibitive for the computation of flows around pitching aerofoils since, at most instances of time, the flow remains attached and therefore the total number of vortices is not great. The situation would be different for bluff body flow simulation or for three dimensional flow computation, in which cases the benefit of a fast algorithm would then be more attract-

ive. Existing algorithms include vortex-in-cloud, multipole decomposition, zonal decomposition, parallel computation and many others.

2. Improvement in leading edge modelling. The current model has predicted spiky pressure distributions at the leading edge, which may be due to the inadequacy of the current linear distribution of panel vorticity in this region. Special treatment may be required for this high curvature surface segment, including modifications to both the circulation distribution and the vortex shedding model.
3. Incorporation of a turbulence model. No explicit account of turbulence is included in the model although it is possible that the chaos caused by the vortices near the boundary may have some resemblance to the effects of turbulence. However, this effect is greatly reduced as the vortices are transported farther away from the body into the wake, and is compounded by vortex merging. The small scale turbulence could then only be accounted for by implementing an appropriate model.
4. Development of relationships between the numerical parameters and physical properties. Most vortex methods involve some degree of empiricism in the specification of some numerical parameters, and the current model is no exception. In order to remove a certain amount of arbitrariness in the values employed for these parameters there is a need to establish a more general process for identifying these values.

In conclusion, the current model has demonstrated its capability in simulating flows around pitching aerofoils. As might be expected, a number of improvements which could be made to the model have been identified which will further increase its modelling capability.

REFERENCES

- [1] B.W. McCormick. *Aerodynamics, Aeronautics and Flight Mechanics*. Wiley, 1995.
- [2] I.H. Abbott and A.E. van Doenhoff. *Theory of Wing Sections*. Dover Publications, Inc, 1959.
- [3] C.D. Harris. Two-dimensional aerodynamic characteristics of the NACA0012 airfoil in the langley 8-foot transonic pressure tunnel. *NASA TM-81927*, April 1981.
- [4] S. Ahmed and M.S. Chandrasekhara. Reattachment studies of an oscillating airfoil dynamic stall flowfield. *AIAA Journal*, 32(5):1006–1012, May 1994.
- [5] R.K. Angell, P.J. Musgrove, and R.A.McD. Galbraith. Collected data for tests on a NACA 0015 aerofoil. volume I: Pressure data from ramp function tests. *G.U. AERO report 8803*, 1988.
- [6] S. Aso and M. Hayashi. Experimental and computational studies on dynamic stall in low speed flows. In *Proceedings of the IUTAM Symposium on Fluid Dynamics of High Angle of Attack*, 1993.
- [7] L.W. Carr and M.S. Chandrasekhara. Study of compressibility effects on dynamic stall of rapidly pitching airfoils. *Computer Physics Communications*, 65(1-3), April 1991.
- [8] L.W. Carr. Progress in analysis and prediction of dynamic stall. *Journal of Aircraft*, 25(1), January 1988.

- [9] L.W. Carr and M.S. Chandrasekhara. Compressibility effects on dynamic stall. *Progress in Aerospace Science*, 32(6):523–573, December 1996.
- [10] L.W. Carr, K.W. McAlister, and W.J. McCroskey. Analysis of the development of dynamic stall based on oscillating airfoil experiments. *NASA TN D-8382*, 1977.
- [11] L.W. Carr and W.J. McCroskey. Review of recent advances in computational and experimental analysis of dynamic stall. *Proceedings of the IUTAM Symposium on Fluid Dynamics of High Angle of Attack*, 1993.
- [12] M.S. Chandrasekhara and S. Ahmed. Laser velocimetry measurements of oscillating airfoil dynamic stall flow field. *AIAA Journal*, 32(5):1006–1012, 1994.
- [13] J.M. Currier and K.Y. Fung. Analysis of the onset of dynamic stall. *AIAA Journal*, 30(10), October 1992.
- [14] L.E. Ericsson. Dynamic airfoil flow separation and reattachment. *Journal of Aircraft*, 32(6):1191–1197, 1995.
- [15] L.E. Ericsson and J.P. Reding. Dynamic stall at high frequency and large amplitude. *Journal of Aircraft*, 17(3):136–142, March 1980.
- [16] R.A.McD. Galbraith, M.W. Gracey, and R. Gilmour. Collected data for tests on a NACA 0012 aerofoil. volume I: Pressure data from ramp function tests. *G.U. AERO report 9207*, February 1992.
- [17] R.A.McD. Galbraith, A.J. Niven, and L.Y. Seto. On the duration of low speed dynamic stall. *Congress of the International Council of the Aeronautical Sciences*, 1, 1986.

- [18] M. Acharya and M.H. Metwally. Unsteady pressure field and vorticity production over a pitching airfoil. *AIAA Journal*, 30(2), February 1992.
- [19] P. Wernert, W. Geissler, M. Raffel, and J. Kompenhans. Experimental and numerical investigation of dynamic stall on a pitching airfoil. *AIAA Journal*, 34(5):982–989, May 1996.
- [20] J.M. Walker, H.E. Helin, and J.H. Strickland. Experimental investigation of an airfoil undergoing large-amplitude pitching motions. *AIAA Journal*, 23(8), August 1985.
- [21] C. Shih, L. Lourenco, L. van Dommelen, and A. Krothapalli. Unsteady flow past an airfoil pitching at a constant rate. *AIAA Journal*, 30(5):1153–1161, May 1992.
- [22] C. Shih, L.M. Lourenco, and A. Krothapalli. Investigation of flow at leading and trailing edges of pitching-up airfoil. *AIAA Journal*, 33(8), August 1995.
- [23] H. Oshima and B.R. Ramaprian. Velocity measurement over a pitching airfoil. *AIAA Journal*, 35(1), January 1997.
- [24] A.J. Niven, R.A.McD. Galbraith, and D.G.F. Herring. Analysis of reattachment during ramp down tests. *Vertica*, 12(2), 1989.
- [25] A.J. Niven and R.A.McD. Galbraith. Experiments on the establishment of fully attached aerofoil flow from the fully stalled condition during ramp-down motions. In *Proceeding of 17th ICAS Congress, Stockholm, Sweden*, September 1990.
- [26] J. Miyakawa, Y. Shimbo, and S. Aso. Numerical and experimental investigation on dynamic stall vortex. In *Transactions of the 12th International Conference on Structural Mechanics in Reactor Technology*, 1993.

- [27] W.J. McCroskey, L.W. Carr, and K.W. McAlister. Dynamic stall experiments on oscillating airfoils. *AIAA Journal*, 14(1):57–63, 1976.
- [28] W.J. McCroskey. Unsteady airfoils. *Annual Review of Fluid Mechanics*, 14, 1982.
- [29] J.G. Leishman. Dynamic stall experiments on the NACA23012 aerofoil. *Experiment in Fluids*, 9:49–58, 1990.
- [30] R.B. Green and R.A.McD. Galbraith. Phenomena observed during aerofoil ramp-down motions from the fully separated state. *Aeronautical Journal*, 98(979):349–356, November 1994.
- [31] R.B. Green. An investigation of dynamic stall through the application of leading edge roughness. *The Aeronautical journal*, 98(971), January 1994.
- [32] R.B. Green, R.A.McD. Galbraith, and A.J. Niven. Measurements of the dynamic stall vortex convection speed. *Aeronautical Journal*, 96:319–327, October 1992.
- [33] R.B. Green and R.A.McD. Galbraith. Dynamic stall vortex convection: thoughts on compressibility. *The Aeronautical journal*, 100(999), November 1996.
- [34] E.J. Jumper, R.L. Dimmick, and A.J.S. Allaire. Effect of pitch location on dynamic stall. *Journal of Fluids Engineering, Transactions of the ASME*, 111(3), September 1989.
- [35] N.D. Ham. Aerodynamic loading on a two-dimensional airfoil during dynamic stall. *AIAA Journal*, 6(10):1927–1934, October 1968.

- [36] D.N. Gorelov. Calculation of pressure distribution near the leading edge of an airfoil using the discrete-vortex method. *Journal of Applied Mechanics and Technical Physics (English translation of PMTF, Zhurnal Prikladnoi Mekhaniki i Tekhnicheskoi Fiziki)*, 37(1), 1996.
- [37] T. Reu and S.X. Ying. Hybrid grid approach to study dynamic stall. *AIAA Journal*, 30(1):2670–2676, 1992.
- [38] A. Allet, S. Halle, and I. Paraschivoiu. Dynamic stall simulation including turbulence modeling. *American Society of Mechanical Engineers, Solar Energy Division (Publication) SED*, 1995.
- [39] S. Aso and M. Hayashi. Dynamic stall calculations by a discrete vortex method. *Pitman research notes in mathematics series or Research notes in mathematics No:317*, 1994.
- [40] S. Aso, A. Sakamoto, and M. Hayashi. Numerical simulations of separated flows around oscillating airfoil for dynamic stall phenomena. *Proceedings - Society of Automotive Engineers*, 1991.
- [41] D.H. Choi and L. Landweber. Inviscid analysis of two-dimensional airfoils in unsteady motion using conformal mapping. *AIAA Journal*, 28(12):2025–2033, December 1990.
- [42] P.G. Choudhuri, D.D. Knight, and M.R. Visbal. Two-dimensional unsteady leading-edge separation on a pitching airfoil. *AIAA Journal*, 32(4):673–681, April 1994.
- [43] R.A. McD. Galbraith and M. Vezza. Methods of predicting dynamic stall. *Proceedings of the BWEA Wind Energy Conference (British Wind Energy Association)*, 1986.

- [44] W. Geissler, J. Kompenhans, M. Raffel, H. Vollmers, and P. Wernert. Numerical and experimental investigations of unsteady flows under deep dynamic stall conditions. *Proceedings of the 20th European Rotorcraft Forum*, pages 22.1–22.19, 1994.
- [45] H. Lin and M. Vezza. Implementation of a vortex method for the prediction of separated incompressible flows. *G.U. AERO report 9425*, 1994.
- [46] H. Lin and M. Vezza. A pure vortex method for simulating unsteady, incompressible, separated flows around static and pitching aerofoils. In *Proceedings of 20th ICAS Congress, Sorrents, Italy*, September 1996.
- [47] H. Lin, M. Vezza, and R.A.McD. Galbraith. Discrete vortex method for simulating unsteady flow around pitching airfoils. *AIAA Journal*, 35(3):494–499, March 1997.
- [48] M. Vezza and R.A.McD. Galbraith. Inviscid model of unsteady aerofoil flow with fixed upper surface separation. *International Journal for Numerical Methods in Fluids*, 5(6), June 1985.
- [49] M.R. Visbal and J.S. Shang. Investigation of the flow structures around a rapidly pitching airfoil. *AIAA Journal*, 27(8):1044–1051, 1989.
- [50] M.R. Visbal. Dynamic stall of a constant-rate pitching airfoil. *Journal of Aircraft*, 27(5):400–407, May 1990.
- [51] I.H. Tuncer, J.C. Wu, and C.W. Wang. Theoretical and numerical studies of oscillating airfoils. *AIAA Journal*, 28(9):1615–1624, September 1990.
- [52] T. Tanahashi, S.I. Amano, and A. Kano. Numerical analysis of dynamic stall around an oscillating airfoil using TVD finite volume method. *Nippon Kikai*

Gakkai Ronbunshu, B Hen/Transactions of the Japan Society of Mechanical Engineers, Part B, 60(574), June 1994.

- [53] P.R. Spalart, A. Leonard, and D. Baganoff. Numerical simulation of separated flows. *NASA TM-84328*, 1983.
- [54] Y. Shida, K. Kuwahara, K. Ono, and H. Takami. Computation of dynamic stall of a NACA-0012 airfoil. *AIAA Journal*, 25(3), March 1987.
- [55] K. Salari, P.J. Roache, and D.C. Wilcox. Numerical simulation of dynamic stall using the two-equation k-omega turbulence model. *American Society of Mechanical Engineers, Fluids Engineering Division (Publication) FED*, 196, 1994.
- [56] G.A. Oswald, K.N. Ghia, and U. Ghia. Simulation of dynamic stall phenomenon using unsteady Navier-Stokes equations. *Computer Physics Communications*, 65:209–218, 1991.
- [57] W.G. Park and L.N. Sankar. Dynamic stall simulation of a NACA 0012 airfoil using the primitive variable formulation. *American Society of Mechanical Engineers, Fluids Engineering Division (Publication) FED*, 196, 1994.
- [58] S.W. Kim, K.B.M.Q. Zaman, and J. Panda. Numerical investigation of unsteady transitional flow over oscillating airfoil. *Journal of Fluids Engineering, Transactions of the ASME*, 117(1):10–16, March 1995.
- [59] D. Favier, A. Agnes, C. Barbi, and C. Maresca. Combined translation/pitch motion: A new airfoil dynamic stall simulation. *Journal of Aircraft*, 25(9), September 1988.
- [60] C.P. Gendrich, M.M. Koochesfahani, and M.R. Visbal. Effects of initial acceleration on the flow field development around rapidly pitching airfoils. *Journal of Fluids Engineering, Transactions of the ASME*, 117(1), March 1995.

- [61] J.D. Anderson, Jr. *Fundamentals of Aerodynamics*. McGraw-Hill, 1984.
- [62] B. Thwaites. *Incompressible Aerodynamics: an account of the theory and observation of the steady flow of incompressible fluid past aerofoils, wings and other bodies*. Oxford University Press, 1960.
- [63] R.I. Lewis. *Vortex element methods for fluid dynamic analysis of engineering systems*. Cambridge University Press, 1991.
- [64] J. Katz and A. Plotkin. *Low-speed aerodynamics : from wing theory to panel methods*. McGraw-Hill, 1991.
- [65] W.J. McCroskey, K.W. McAlister, L.W. Carr, S.L. Pucci, O. Lambert, and R.F. Lt. Indergrand. Dynamic stall on advanced airfoil sections. *Journal of the American Helicopter Society*, 26(3):40–50, July 1981.
- [66] N.D. Ham and M.I. Young. Torsional oscillation of helicopter blades due to stall. *Journal of Aircraft*, 3(3):218–224, May 1966.
- [67] N.D. Ham. Stall flutter of helicopter rotor blades: A special case of the dynamic stall phenomenon. *Journal of the American Helicopter Society*, 12(4):19–21, October 1967.
- [68] F.O. Carta. An analysis of the stall flutter instability of helicopter rotor blades. *Journal of the American Helicopter Society*, 12(4):1–18, October 1967.
- [69] G. Bir, I. Chopra, and K. Nguyen. Development of UMARC (University of Maryland Advanced Rotorcraft Code). *Annual Forum Proceedings - American Helicopter Society*, 1, 1990.
- [70] D. Barwey and G.H. Gaonkar. Dynamic-stall and structural-modeling effects on helicopter blade stability with experimental correlation. *AIAA Journal*, 32(4), April 1994.

- [71] C.J. He and R. DuVal. Unsteady airload model with dynamic stall for rotorcraft simulation. *Annual Forum Proceedings - American Helicopter Society*, 2, 1994.
- [72] K.V. Truong and J.J. Costes. Oscillatory behavior of helicopter rotor airloads in the blade stall regime. *Journal of Aircraft*, 32(5), September 1995.
- [73] Y.H. Yu, S. Lee, K.W. McAlister, C. Tung, and C.M. Wang. Dynamic stall control for advanced rotorcraft application. *AIAA Journal*, 33(2), February 1995.
- [74] N.D. Ham and M.S. Garelick. Dynamic stall considerations in helicopter rotors. *Journal of the American Helicopter Society*, 13(2):49–55, April 1968.
- [75] K.W. McAlister, O. Lambert, and D. Petot. Application of the ONERA model of dynamic stall. *NASA Technical Paper 2399*, November 1984.
- [76] G.J. Hancock and J.S.Y. Lam. On the application of axiomatic aerodynamic modelling to aircraft dynamics: Part 4 - two dimensional dynamic stall. *Aeronautical Journal*, 91(902), February 1987.
- [77] A. Yeznasni, R. Derdelinckx, and C. Hirsch. Influence of dynamic stall in the aerodynamic study of HAWTs. *Journal of Wind Engineering and Industrial Aerodynamics*, 39(1-3), May 1992.
- [78] D.E. Shipley, M.S. Miller, and M.C. Robinson. Dynamic stall occurrence on a horizontal axis wind turbine blade. *American Society of Mechanical Engineers, Solar Energy Division (Publication) SED*, 1995.
- [79] J.W. Oler and M.T. Dobbins. VAWT aerodynamic code development at Texas Tech University. *American Society of Mechanical Engineers, Solar Energy Division (Publication) SED*, 9, 1990.

- [80] S.R. Major and I. Paraschivoiu. Indicial method calculating dynamic stall on a vertical axis wind turbine. *Journal of Propulsion and Power*, 8(4), July 1992.
- [81] A. Laneville and P. Vittecoq. Dynamic stall: The case of the vertical axis wind turbine. *Journal of Solar Energy Engineering, Transactions of the ASME*, 108(2), May 1986.
- [82] R.A.McD. Galbraith, A.J. Niven, and F.N. Coton. Aspects of unsteady aerodynamics in wind turbines. *Wind Engineering*, 14(5), 1990.
- [83] W.Q. Liu, I. Paraschivoiu, and R. Martinuzzi. Calculation of dynamic stall on sandia 34-m VAWT using an indicial model. *Wind Engineering*, 16(6), 1992.
- [84] D.E. Gault. A correlation of low speed airfoil section stalling characteristics with reynolds number and airfoil geometry. *NACA TN-3963*, 1956.
- [85] T.S. Beddoes. A synthesis of unsteady aerodynamic effects including stall hysteresis. *Vertica*, 1(2):113–123, 1976.
- [86] C.T. Tran and D. Petot. A semi-empirical model for the dynamic stall of airfoils in view of the application to the calculation of responses of a helicopter blade in forward flight. *Vertica*, 5(1):35–53, 1981.
- [87] S.T. Gangwani. Synthesized airfoil data method for prediction of dynamic stall and unsteady airloads. *Vertica*, 8(2):93–118, 1984.
- [88] J.G. Leishman and T.S. Beddoes. A semi-empirical model for dynamic stall. *Journal of the American Helicopter Society*, 34(3), July 1989.
- [89] T.S.R. Reddy and K.R.V. Kaza. Comparative study of some dynamic stall models. *NASA Technical Memorandum*, March 1987.
- [90] T.S. Beddoes. Representation of airfoil behaviour. *Vertica*, 7(2), 1983.

- [91] K. Pierce and A.C. Hansen. Prediction of wind turbine rotor loads using the Beddoes-Leishman model for dynamic stall. *Journal of Solar Energy Engineering*, 117(3), 1995.
- [92] R.A.McD. Galbraith, F.N. Coton, and D.J. Robison. Prescribed wake methodologies for wind turbine design codes. *Proceedings of the 30th Intersociety Energy Conversion Engineering Conference*, 1, 1995.
- [93] S.T. Gangwani. Prediction of dynamic stall and unsteady airloads for rotorblades. *Journal of the American Helicopter Society*, 27(4), October 1982.
- [94] M. Raffel, J. Kompenhans, and P. Wernert. Investigation of the unsteady flow velocity field above an airfoil pitching under deep dynamic stall conditions. *Experiments in Fluids*, 19:103–111, 1995.
- [95] R.B. Green and R.A.McD. Galbraith. Dynamic recovery to fully attached aerofoil flow from deep stall. *AIAA Journal*, 33(8):1433, 1995.
- [96] D.M. Tang and E.H. Dowell. Experimental investigation of three-dimensional dynamic stall model oscillating in pitch. *Journal of Aircraft*, 32(5), 1995.
- [97] R.A.McD. Galbraith, F.N. Coton, D. Jiang, and R. Gilmour. The comparison between the dynamic stall of a finite wing with straight and swept tips. In *Proceedings of 20th ICAS Congress, Sorrento, Italy*, September 1996.
- [98] M.T. Patterson and P.F. Lorber. Computational and experimental studies of compressible dynamic stall. *Journal of Fluids and Structures*, 4(3), May 1990.
- [99] C.A.J. Fletcher. *Computational Techniques for Fluid Dynamics Volume 1*. Springer-Verlag, 1988.

- [100] C.A.J. Fletcher. *Computational Techniques for Fluid Dynamics Volume 2*. Springer-Verlag, 1988.
- [101] D.A. Anderson, J.C. Tannehill, and R.H. Fletcher. *Computational Fluid Mechanics and Heat Transfer*. Hemisphere Publishing Corporation, 1984.
- [102] K.A. Hoffmann and S.T. Chiang. *Computational Fluid Dynamics for Engineers*. Wichita, Kan. : Engineering Education System, 1993.
- [103] J.P. Boris. New directions in computational fluid dynamics. *Annual Review of Fluid Mechanics*, 21:345–385, 1989.
- [104] R. Glowinski and O. Pironneau. Finite element methods for Navier-Stokes equations. *Annual Review of Fluid Mechanics*, 24:167–204, 1992.
- [105] M.O. Bristeau, C. Bernardi, O. Pironneau, and M.G. Vallet. Numerical analysis for compressible isothermal flows. In *Proceedings of Symp. on Applied Mathematics*, 1990.
- [106] M.O. Bristeau, R. Glowinski, and J. Periaux. Numerical methods for the Navier-Stokes equations - applications to the simulation of compressible and incompressible viscous flows. *Computer Physics Reports*, 6:73–187, 1987.
- [107] K.N. Ghia, Y. Yang, G.A. Osswald, and U. Ghia. Study of the role of unsteady separation in the formation of dynamic stall vortex. *AIAA-92-0196*, January 1992.
- [108] K.N. Ghia, Y. Yang, G.A. Osswald, and U. Ghia. Physics of forced unsteady flow for a NACA 0015 airfoil undergoing constant-rate pitch-up motion. *Fluid Dynamics Research*, 10, 1992.

- [109] R.H. Landon. NACA0012 oscillatory and transient pitching. *Compendium of Unsteady Aerodynamic Measurements AGARD Rept 702*, August 1992.
- [110] B.S. Baldwin and H. Lomax. Thin layer approximation and algebraic model for separated flows. *AIAA Paper 78-0257*, January 1978.
- [111] R. Beam and R.F. Warming. An implicit finite difference algorithm for hyperbolic systems in conservative law form. *Journal of Computational Physics*, 22(1):87–110, September 1976.
- [112] I.H. Tuncer, J.A. Ekaterinaris, and M.F. Plutzer. Viscous-inviscid interaction method for unsteady low-speed airfoil flows. *AIAA Journal*, 33(1):151–154, January 1995.
- [113] D. Knight and P.G. Choudhuri. 2-D unsteady leading edge separation on a pitching airfoil. *AIAA 93-2977*, July 1993.
- [114] T. Sarpkaya. Computational methods with vortices – the 1988 freeman scholar lecture. *Journal of Fluids Engineering*, 111(1):5–52, 1989.
- [115] R.R. Clements and D.J. Maull. The representation of sheets of vorticity by discrete vortices. *Progress in Aerospace Sciences*, 16(2):129–146, 1975.
- [116] P.G. Saffman. Dynamics of vorticity. *Journal of Fluid Mechanics*, 106:49–58, 1981.
- [117] P.G. Saffman and G.R. Baker. Vortex interactions. *Annual Review of Fluid Mechanics*, 11:95–122, 1979.
- [118] A. Leonard. Vortex methods for flow simulation. *Journal of Computational Physics*, 37(3):289–335, October 1980.

- [119] A. Leonard. Computing three-dimensional incompressible flows with vortex elements. *Annual Review of Fluid Mechanics*, 17:523–559, 1985.
- [120] H. Aref. Integrable, chaotic and turbulent vortex motion in two dimensional flows. *Annual Review of Fluid Mechanics*, 15:345–389, 1983.
- [121] T. Sarpkaya. Brief reviews of some time-dependent flows. *Journal of Fluids Engineering, Transactions of the ASME*, 114(3):283–298, 1992.
- [122] T.L. Doligalski, C.R. Smith, and J.D.A. Walker. Vortex interactions with walls. *Annual Review of Fluid Mechanics*, 26:573–616, 1994.
- [123] B.R. Morton. The generation and decay of vorticity. *Geophysical and Astrophysical Fluid Dynamics*, 28:277–308, 1984.
- [124] C.C. Chang. Random vortex methods for the Navier-Stokes equations. *Journal of Computational Physics*, 76(2):281–300, June 1988.
- [125] C. Greengard. The core spreading vortex method approximates the wrong equation. *Journal of Computational Physics*, 61(2):345–348, November 1985.
- [126] R. Krasny. Computation of vortex sheet roll-up in the trefftz plane. *Journal of Fluid Mechanics*, 184:123–155, 1987.
- [127] J.C.S. Meng. The physics of vortex-ring evolution in a stratified and shearing environment. *Journal of Fluid Mechanics*, 84:455–469, 1978.
- [128] O. Inoue. Vortex simulation of a turbulent mixing layer. *AIAA Journal*, 23(3):367–372, March 1985.
- [129] P.R. Spalart. Vortex methods for separated flows. *NASA TM-100068*, June 1988.

- [130] E.C. Tiemroth. *The Simulation of the Viscous Flow Around a Cylinder by the Random Vortex Method*. PhD thesis, University of California, Berkeley, 1986.
- [131] A.F. Ghoniem, D.Y. Chen, and A.K. Oppenheim. Formation and inflammation of a turbulent jet. *AIAA Journal*, 24(2):224–229, February 1986.
- [132] C.R. Anderson. A method of local corrections for computing the velocity field due to a distribution of vortex blobs. *Journal of Computational Physics*, 62:111–123, 1986.
- [133] S.B. Baden and E.G. Puckett. A fast vortex method for computing 2D viscous flow. *Journal of Computational Physics*, 91(2):278–297, December 1990.
- [134] L. Greengard and V. Rokhlin. A fast algorithm for particle simulations. *Journal of Computational Physics*, 73(2):325–348, December 1987.
- [135] J. Carrier, L. Greengard, and V. Rokhlin. A fast adaptive multipole algorithm for particle simulations. *SIAM Journal on Scientific and Statistical Computing*, 9(4):669–686, July 1988.
- [136] M.L. van Dommelen and E.A. Rundensteiner. Fast, adaptive summation of point forces in the two-dimensional Poisson equation. *Journal of Computational Physics*, 83(1):126–147, July 1989.
- [137] J.P. Christiansen. Numerical simulation of hydromechanics by the method of point vortices. *Journal of Computational Physics*, 13(2):363–379, October 1973.
- [138] G.R. Baker. The ‘cloud in cell’ technique applied to the roll-up of vortex sheets. *Journal of Computational Physics*, 31(1):76–95, April 1979.
- [139] M.J. Downie and P. Bettess. Discrete vortex method and parallel processing using transputers. *Engineering Computations (Swansea, Wales)*, 6(2), June 1989.

- [140] J.A. Sethian, J.P. Brunet, A. Greenberg, and J.P. Mesirov. A parallel implementation of the random vortex method. *Computer Physics Communications*, 65:231–237, April 1991.
- [141] J.A. Sethian, J.P. Brunet, A. Greenberg, and J.P. Mesirov. Two-dimensional, viscous, incompressible flow in complex geometries on a massively parallel processor. *Journal of Computational Physics*, 101(1):185–206, July 1992.
- [142] A.J. Chorin. Numerical study of slightly viscous flow. *Journal of Fluid Mechanics*, 57(4):785–796, 1973.
- [143] K. Kuwahara and H. Takami. Numerical studies of two dimensional vortex motion by a system of point vortices. *Journal of Physical Society of Japan*, 34:247–253, 1973.
- [144] P. Degond and S. Mas-Gallic. The weighted particle method for convection-diffusion equations part 1 the case of an isotropic viscosity. *Mathematics of Computation*, 53(188):485–507, October 1989.
- [145] G.S. Winckelmans and A. Leonard. Contribution to vortex particle methods for the computation of three-dimensional incompressible unsteady flows. *Journal of Computational Physics*, 109(2):247–273, December 1993.
- [146] P. Koumoutsakos, A. Leonard, and F. Pepin. Boundary conditions for viscous vortex methods. *Journal of Computational Physics*, 113(1):52–61, July 1994.
- [147] P. Koumoutsakos and A. Leonard. High-resolution simulations of the flow around an impulsively started cylinder using vortex methods. *Journal of Fluid Mechanics*, 296, August 1995.
- [148] O.H. Hald. Convergence of a random method with creation of vorticity. *SIAM Journal on Scientific and Statistical Computing*, 7:1373, 1986.

- [149] J.T. Beale and A. Majda. Vortex methods I: Convergence in three dimensions. *Mathematics of Computation*, 39(159):1–27, 1982.
- [150] J.T. Beale and A. Majda. Vortex methods II: Higher order accuracy in two and three dimensions. *Mathematics of Computation*, 39(159):29–52, 1982.
- [151] C. Greengard. Convergence of the vortex filament method. *Mathematics of Computation*, 47(176):387–398, 1986.
- [152] S. Roberts. Accuracy of the random vortex method for a problem with non-smooth initial conditions. *Journal of Computational Physics*, 58(1):29–43, March 1985.
- [153] T. Sarpkaya. An inviscid model of two-dimensional vortex shedding for transient and asymptotically steady separated flow over an inclined flat plate. *Journal of Fluid Mechanics*, 68:109–128, 1975.
- [154] W.R. Sears. Unsteady motion of airfoils with boundary-layer separation. *AIAA Journal*, 14:216–220, 1976.
- [155] A.J. Chorin. Vortex sheet approximation of boundary layers. *Journal of Computational Physics*, 27(3):428–442, June 1978.
- [156] P.A. Smith. *Computation of Viscous Flows by the Vortex Method*. PhD thesis, University of Manchester, 1984.
- [157] L.L. van Dommelen. Unsteady separation from a Lagrangian point of view. *Proceeding of Forum on Unsteady Flow Separation ASME FED*, 52:81–84, 1987.
- [158] M.J. Kim and D.T. Mook. Application of continuous vorticity panels to general unsteady incompressible two-dimensional lifting flows. *Journal of Aircraft*, 23(6):464–471, June 1986.

- [159] S.A. Huyer and J.R. Grant. Computation of unsteady separated flow fields using anisotropic vorticity elements. *Journal of Fluids Engineering - Transactions of the ASME*, 118(4), 1996.
- [160] M. Vezza. A new vortex method for modelling two dimensional unsteady incompressible viscous flows. *G.U. AERO report 9245*, 1992.
- [161] M.D. Greenberg. *Applications of Green's Functions in Science and Engineering*. Prentice-Hall, 1971.
- [162] J.D. Batchelor, Jr. *An Introduction to Fluid Dynamics*. Cambridge University Press, 1967.
- [163] J.C. Wu, D.L. Huff, and L.N. Sankar. Evaluation of three turbulence models in static air loads and dynamic stall predictions. *Journal of Aircraft*, 27(4), April 1990.
- [164] D.P. Rizzetta and M.H. Visbal. Comparative numerical study of two turbulence models for airfoil static and dynamic stall. *AIAA Journal*, 31(4), April 1993.
- [165] J.A. Ekaterinaris, G.R. Srinivasan, and W.J. McCroskey. Present capabilities of predicting two-dimensional dynamic stall. *Aerodynamics and Aeroacoustics of Rotorcraft, Berlin, Germany, AGARD CP-552*, October 1994.

Appendix A

The velocity of point \mathbf{r}_p induced by vortex with circulation $d\Gamma$ at \mathbf{r} is

$$d\mathbf{u}_p = \vec{\mathbf{k}} \times \frac{(d\Gamma)(\vec{\mathbf{r}}_p - \vec{\mathbf{r}})}{2\pi \|\vec{\mathbf{r}}_p - \vec{\mathbf{r}}\|^2} = -\vec{\mathbf{k}} \times \frac{(d\Gamma)(\vec{\mathbf{r}} - \vec{\mathbf{r}}_p)}{2\pi \|\vec{\mathbf{r}} - \vec{\mathbf{r}}_p\|^2} \quad (\text{A.1})$$

where

$$d\Gamma = 2\Omega_B dA$$

By integrating over the body area, the induced velocity becomes

$$\begin{aligned} \vec{\mathbf{u}}_p &= \int_{A_B} d\mathbf{u}_p \\ &= -\frac{\Omega_B}{2\pi} \sum_m \vec{\mathbf{s}}_m \int_0^{\ell_m} \ln \|\vec{\mathbf{r}} - \vec{\mathbf{r}}_p\|^2 ds = -\frac{\Omega_B}{2\pi} \sum_m \vec{\mathbf{s}}_m \mathbf{I}_1 \end{aligned} \quad (\text{A.2})$$

where

$$\begin{aligned} \mathbf{I}_1 &= \int_0^{\ell_m} \ln \|\vec{\mathbf{r}} - \vec{\mathbf{r}}_p\|^2 ds_m \\ &= \ell_m \ln c_1 + \frac{b_0}{\ell_m} \ln \left(\frac{c_1}{a_0} \right) + \frac{2c_0}{\ell_m} \left[\tan^{-1} \left(\frac{c_2}{c_0} \right) - \tan^{-1} \left(\frac{b_0}{c_0} \right) \right] - 2\ell_m \end{aligned}$$

and

$$\begin{aligned} b_0 &= \Delta x_{mp} \Delta x_m + \Delta y_{mp} \Delta y_m \\ c_0 &= \Delta x_{mp} \Delta y_m - \Delta y_{mp} \Delta x_m \\ c_1 &= \Delta x_{m+1p}^2 + \Delta y_{m+1p}^2 \\ c_2 &= \Delta x_{m+1p} \Delta x_m + \Delta y_{m+1p} \Delta y_m \end{aligned}$$

$$\begin{aligned} F_{ji} &= \int_0^{\ell_j} \vec{\mathbf{u}}_p \cdot \vec{\mathbf{n}} ds_j \\ &= -\frac{\Omega_B}{2\pi} \int_0^{\ell_j} \left(\int_{S_B} \vec{\mathbf{s}} \ln \|\vec{\mathbf{r}} - \vec{\mathbf{r}}_p\|^2 ds \right) \cdot \vec{\mathbf{n}} ds_j \\ &= -\frac{\Omega_B}{2\pi} \sum_m (\vec{\mathbf{s}}_m \cdot \vec{\mathbf{n}}_j) \mathbf{I}_2 \end{aligned} \quad (\text{A.3})$$

$$\mathbf{I}_2 = \int_0^{\ell_j} \int_0^{\ell_m} \ln \|\bar{\mathbf{r}} - \bar{\mathbf{r}}_p\|^2 ds_m ds_j$$

$$\begin{aligned} \mathbf{I}_2 &= \ell_m \ell_j \ln c_3 - 3\ell_m \ell_j + \frac{(b_3 a_1 - 2a_5 b_1)}{2\ell_j \ell_m} \ln \left(\frac{c_3}{a_1} \right) \\ &+ \frac{(2a_4 b_1 - b_4 a_1)}{\ell_j \ell_m} \left[\tan^{-1} \left(\frac{-b_1 + \ell_j^2}{c_4} \right) - \tan^{-1} \left(\frac{b_1}{c_4} \right) \right] \\ &+ \frac{(2a_3 - b_3) \ell_j}{2\ell_m} \ln \left(\frac{c_3}{c_6} \right) + \frac{(2a_4 - b_4) \ell_j}{\ell_m} \left[\tan^{-1} \left(\frac{c_9}{c_{11}} \right) - \tan^{-1} \left(\frac{c_{10}}{c_{11}} \right) \right] \\ &+ \frac{(-b_3 a_2 + 2a_3 b_2)}{2\ell_j \ell_m} \ln \left(\frac{c_6}{a_2} \right) + \frac{(-2a_4 b_2 + b_4 a_2)}{\ell_j \ell_m} \left[\tan^{-1} \left(\frac{-b_2 + \ell_j^2}{c_7} \right) - \tan^{-1} \left(\frac{b_2}{c_7} \right) \right] \end{aligned}$$

for $|m - j| > 1$,

$$\mathbf{I}_2 = \ell_j^2 (2 \ln \ell_j - 3)$$

for $m = j$,

$$\begin{aligned} \mathbf{I}_2 &= -3\ell_{j+1} \ell_j + \frac{a_6 \ell_j}{\ell_{j+1}} \left[\tan^{-1} \left(\frac{a_3 + \ell_{j+1}^2}{a_6} \right) - \tan^{-1} \left(\frac{a_3}{a_6} \right) \right] \\ &+ \frac{2a_6^3}{\ell_j^3 \ell_{j+1}} \left[\tan^{-1} \left(\frac{a_3 + \ell_j^2}{a_6} \right) - \tan^{-1} \left(\frac{a_3}{a_6} \right) \right] \\ &+ \frac{a_6 (a_6^2 - a_3^2)}{\ell_j^3 \ell_{j+1}} \left[\tan^{-1} \left(\frac{a_6}{a_3 + \ell_j^2} \right) - \tan^{-1} \left(\frac{a_6}{a_3} \right) \right] \\ &+ \frac{a_3 \ell_{j+1}}{2\ell_j} \ln \left[\frac{\ell_{j+1}^2 + 2a_3 + \ell_j^2}{\ell_{j+1}^2} \right] + \frac{a_3 \ell_j}{2\ell_{j+1}} \ln \left[\frac{\ell_{j+1}^2 + 2a_3 + \ell_j^2}{\ell_j^2} \right] \\ &+ \ell_j \ell_{j+1} \ln (\ell_{j+1}^2 + 2a_3 + \ell_j^2) \end{aligned}$$

for $m = j + 1$, and

$$\begin{aligned} \mathbf{I}_2 &= -3\ell_{j-1} \ell_j + \frac{b_6 \ell_j}{\ell_{j-1}} \left[\tan^{-1} \left(\frac{b_3 + \ell_{j-1}^2}{b_6} \right) - \tan^{-1} \left(\frac{b_3}{b_6} \right) \right] \\ &+ \frac{2b_6^3}{\ell_j^3 \ell_{j-1}} \left[\tan^{-1} \left(\frac{b_3 + \ell_j^2}{b_6} \right) - \tan^{-1} \left(\frac{b_3}{b_6} \right) \right] \\ &+ \frac{b_6 (b_6^2 - b_3^2)}{\ell_j^3 \ell_{j-1}} \left[\tan^{-1} \left(\frac{b_6}{b_3 + \ell_j^2} \right) - \tan^{-1} \left(\frac{b_6}{b_3} \right) \right] \\ &+ \frac{b_3 \ell_{j-1}}{2\ell_j} \ln \left[\frac{\ell_{j-1}^2 + 2b_3 + \ell_j^2}{\ell_{j-1}^2} \right] + \frac{b_3 \ell_j}{2\ell_{j-1}} \ln \left[\frac{\ell_{j-1}^2 + 2b_3 + \ell_j^2}{\ell_j^2} \right] \\ &+ \ell_j \ell_{j-1} \ln (\ell_{j-1}^2 + 2b_3 + \ell_j^2) \end{aligned}$$

for $m = j - 1$.

Some variables are expressed as

$$\begin{aligned}
 a_1 &= \Delta x_{m+1j}^2 + \Delta y_{m+1j}^2 \\
 a_2 &= \Delta x_{mj}^2 + \Delta y_{mj}^2 \\
 a_3 &= \Delta x_{mj} \Delta x_m + \Delta y_{mj} \Delta y_m \\
 a_4 &= \Delta x_{mj} \Delta y_m - \Delta y_{mj} \Delta x_m \\
 a_5 &= \Delta x_{m+1j} \Delta x_m + \Delta y_{m+1j} \Delta y_m \\
 a_6 &= \sqrt{\ell_j^2 \ell_{j+1}^2 - a_3^2} \\
 b_1 &= \Delta x_{m+1j} \Delta x_j + \Delta y_{m+1j} \Delta y_j \\
 b_2 &= \Delta x_{mj} \Delta x_j + \Delta y_{mj} \Delta y_j \\
 b_3 &= \Delta x_m \Delta x_j + \Delta y_m \Delta y_j \\
 b_4 &= \Delta x_j \Delta y_m - \Delta y_j \Delta x_m \\
 b_6 &= \sqrt{\ell_j^2 \ell_{j-1}^2 - b_3^2} \\
 c_3 &= \Delta x_{m+1j+1}^2 + \Delta y_{m+1j+1}^2 \\
 c_4 &= \Delta x_{m+1j} \Delta y_j - \Delta y_{m+1j} \Delta x_j \\
 c_6 &= \Delta x_{mj+1}^2 + \Delta y_{mj+1}^2 \\
 c_7 &= \Delta x_{mj} \Delta y_j - \Delta y_{mj} \Delta x_j \\
 c_9 &= \Delta x_{m+1j+1} \Delta x_m + \Delta y_{m+1j+1} \Delta y_m \\
 c_{10} &= \Delta x_{mj+1} \Delta x_m + \Delta y_{mj+1} \Delta y_m \\
 c_{11} &= \Delta x_{mj+1} \Delta y_m - \Delta y_{mj+1} \Delta x_m
 \end{aligned}$$